MORPHED POTENTIAL ENERGY SURFACES FROM THE SPECTROSCOPY OF WEAKLY BOUND COMPLEXES

A Dissertation

by

LUIS A. RIVERA-RIVERA

Submitted to the Office of Graduate Studies of
Texas A&M University
in partial fulfillment of the requirements for the degree of

DOCTOR OF PHILOSOPHY

May 2011

Major Subject: Chemistry

Morphed Potential Energy Surfaces from the

Spectroscopy of Weakly Bound Complexes

MORPHED POTENTIAL ENERGY SURFACES FROM THE SPECTROSCOPY OF WEAKLY BOUND COMPLEXES

A Dissertation

by

LUIS A. RIVERA-RIVERA

Submitted to the Office of Graduate Studies of
Texas A&M University
in partial fulfillment of the requirements for the degree of

DOCTOR OF PHILOSOPHY

Approved by:

Chair of Committee,	Robert R. Lucchese
Committee Members,	John W. Bevan
	Steven E. Wheeler
	Jay R. Walton
Head of Department,	David H. Russell

May 2011

Major Subject: Chemistry

ABSTRACT

Morphed Potential Energy Surfaces from the Spectroscopy of Weakly Bound Complexes. (May 2011)

Luis A. Rivera-Rivera, B.S., University of Puerto Rico at Mayagüez;

M.S., University of Puerto Rico at Mayagüez

Chair of Advisory Committee: Dr. Robert R. Lucchese

In this research the so-called potential morphing method was used to generate reliable interaction potential energy surfaces for weakly bound complexes. The potential morphing method is based on the optimization of modified computed *ab initio* potential energy surfaces to give predicted spectroscopic data, in agreement with the experimental values. In the standard potential morphing procedure the computed *ab initio* potential is adjusted by scaling, shifting, and dilating transformations to reproduce the experimental data.

In this research, selected systems have been chosen to be studied based on the availability of varied and accurate sets of experimental data. In the present work, accurate interaction potential energy surfaces are obtained for the weakly bound complexes: Ne:HCl, OC:HX (X = F, Cl, Br, I) and HI:CO_2. A comprehensive study on the interaction potential of these systems provides fundamental perspectives on the influence of different intermolecular forces. In addition the ground state isotopic

isomerization observed in the OC:HI system may suggest a possible structural change of proteins, and other biological macromolecules, in deuterated solvents.

In this dissertation, an alternative approach to morphing the potential energy surfaces of non-covalent interactions is also presented. In this approach the morphed potential is generated as a linear combination of *ab initio* potentials, that are computed at different levels of theory. This new morphing approach is applied to OC:HCl and is found to be of similar accuracy to that of the previous morphing method. In addition, this new method is also extended from four-dimensions to six-dimensions and is applied to the OC:HF system to obtain a vibrationally-complete six-dimensional morphed potential.

DEDICATION

This dissertation is dedicated to very special people that have always encouraged me to complete my work.

To:

my wife Teresa and our baby,

my parents, Maria & Gerardo,

my family,

the Carrasco family,

my teachers,

and

my friends

ACKNOWLEDGEMENTS

I would like to thank my committee chair, Dr. R. R. Lucchese, my committee members (Dr. J. W. Bevan, Dr. S. E. Wheeler, and Dr. J. R. Walton), Dr. Y.-Q. Gao, Dr. G. Kanschat, and Dr. L. M. Pérez for their guidance and support throughout the course of this research. Also, I would like to thank the members of Dr. Lucchese's, Dr. Bevan's, and Dr. Yeager's research groups, for their help and friendship. The Laboratory for Molecular Simulation, the Supercomputing Facility, and the Brazos HPC cluster at Texas A&M University are thanked, as well, for providing support and computer time. Lastly, I would like to thank the National Science Foundation, the Robert A. Welch Foundation, and the Department of Chemistry at Texas A&M University for financial support.

NOMENCLATURE

ACCD	Approximate double substitution coupled cluster
aug-cc-pVQZ	Augmented correlation consistent polarized valence quadruple zeta basis set
aug-cc-pVQZ-DK	Augmented correlation consistent polarized valence quadruple zeta Douglas-Kroll basis set
aug-cc-pVTZ	Augmented correlation consistent polarized valence triple zeta basis set
aug-cc-pVTZ-pp	Augmented correlation consistent polarized valence triple zeta pseudopotential basis set
aug-cc-pV5Z	Augmented correlation consistent polarized valence quintuple zeta basis set
BSSE	Basis set superposition error
CCSD(T)	Coupled cluster singles and doubles with perturbative triples
CM	Compound model
CMM	Compound model morphing
CP	Counterpoise
DFT	Density functional theory
DKH2	Douglas-Kroll-Hess second order
DNA	Deoxyribonucleic acid
Exp	Experimental
HF	Hartree-Fock
HSRK	Hilbert space reproducing kernel
IR	Infrared

NOMENCLATURE (CONTINUED)

MMC	Molecular mechanics for clusters
MP2	Moller-Plesset second order
MP4	Moller-Plesset fourth order
NBF	Number of basis functions
NBO	Natural bond orbital
PCM	Potential coordinate morphing
PES	Potential energy surface
RKR	Rydberg-Klein-Rees
RMS	Root mean square
RNA	Ribonucleic acid
VCI	Vibrational configuration interaction
VSCF	Vibrational self-consistent field

TABLE OF CONTENTS

Page

ABSTRACT iii

DEDICATION v

ACKNOWLEDGEMENTS vi

NOMENCLATURE vii

TABLE OF CONTENTS ix

LIST OF FIGURES xi

LIST OF TABLES xiii

1. INTRODUCTION 1

    1.1 Aims 4

2. PREVIOUS WORK ON POTENTIAL MORPHING METHODOLOGY 6

3. THEORETICAL METHODOLOGIES 10

    3.1 *Ab initio* calculations of the interaction potentials 10
    3.2 Fitting of the *ab initio* potentials 12
    3.3 Calculation of rovibrational energy levels 17
    3.4 Calculation of the spectroscopic constants 26
    3.5 Compound model morphing method 27

4. APPLICATIONS 31

    4.1 Ne:HCl 32
    4.2 OC:HCl 45
    4.3 OC:HBr 57
    4.4 OC:HI 64
    4.5 HI:CO_2 75
    4.6 OC:HF 84

5. CONCLUSIONS 101

TABLE OF CONTENTS (CONTINUED)

Page

REFERENCES 105

VITA 119

LIST OF FIGURES

		Page
Figure 1	The Jacobi coordinates for different weakly bound systems.....	11
Figure 2	$G(\gamma)$ vs. γ curve for the CMM method	29
Figure 3	Morphed interaction potential of Ne:HCl	38
Figure 4	Adiabatic potential surfaces for the ^{20}Ne:H^{35}Cl isotopomer.....	39
Figure 5	Ground state probability densities for the ^{20}Ne-H^{35}Cl isotopomer.....	42
Figure 6	Two-dimensional slices of the interaction potential of ^{16}O^{12}C:H^{35}Cl generated using the CMM method.....	52
Figure 7	The corresponding estimated errors on the ^{16}O^{12}C:H^{35}Cl CMM potential, relative to the potential at infinite separation	53
Figure 8	Differences between interaction potentials of ^{16}O^{12}C:H^{35}Cl generated by the PCM and CMM methods.....	54
Figure 9	Two-dimensional slices of the $V_{\mathrm{CMM}}^{(3)}$ interaction potential of ^{16}O^{12}C:H^{79}Br	61
Figure 10	The corresponding estimated errors on the ^{16}O^{12}C:H^{79}Br CMM potential, relative to the potential at infinite separation	62
Figure 11	Morphed potential of ^{16}O^{12}C:HI at R = 4.18 Å	69
Figure 12	Morphed potential of ^{16}O^{12}C:HI at R = 4.90 Å	70
Figure 13	Ground state probability densities for ^{16}O^{12}C-HI and ^{16}O^{12}C-IH	71
Figure 14	Ground state probability densities for ^{16}O^{12}C-ID and ^{16}O^{12}C-DI	72
Figure 15	Morphed interaction potential of HI:^{12}C^{16}O$_2$	79

LIST OF FIGURES (CONTINUED)

		Page
Figure 16	Corresponding statistical uncertainties for the morphed potential of HI:$^{12}C^{16}O_2$	80
Figure 17	Energy level diagram for OC-DF	93
Figure 18	Two-dimensional slices of the adiabatic $V^{(0,0)}$ interaction morphed potential (relativistic $V^{(4)}_{CMM}$), of $^{16}O^{12}C$:HF	97
Figure 19	The corresponding estimated errors on the $^{16}O^{12}C$:HF morphed potential, relative to the potential at infinite separation	98

LIST OF TABLES

		Page
Table 1	Experimental data of Ne:HCl used in the fits and fitted values, and the uncertainties used	36
Table 2	Optimized morphing parameters $C_{\alpha,i,j}$ and their corresponding uncertainties for Ne:HCl	37
Table 3	Correlation matrix of the morphing parameters ($C_{\alpha,i,j}$) for Ne:HCl	37
Table 4	Features of various Ne:HCl potentials	40
Table 5	Predicted spectroscopic constants from the morphed potential for Ne-HCl	43
Table 6	Experimental data of OC:HCl used in the fits and fitted values, and their uncertainties	49
Table 7	Optimized values for the morphing parameters of OC:HCl	50
Table 8	Features of morphed potentials of OC:HCl	55
Table 9	Comparison of predicted vibrational frequencies and D_0 energy of $^{16}O^{12}C$-$H^{35}Cl$	55
Table 10	Comparison of previous potentials of OC:HCl	55
Table 11	Experimental data of OC:HBr used in the fits and fitted values, and their uncertainties	60
Table 12	Optimized values for the morphing parameters of OC:HBr	60
Table 13	Predictions of ν_3 and ν_4^1 frequencies, for $^{16}O^{12}C$-$H^{79}Br$, using the $V_{\mathrm{CMM}}^{(3)}$ potential	60
Table 14	Experimental data of OC:HI used in the fits and fitted values, and their uncertainties	67

LIST OF TABLES (CONTINUED)

		Page
Table 15	Optimized values for the morphing parameters of OC:HI	68
Table 16	Features of OC:HI potentials	68
Table 17	D_0 value for $^{16}O^{12}C$:HI and $^{16}O^{12}C$:DI isomers predicted from the morphed potential	68
Table 18	Experimental data of HI:CO_2 used in the fits and fitted values, and their uncertainties	78
Table 19	Optimized values for the parameters of the morphing functions of HI:CO_2	78
Table 20	Experimental data of OC:HF used in the fits and fitted values, and their uncertainties	89
Table 21	Optimized values for the morphing parameters of OC:HF	90
Table 22	Relativistic effects in the computed observables of OC:HF	91
Table 23	Morphing parameters of the relativistic and non-relativistic potentials	92
Table 24	Accuracy of the relativistic $V_{\mathrm{CMM}}^{(4)}$ potential of OC:HF	92
Table 25	Comparison of previous potentials of OC:HF	99
Table 26	Predictions of ν_3 and ν_4^1 frequencies of $^{16}O^{12}C$-HF, using the relativistic $V_{\mathrm{CMM}}^{(4)}$ potential	99

1. INTRODUCTION

Intermolecular interactions such as the van der Waals interaction [1] and the hydrogen bond [2] are ubiquitous throughout nature. These interactions underlie the physical, chemical, and biological properties of many condensed phase molecular systems. For example, the properties of bulk materials and the dynamics of gas-phase molecular collisions are determined by such non-covalent interactions [3,4]. In addition, the stability and structure of biological macromolecules like proteins, ribonucleic acid (RNA), and deoxyribonucleic acid (DNA) are principally due to hydrogen bond interactions [2,5-7].

The concept of intermolecular interactions is closely related to that of the potential energy surface (PES). In the Born-Oppenheimer approximation [8] for the separation of electronic and nuclear motion, the PES is the potential energy that determines the motions of the nuclei. Consequently, the PES is a mathematical function of all coordinates that describes the relative orientation of all atoms in the molecule. For weakly bound molecules the intermolecular PES is determined by the nature of the intermolecular forces, acting between the interacting molecules [9]. Weakly bound molecules have the characteristics of small dissociation energies and large interatomic distances relative to covalent molecules. In addition, weakly bound complexes are bound not by normal chemical bonds, but by physical interactions, such as multipolar electrostatic, dispersion and induction forces, and the hydrogen bond interaction [10].

This dissertation follows the style of Chemical Physics Letters.

Potential energy surfaces increase in complexity as the number of atoms in the molecules increase. In this simple case, the potential energy curve for diatomic molecules depends only on one coordinate, the interatomic separation. For a triatomic molecule the PES is a function of three coordinates, while for a four-atom molecule it is six. In general for an n-atom molecule the PES is a function of $3n$-6 coordinates [9]. A multidimensional surface can have multiple local minima, but only one global minimum that represents the most stable position of atoms in the molecule. In contrast, the local minima represent a metastable position of the atoms. Several equivalent global minima can be possible only if they are related to each other by symmetry. Each minimum in the PES has an associated zero-point energy. If the energy barrier between different minima is not too high and the molecule has enough energy, then it can move from one energy minimum to another by going over the top of the energy barrier. However, if the energy of the molecule is not enough to overcome the energy barrier, it can tunnel from one energy minimum to another [11].

A potential energy surface for weakly bound complexes can be determined by [12-15]: (i) performing *ab initio* calculations; (ii) performing inversions of the experimental data such as spectroscopy, molecular-beam scattering, or reaction kinetics; or (iii) fitting parameters to the experimental data. The accuracy of *ab initio* calculations, in which the Schrödinger equation is solved within the Born-Oppenheimer approximation, is limited by the available computer capabilities [8]. High accuracy *ab initio* potential energy surfaces are still limited to systems with small numbers of electrons. In addition, *ab initio* potential energy surfaces often do not possess the

accuracy to account for high quality spectroscopic and scattering data [12]. On the other hand, the inversion method consists in obtaining the PES by considering the experimental observables as functionals of the potential [12]. However, in the parameter fitting method the experimental data is fitted to a constrained form of the potential with a finite number of parameters [13]. Nevertheless, using experimental data to extract the PES is limited by the quality and availability of experimental data. The experimental data is usually incomplete and can be affected by systematic errors, which can make the inversion process unstable and undetermined [12]. Contrary to the aforementioned, *ab initio* calculations unambiguously give one, and only one, PES that is unique to each molecular system [12].

A useful method to generate more reliable PES for weakly bound complexes is the so-called potential morphing method [16,17]. The potential morphing method is based on the optimization of computed *ab initio* potential energy surfaces to give predicted spectroscopic data, in agreement with the experimental value [16,17]. Several studies [18-32] have been concerned with the development of potential morphing methodology and applications to systems of higher vibrational dimensionality. The methodology also permits the quantitative evaluation of uncertainties associated with the generated PES and predicted properties. A number of elements are necessary to generate a reliable morphed PES [16,33]: (i) a reliable initial *ab initio* PES; (ii) accurate and varied sets of spectroscopic data such as rotationally resolved spectra, rovibrational transition energies, dissociation energies, and virial coefficients; (iii) a good functional form for interpolating the PES between the computed *ab initio* points, and (iv) an

accurate method for predicting the experimental observables from the fitted potential. It should be noted that the accuracy of the generated morphed PES is directly related to the range and quality of the available experimental data.

The generation of accurate interaction potential energy surfaces, of isolated dimers of weakly bound complexes, is indispensable in understanding weak binding due to intermolecular forces. Also, the applicability of this approach to higher vibrational dimensionality, and the transferability of empirical parameters between different systems is a theoretical challenge that will be addressed in this dissertation. In this dissertation, selected systems have been chosen to be studied based on the availability of varied and accurate sets of experimental data.

1.1 Aims

The first aim of this dissertation is to generate accurate and reliable morphed interaction potential energy surfaces of the systems: Ne:HCl, OC:HF, OC:HCl, OC:HBr, OC:HI, and HI:CO_2. These systems are prototype systems used to study van der Waals and hydrogen bond interactions. A comprehensive study on the interaction potential of these systems will provide a fundamental perspective on the influence of different intermolecular forces. The second aim is the development of a new method to generate morphed interaction potentials of weakly bound complexes, where the empirical parameters may be transferable and applied to other systems. Lastly, the third aim is the

extension of the potential morphing method from four-dimension to six-dimension, in order to have a complete treatment of four-atom systems.

2. PREVIOUS WORK ON POTENTIAL MORPHING METHODOLOGY*

Even though different morphing methods have been developed they all have the same objective: achieving agreement with experimental data by making changes to a computed PES so that the average deviation is minimized [16]. There have been a number of advances since the early work on morphing intermolecular *ab initio* potentials of weakly bound complexes by Meuwly and Hutson, on the Ne:HF system [16], and Lucchese, Bevan, and coworkers, on Ar:HI [17]. The method of Meuwly and Hutson involved scaling functions for both the energy and intermolecular distance. The morphing transformation being formulated [16] as

$$V_{\text{morphed}}\left(R,\theta\right) = \nu\left(R,\theta\right) V_{ab\ initio}\left(\rho\left(\theta\right)\cdot R,\theta\right). \tag{1}$$

With the aim of determining the functions $\nu(R,\theta)$ and $\rho(\theta)$, giving it an optimal fit to the experimental data. This method was later applied to He:OCS [18], which is a system of higher dimension but the treatment was limited to two-dimensions.

In contrast, the approach of Lucchese, Bevan, and coworkers was formulated to involve scaling parameters for both the energy and intermolecular distance, as well as a potential shifting factor [17]. In this approach the *ab initio* PES is morphed as

$$V_{\text{morphed}}\left(R,\theta\right) = c_1 V_{ab\ initio}\left(c_2 R + c_3,\theta\right), \tag{2}$$

*Reproduced with permission from "A parameterized compound-model chemistry for morphing the intermolecular potential of OC-HCl" by L.A. Rivera-Rivera, R.R. Lucchese, J.W. Bevan, Chemical Physics Letters 460 (2008) 352-358. Copyright 2008 Elsevier.

where c_1 and c_2 are the scaling parameters for the energy and intermolecular distance respectively, and c_3 is the potential shifting parameter. These three parameters were then optimized to obtain the best fit of the spectroscopic constants of available experimental data. This approach was later improved by adding the factor R_f and using scaling and shifting functions expanded in Legendre polynomials of the form [19-22]

$$V_{\text{morphed}}\left(R,\theta\right)=S_1\left(\theta\right)V_{ab\ initio}\left\{S_2\left(\theta\right)\left(R-R_f\right)+\left[1+S_3\left(\theta\right)\right]R_f,\theta\right\}, \tag{3}$$

where

$$S_\alpha\left(\theta\right)=\sum_i C_{\alpha,i}P_i\left(\cos\theta\right). \tag{4}$$

The factor R_f was found to make the scaling (S_2) and shifting (S_3) functions less strongly correlated [19-22].

Subsequently, Lucchese, Bevan, and coworkers developed a three-dimensional morphing method for Ar:HBr, Kr:HBr, and Ne:HCl systems [23-27]. In this method, the *ab initio* PES is morphed into the form

$$V_{\text{morphed}}\left(R,\theta,r\right)=S_1\left(\theta,r\right)V_{ab\ initio}\left\{S_2\left(\theta,r\right)\left(R-R_f\right)+\left[1+S_3\left(\theta,r\right)\right]R_f,\theta,r\right\}, \tag{5}$$

where

$$S_\alpha\left(\theta,r\right)=\sum_{ij} C_{\alpha,i,j}P_i\left(\cos\theta\right)\left[1-\exp\left(-\beta\frac{r-r_e}{r_e}\right)\right]^j. \tag{6}$$

The values of the dimensionless morphing parameters $C_{\alpha,i,j}$ are obtained by minimizing the function in Eq. (7), using a regularized nonlinear least-squares optimization [23].

$$F\left(C_x,\gamma\right)=\sum_{k=1}^{M}\left\{\frac{O_k^{\text{expt}}-O_k^{\text{calc}}\left(C_x\right)}{\sigma_k}\right\}^2+\gamma^2\sum_x\left(C_x-C_x^{(0)}\right)^2 \tag{7}$$

In Eq. (7), γ is the regularization parameter, σ_k are the uncertainties in either the observed or computed values, the C_x are the $C_{\alpha,i,j}$, and the $C_x^{(0)}$ are the $C_{\alpha,i,j}^{(0)}$; of which $C_{\alpha,i,j}^{(0)}$ are the morphing parameters which correspond to no morphing. The quality of the fit of the experimental data is characterized by the root mean square (RMS) deviation from the experimental data

$$G\left(\gamma\right)=\left\{\frac{1}{M}\sum_{k=1}^{M}\left[\frac{O_k^{\text{expt}}-O_k^{\text{calc}}\left(C_x\right)}{\sigma_k}\right]^2\right\}^{1/2}, \tag{8}$$

where the C_x are the $C_{\alpha,i,j}$. The value of $G(\gamma = \infty)$ is the deviation, from the experimental data, of the observables predicted from the *ab initio* potential (i.e., the unmorphed potential). On the other hand, the value of $G(\gamma = 0)$ would be the quality of the fit for the unconstrained or "nonregularized" fit of the potential.

More recently, Lucchese, Bevan, and coworkers have further developed the method to morph interaction potentials of two linear rigid rotors, hereafter referred to as the potential coordinated morphing (PCM) method. In this particular approach the *ab initio* potential is morphed using the transformation [28-30]

$$\begin{aligned}V_{\text{morphed}}\left(R,\theta_1,\theta_2,\phi\right)=S_1\left(\theta_1,\theta_2,\phi\right)V_{ab\,initio}\left\{S_2\left(\theta_1,\theta_2,\phi\right)\left(R-R_{\text{f}}\right)\right.\\ \left.+\left[1+S_3\left(\theta_1,\theta_2,\phi\right)\right]R_{\text{f}},\theta_1,\theta_2,\phi\right\},\end{aligned} \tag{9}$$

where

$$S_\alpha\left(\theta_1,\theta_2,\phi\right)=\sum_i C_{\alpha,i}F_{\lambda\alpha,i}\left(\theta_1,\theta_2,\phi\right). \tag{10}$$

In Eq. (10), $C_{\alpha,i}$ are the morphing parameters obtained by a regularized nonlinear least-squares optimization [23] while F_λ are angular morphing functions characterized by five parameters, represented by the index $\lambda = \left(l_x,n,\theta_1',\theta_2',\phi'\right)$, and defined so that they approach Dirac delta function as l_x increases. They are given by [28]

$$F_\lambda\left(\theta_1,\theta_2,\phi\right)=\left[N_\lambda\sum_{l_1=0}^{l_x}\sum_{l_2=0}^{l_x}\sum_{l=|l_1-l_2|}^{l_1+l_2} I_{l_1,l_2,l}\left(\theta_1,\theta_2,\phi\right)\, I_{l_1,l_2,l}\left(\theta_1,\theta_2,\phi\right)\right]^n, \tag{11}$$

where the $I_{l_1,l_2,l}\left(\theta_1,\theta_2,\phi\right)$ functions are related to the angular expansion functions defined by [34]

$$I_{l_1,l_2,l}\left(\theta_1,\theta_2,\phi\right)=\sum_m\left\langle l_1,m,l_2,-m\,|\,l,0\right\rangle \mathrm{Y}_{l_1,m}\left(\theta_1,\phi\right)\mathrm{Y}_{l_2,-m}\left(\theta_2,\phi\right). \tag{12}$$

Even more recently Higgins and Klemperer have applied an alternative approach to the He:CH_3F complex [31]. The method involves scaling of the correlation energy to correct the MP4 potential. In this method, the morphed potential is constructed in the form

$$V_{\text{morphed}}\left(R,\theta,\phi\right)=E_{\text{int}}^{\text{HF}}\left(R,\theta,\phi\right)+\sum_{l=0}^{n}c_l P_l(\cos\theta)\left[E_{\text{int}}^{\text{MP4}}\left(R,\theta,\phi\right)-E_{\text{int}}^{\text{HF}}\left(R,\theta,\phi\right)\right], \tag{13}$$

where c_l are morphing coefficients obtained by a nonlinear least-squares optimization [31].

3. THEORETICAL METHODOLOGIES*

3.1 *Ab initio* calculations of the interaction potentials

For two interacting monomers, the interaction potential can be expressed in terms of Jacobi coordinates. For an atom-diatom system, Figure 1(a), R is the distance from the atom to the center of mass of the diatom. The θ angle describes the orientation of the diatom and r is the diatom bond length. In the case of two linear rigid rotors, Figure 1(b), R is the distance between the center of mass of the two monomers. The angles θ_1 and θ_2 describe the orientation of the interacting monomers and the dihedral angle ϕ describes the relative internal orientation of both monomer components. For the six-dimensional interaction potential of the diatom-diatom system, Figure 1(c), R is the distance between the center of mass of the two monomers. The monomers' bond lengths are described by r_1 and r_2. The angles θ_1 and θ_2 describe the orientation of the interacting monomers and the dihedral angle ϕ describes the relative internal orientation of both monomer components.

---

*Reproduced in part with permission from: "A three-dimensional morphed potential of Ne-HCl including the ground state deuterated Σ bending vibration" by L.A. Rivera-Rivera, B.A. McElmurry, S.P. Belov, R.R. Lucchese, J.W. Bevan, Chemical Physics Letters 444 (2007) 9-16. Copyright 2007 Elsevier. "A parameterized compound-model chemistry for morphing the intermolecular potential of OC-HCl" by L.A. Rivera-Rivera, R.R. Lucchese, J.W. Bevan, Chemical Physics Letters 460 (2008) 352-358. Copyright 2008 Elsevier. "A four-dimensional compound-model morphed potential for the OC:HBr complex" by L.A. Rivera-Rivera, R.R. Lucchese, J.W. Bevan, Physical Chemistry Chemical Physics 12 (2010) 7258-7265. http://pubs.rsc.org/en/Content/ArticleLanding/2010/CP/C000972E Reproduced by permission of the PCCP Owner Societies.

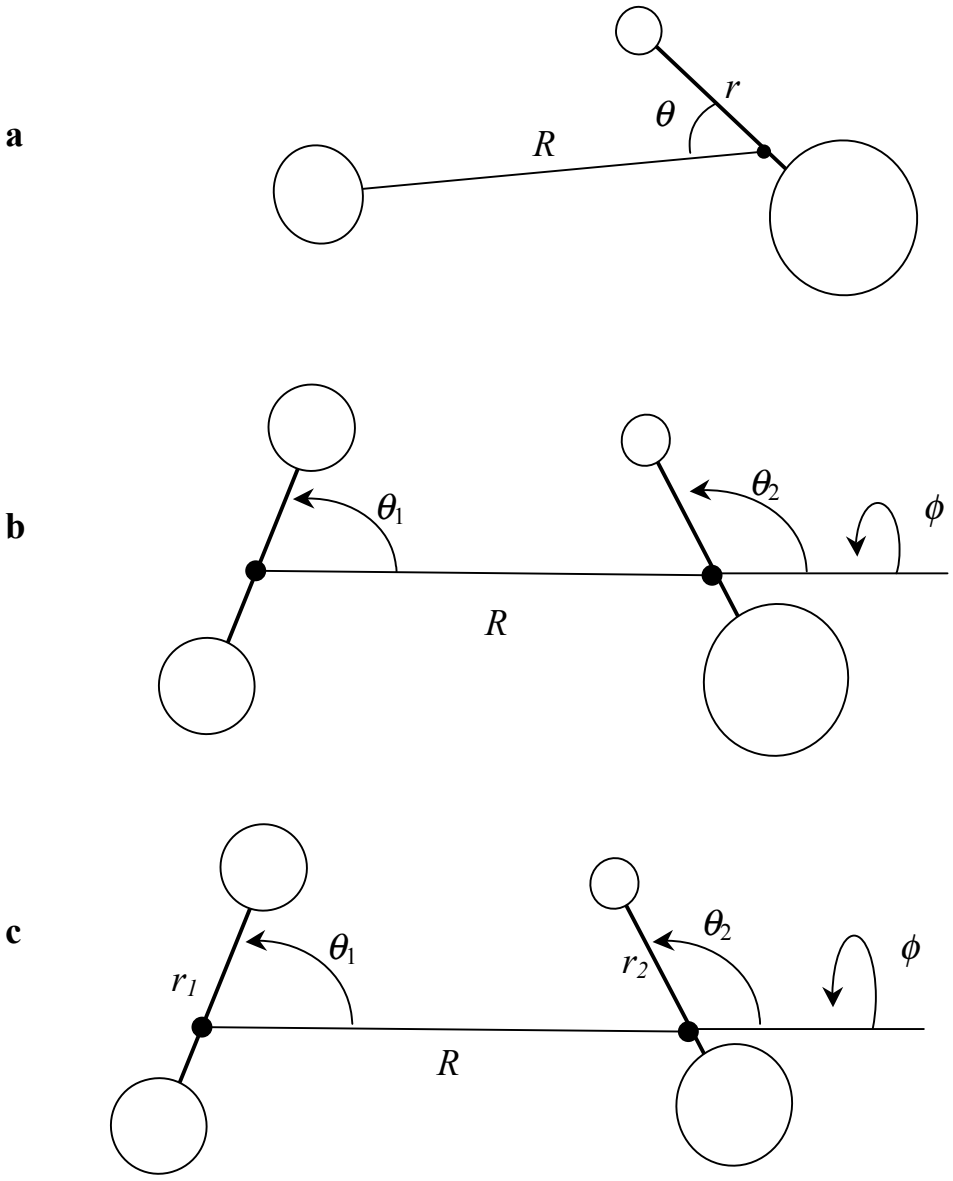

Figure 1. The Jacobi coordinates for different weakly bound systems. In Figures 1(b) and 1(c), the θ_1 angle correspond to the CO or CO_2 monomer, and the θ_2 angle to the HX (X = F, Cl, Br, I) monomer.

The non-relativistic *ab initio* interaction energies of the complexes were calculated using the MOLPRO 2006 and 2009 electronic structure packages [35,36]. The augmented correlation consistent polarized valence N-ζ basis set (aug-cc-pVNZ) was used, where the N represents triple (T), quadruple (Q), or quintuple (5) functions [37-39]. Also for the heavy atoms such as iodine the effective core potential (aug-cc-pVNZ-pp) has been used. The *ab initio* potentials calculated are: (i) coupled cluster singles and doubles with perturbative triples (CCSD(T)/aug-cc-pVNZ), (ii) Moller-Plesset second order (MP2/aug-cc-pVNZ), and (iii) Hartree-Fock (HF/aug-cc-pVNZ). All the interaction energies were then corrected for the basis set superposition error (BSSE), using the counterpoise (CP) method of Boys and Bernardi [40]. The CCSD(T)/aug-cc-pVNZ potential without the CP correction was also calculated. In addition, relativistic correction has been calculated at the Hartree-Fock level of theory (HF/aug-cc-pVNZ-DK CP corrected [41]) using a second order Douglas-Kroll-Hess Hamiltonian (DKH2) [42,43] available on MOLPRO.

3.2 Fitting of the *ab initio* potentials

For an atom-diatom system the computed interaction energies were then fitted to an analytical form, using a three-dimensional interpolation function, based on the Hilbert space reproducing kernel (HSRK) of Ho and Rabitz [44]. The fitting function used for the *R* direction was the distance-like HSRK of the form

$$q_1^{2,6}\left(R,R'\right)=\frac{1}{14R_>^7}\left\{1-\frac{7}{9}\frac{R_<}{R_>}\right\}. \tag{14}$$

Eq. (14) behaves asymptotically as $1/R^7$, and if a continuous set of HSRK is used it will yield the correct functional form of the potential ($1/R^6$). An angle-like HSRK was used for the θ direction, given by

$$q_2^2\left(y,y'\right)=1+y_>y_<+2y_<^2y_>\left\{1-\frac{1}{3}\frac{y_<}{y_>}\right\}, \tag{15}$$

where $y\left(\theta\right)=\left(1-\cos\theta\right)/2$. Lastly, in the r direction the angle-like HSRK $q_2^2\left(z,z'\right)$ was used, where $z\left(r\right)=1-\exp\left[-\left(r/r_\mathrm{e}\right)\right]$ and r_e is the equilibrium bond length of the diatom [23]. In Eqs. (14) and (15) the $x_>$ and $x_<$ (x = R and y) are respectively the larger and smaller of x and x'.

Then the fitted potential is obtained as [23]

$$V^{\mathrm{int}}\left(R,\theta,r\right)=\sum_{ijk}Q_{ijk}\left(R,\theta,r\right)C_{ijk}. \tag{16}$$

The $Q_{ijk}\left(R,\theta,r\right)$ in Eq. (16) are the three-dimensional orthogonalized fitting functions defined as [23]

$$Q_{ijk}\left(R,\theta,r\right)=\bar{q}_{1,i}^{2,6}\left(R\right)\bar{q}_{2,j}^{2}\left(y\left(\theta\right)\right)\bar{q}_{2,k}^{2}\left(z\left(r\right)\right). \tag{17}$$

In addition, the expansion coefficients, C_{ijk} in Eq. (16) can be obtained by the matrix multiplication of $Q_{ijk}\left(R_{i'},\theta_{j'},r_{k'}\right)$ and $V^{\mathrm{int}}\left(R_{i'},\theta_{j'},r_{k'}\right)$ [23].

In order to have a global representation of the interaction potential, for two linear rigid rotors, the calculated *ab initio* points at each value of R_i, were fitted to the spherical expansion [45-47]

$$V_{\Lambda}\left(R_i,\theta_1,\theta_2,\phi\right)=\sum_{\Lambda}\nu_{\Lambda,i}A_{\Lambda}\left(\theta_1,\theta_2,\phi\right). \tag{18}$$

In Eq. (18), Λ is a collective symbol for the quantum numbers $\{L_1,L_2,L\}$, $\nu_{\Lambda,i}$ are the expansion coefficients [34,45], and $A_{\Lambda}\left(\theta_1,\theta_2,\phi\right)$ is given by Eq. (19) [45].

$$\begin{aligned}A_{\Lambda}\left(\theta_1,\theta_2,\phi\right)=&\sum_{M=0}^{\min\left(L_1,L_2\right)}\left(-1\right)^{M}\left(2-\delta_{M,0}\right)\left\langle L_1,M;L_2,-M\mid L,0\right\rangle\left[\frac{\left(L_1-M\right)!\left(L_2-M\right)!}{\left(L_1+M\right)!\left(L_2+M\right)!}\right]^{1/2}\\&\times P_{L_1}^{|M|}\left(\cos\theta_1\right)P_{L_2}^{|M|}\left(\cos\theta_2\right)\cos\left(M\phi\right)\end{aligned} \tag{19}$$

An accurate representation of the interaction potential, for the systems studied in this work, can be obtained by using 55 angular functions. These are defined in Eq. (19), with $L_1 = L_2 = 0, 2, 3, 4$; $L = 0, 2, \ldots, (L_1+L_2)$; and where L_1+L_2+L is an even number. The expansion coefficients in Eq. (18) can be evaluated by a standard least-squares procedure [45,48], that minimizes

$$I_{4D}=\sum_{\varsigma}W_{\varsigma}\left(V\left(R_i,\theta_{1,\varsigma},\theta_{2,\varsigma},\phi_{\varsigma}\right)-\sum_{\Lambda}\nu_{\Lambda,i}A_{\Lambda}\left(\theta_{1,\varsigma},\theta_{2,\varsigma},\phi_{\varsigma}\right)\right)^2. \tag{20}$$

In Eq. (20) W_{ς} is the weight function of the *ab initio* points in the fitting, given by [45]

$$W_{\varsigma}=\frac{1}{1+\left(V\left(R_i,\theta_{1,\varsigma},\theta_{2,\varsigma},\phi_{\varsigma}\right)-E_{\min}\right)\Big/F_w}, \tag{21}$$

where $E_{\min}$ is the minimum value of $V\left(R_i,\theta_1,\theta_2,\phi\right)$, and F_w is the weight factor parameter.

The four–dimensional potential was then obtained by interpolating the angular potential, on the grid of R_i points at fixed angular coordinates, using a one-dimensional radial reproducing kernel [28] of the form

$$\ln\left[\frac{V\left(R,\theta_1,\theta_2,\phi\right)+V_{\min}}{V_{\min}}\right]=\sum_i \alpha_i\left(\theta_1,\theta_2,\phi\right)q_1^{2,6}\left(R_i,R\right), \tag{22}$$

where $q_1^{2,6}\left(R_i,R\right)$ is the one-dimensional distance-like HSRK, Eq. (14). In Eq. (22), the expansion coefficients are then defined by [49]

$$\alpha_i\left(\theta_1,\theta_2,\phi\right)=\sum_{i'}\ln\left[\frac{V_{\mathrm{A}}\left(R_{i'},\theta_1,\theta_2,\phi\right)+V_{\min}}{V_{\min}}\right]\left[q_1^{2,6}\left(R_{i'},R_i\right)\right]^{-1}. \tag{23}$$

In the case of the six-dimensional interaction potential of a diatom-diatom system, the *ab initio* points were interpolated in a way similar to the four-dimensional case. At each value of R_i, $r_{1,j}$, and $r_{2,k}$ the angular potential was fitted to the spherical expansion [47,50]

$$V_{\mathrm{A}}\left(R_i,r_{1,j},r_{2,k},\theta_1,\theta_2,\phi\right)=\sum_{\Lambda}\nu_{\Lambda,ijk}\left(\theta_1,\theta_2,\phi\right)A_{\Lambda}\left(\theta_1,\theta_2,\phi\right). \tag{24}$$

The expansion coefficients $\nu_{\Lambda,ijk}\left(\theta_1,\theta_2,\phi\right)$ are evaluated by an interpolating moving least-squares procedure [51], that minimizes

$$I_{6\mathrm{D}}=\sum_{\zeta}W_{\zeta}\left(\theta_1,\theta_2,\phi\right)\left(V\left(R_i,r_{1,j},r_{2,k},\theta_{1,\zeta},\theta_{2,\zeta},\phi_{\zeta}\right)-\sum_{\Lambda}\nu_{\Lambda,ijk}\left(\theta_1,\theta_2,\phi\right)A_{\Lambda}\left(\theta_{1,\zeta},\theta_{2,\zeta},\phi_{\zeta}\right)\right)^2. \tag{25}$$

In Eq. (25) $W_\zeta\left(\theta_1,\theta_2,\phi\right)$ is the weight function of the *ab initio* points in the fitting and is given by

$$W_\zeta\left(\theta_1,\theta_2,\phi\right)=\frac{\exp\left(-\chi d_\zeta^2\right)}{\left(d_\zeta^n+\varepsilon\right)}, \tag{26}$$

where the parameters χ and n control the rate of attenuation of the weight function, and ε removes the singularity that would otherwise be present as $d_\zeta \to 0$. In order for the fitting functions to provide an interpolation, i.e. reproduce the data that are being fitted, the weight function should go to infinity at each $\left(\theta_{1,\zeta},\theta_{2,\zeta},\phi_\zeta\right)$ point and must attenuate rapidly to minimize the influence of remote points. In Eq. (26) d_ζ is the Euclidean distance function given by

$$d_\zeta\left(\theta_1,\theta_2,\phi\right)=\sqrt{\left(\theta_1-\theta_{1,\zeta}\right)^2+\left(\theta_2-\theta_{2,\zeta}\right)^2+\min\left[\left(\phi-\phi_\zeta\right)^2,\left(2\pi-\left|\phi-\phi_\zeta\right|\right)^2\right]}. \tag{27}$$

The radial potential is obtained by interpolating the angular potential, on the grid of R_i points, at each value of $r_{1,j}$ and $r_{2,k}$, at fixed angular coordinates, using a one-dimensional radial reproducing kernel of the form

$$\ln\left\{\frac{V\left(R,r_{1,j},r_{2,k},\theta_1,\theta_2,\phi\right)+\left[\left|V_{\min}\right|+V_{\mathrm{M}}\right]}{\left[\left|V_{\min}\right|+V_{\mathrm{M}}\right]}\right\}=\sum_i \alpha_{i,j,k}\left(\theta_1,\theta_2,\phi\right)\, q_1^{n,m}\left(R_i,R\right). \tag{28}$$

In Eq. (28) $\left|V_{\min}\right|$ represents the absolute value of the minimum of $V_{\mathrm{A}}\left(R,r_{1,j},r_{2,k},\theta_1,\theta_2,\phi\right)$ and V_{M} is a real positive parameter. The function $q_1^{n,m}$ in Eq. (28) is the nth-order one-dimensional radial reproducing kernel [44]. The order n and the smoothness m of $q_1^{n,m}$

are chosen such that the interpolation functions have the correct asymptotic form of the potential energy surface. The expansion coefficients in Eq. (28) are then defined by [45]

$$\alpha_{i,j,k}\left(\theta_1,\theta_2,\phi\right)=\sum_{i'}\ln\left\{\frac{V_{\mathrm{A}}\left(R_{i'},r_{1,j},r_{2,k},\theta_1,\theta_2,\phi\right)+\left[\left|V_{\min}\right|+V_{\mathrm{M}}\right]}{\left[\left|V_{\min}\right|+V_{\mathrm{M}}\right]}\right\}\left[q_1^{n,m}\left(R_{i'},R_i\right)\right]^{-1}. \tag{29}$$

3.3 Calculation of rovibrational energy levels

The rovibrational energy levels for an atom-diatom system were computed using the variational method previously described [23,52-55]. In the space-fixed frame, and using the Jacobi coordinates, (Figure 1(a)) the rovibrational Hamiltonian is then [23,52]

$$H\left(R,\theta,r\right)=\left(\frac{-\hbar^2}{2\mu R}\right)\left(\frac{\partial^2}{\partial R^2}\right)R-\left(\frac{\hbar^2}{2\mu' r}\right)\left(\frac{\partial^2}{\partial r^2}\right)r+\frac{l^2}{2\mu R^2}+\frac{j^2}{2\mu' r^2}+V\left(R,\theta,r\right), \tag{30}$$

where j^2 and l^2 are the rotational angular momentum operators associated with the rotation of **r** and **R** respectively. The total angular momentum of the system is given by **J** = **j** + **l**. In Eq. (30) μ is the reduce mass of the atom-diatom complex and μ' is the reduce mass of the diatom. In order to simplify the Hamiltonian in Eq. (30), the diatom stretching motion was adiabatically separated from the bending and stretching motions of the complex. By doing this separation Eq. (30) becomes [23,52]

$$H\left(R,\theta\right)=\left(\frac{-\hbar^2}{2\mu R}\right)\left(\frac{\partial^2}{\partial R^2}\right)R+\frac{l^2}{2\mu R^2}+B_{\upsilon}j^2+V^{(\upsilon)}\left(R,\theta\right), \tag{31}$$

where $V^{(\upsilon)}(R,\theta)$ represents the intermolecular potential of the whole complex, averaged over the diatom vibrational states, and B_υ is the diatom rotational constant for the vibrational state υ.

At each value of R and θ, the energy of the diatom stretching state $E_\upsilon(R,\theta)$ was determined. This energy then became the potential for the determination of the bending and stretching motion of the complex. The intermolecular rovibrational wave function was computed using a space-fixed frame, with the radial functions expanded in a distributed Gaussian basis set. The radial functions were evenly distributed from R_{start} (the first point of the radial grid) to R_{end} (the last point of the radial grid), while the angular basis set contained an expansion of the rotational wave function of the diatom monomer using states up to $j_{\max}$. All possible end-over-end rotational states, consistent with the value of $j_{\max}$ and the value of the total angular momentum of a given state, were included while the rovibrational states were computed in two steps. Initially, a vibrational self-consistent field (VSCF) calculation was performed in which the angular state was computed in an angular potential. This was obtained from the full intermolecular potential by averaging over the ground radial vibrational state. The radial state was obtained from a one-dimensional vibrational calculation. In turn, the potential was determined from the full intermolecular potential averaged over the bending state, and the VSCF equations were solved iteratively. The converged VSCF bending and stretching wave functions were then combined in a direct product basis set which was used in a vibrational configuration interaction (VCI) calculation for the final

rovibrational states. Derivatives of the rovibrational eigenvalues, with respect to the morphing parameters, were computed using the Hellmann-Feynman theorem. The rotational constants used in the Hamiltonian, for the diatomic fragments, were taken to be the same as for the isolated molecules.

In the simplest approximation for two interacting linear rotors, the vibrational problem is reduced to a four-dimensional problem. This is done by freezing the intramolecular modes. Within this approximation, the rovibrational energy levels were calculated by the pseudo-spectral approach discussed previously [45,56]. In the two-angle embedded frame, the Hamiltonian of two interacting linear rigid rotors can be expressed as [57]

$$H\left(R,\theta_1,\theta_2,\phi\right) = T_1 + T_2 + \left(\frac{-\hbar^2}{2\mu_{1,2}R^2}\right)\frac{\partial}{\partial R}R^2\frac{\partial}{\partial R} + \left(\frac{1}{2\mu_{1,2}R^2}\right)\left[J^2 + j^2 - 2\mathbf{j}\cdot\mathbf{J}\right], \\ + V\left(R,\theta_1,\theta_2,\phi\right) \tag{32}$$

where

i) $\mu_{1,2}$ is the dimer reduced mass,

ii) $T_i = B_{0i}(j_i)^2$ (i = 1, 2) are the kinetic energy expression for the rotational motion of monomers 1 and 2 with rotational angular momenta $\mathbf{j}_1$ and $\mathbf{j}_2$, and rotational constants B_{0i},

iii) $\mathbf{j} = \mathbf{j}_1 + \mathbf{j}_2$ is the coupled internal rotational angular momentum,

iv) and $\mathbf{J} = \mathbf{l} + \mathbf{j}$ is the total angular momentum of the system ($\mathbf{l}$ is the angular momentum for the rotation about the center of mass of the complex).

In the pseudo-spectral approach, the Hamiltonian in Eq. (32) was split into six contributing terms [45,56]

$$H\left(R,\theta_1,\theta_2,\phi\right) = T_1 + T_2 + T_R + T_{\mathrm{DD}} + H_{\mathrm{OCC}} + V\left(R,\theta_1,\theta_2,\phi\right), \tag{33}$$

where

$$T_R = \left(\frac{-\hbar^2}{2\mu_{1,2}R^2}\right)\frac{\partial}{\partial R}R^2\frac{\partial}{\partial R}, \tag{34}$$

$$T_{\mathrm{DD}} = \left(\frac{1}{2\mu_{1,2}R^2}\right)\left[J^2 + j^2 - 2j_zJ_z\right], \tag{35}$$

and

$$H_{\mathrm{OCC}} = \left(\frac{-1}{2\mu_{1,2}R^2}\right)\left[j_+J_+ + j_-J_-\right]. \tag{36}$$

The T_R term represents the kinetic energy for the stretching motion of the complex, T_{DD} describes the rotational kinetic energy of the dimer, considered as a pseudo diatom, and H_{OCC} represent the off-diagonal Coriolis interaction terms.

Derivatives of the rovibrational eigenvalues with respect to the morphing parameters, were computed using the Hellmann-Feynman theorem. The experimental values of the rotational constants B_{0i} for the isolated monomers were used in the expression of the kinetic energy for all the calculations. The accuracy of the resulting eigenvalues was controlled by the following parameters [45]: R_{start} (the first point of the radial grid), R_{end} (the last point of the radial grid), N_{R} (the number of grid points in the radial direction), N_{θ_1} and N_{θ_2} (the numbers of θ_1 and θ_2 points used in the grid), and N_{ϕ}

(the number of ϕ points). The number of radial functions and the number of radial spectral basis functions are N_F. All of the summations over spectral states are truncated so that $j_1 \le j_{\max_1}$ and $j_2 \le j_{\max_2}$, and where all possible values of m_1 and m_2 were included. The tolerance used to determine the convergence of the eigenvalues in the Lanczos procedure [58] is τ_L. With this set of parameters the absolute energies are converged to 0.01 cm^{-1}.

In the case of the six-dimensional interaction potential of a diatom-diatom system, the monomers' basis functions are obtained from the monomers' RKR potentials [59]. The RKR potentials are fitted to Morse expansions as [60]

$$V_x^{\mathrm{RKR}}\left(r_x\right) = \sum_{s=0}^{N}\left[B_s\left(1-\mathrm{e}^{-\beta\left(r_x - r_{x,e}\right)}\right)^s \right] \text{ for } x = 1 \text{ and } 2\,. \tag{37}$$

Employing a modified Numerov-Cooley approach [61], the radial Schrödinger equation [Eq. (38)] can be solved numerically to obtain the monomer basis functions $\varphi_x^{(\eta)}\left(r_x\right)$.

$$\left[\left(\frac{-\hbar^2}{2\mu_x r_x^2}\right)\frac{\partial}{\partial r_x} r_x^2 \frac{\partial}{\partial r_x} + V_x^{\mathrm{RKR}}\left(r_x\right) - E_\eta^{\mathrm{RKR},x}\right]\varphi_x^{(\eta)}\left(r_x\right) = 0 \quad \text{for } x = 1 \text{ and } 2 \tag{38}$$

In Eq. (38), μ_x is the monomer reduce mass and η indicates the vibrational level which runs from zero to the number of basis functions $\left(N_{\mathrm{NC}} - 1\right)$. The convergence of the Numerov-Cooley method will depend on the following parameters: $r_{1,\mathrm{start}}$ (the first point of the r_1 radial grid), $r_{1,\mathrm{end}}$ (the last point of the r_1 radial grid), $r_{2,\mathrm{start}}$ (the first point of the r_2 radial grid), $r_{2,\mathrm{end}}$ (the last point of the r_2 radial grid), N_{r_1} (the number of grid points in

the r_1 radial direction), and N_{r_2} (the number of grid points in the r_2 radial direction). The vibrational wave functions of the monomers in the complex are then defined as

$$\psi_x^{(\upsilon_x)}\left(r_x\right) = \sum_{\eta=0}^{\left(N_{\mathrm{NC}}-1\right)} c_x^{(\upsilon_x,\eta)} \varphi_x^{(\eta)}\left(r_x\right) \quad \text{for } x = 1 \text{ and } 2\,, \tag{39}$$

where $c_x^{(\upsilon_x,\eta)}$ are the expansion coefficients.

The VSCF calculations, discussed next, can be sped up by pre-calculating all the integrals and matrix elements needed in the calculation. This can be achieved by evaluating the integral of the fitting functions in the r_1 and r_2 radial coordinates over the RKR basis functions. For these two coordinates the angle-like reproducing kernel [44], $q_2^2\left(Z_x, Z_x'\right)$, defined in Eq. (15) was used and the function Z_x is given by

$$Z_x\left(r_x\right) = \frac{\left(r_x - r_{x,\mathrm{start}}\right)}{\left(r_{x,\mathrm{end}} - r_{x,\mathrm{start}}\right)} \quad \text{for } x = 1 \text{ and } 2\,. \tag{40}$$

For each coordinate the set of raw fitting functions, $\left\{q_2^2\left(Z_x, Z_{x_\kappa}\right) : \kappa = j \text{ and } k\right\}$ can be transformed into a set of orthogonal fitting functions by canonical orthogonalization [62]. The matrix **q** is defined as $q_{\kappa\kappa'} = q_2^2\left(Z_{x_\kappa}, Z_{x_{\kappa'}}\right)$ and the matrix **S** is defined by

$$\mathbf{S} = \mathbf{q}^T\mathbf{q}\,. \tag{41}$$

The matrix **S** can be diagonalized by the unitary transformation **U** such that

$$\mathbf{U}^T\mathbf{S}\mathbf{U} = \mathbf{s}\,, \tag{42}$$

where **s** is a diagonal matrix. The canonical transformation matrix is then given by

$$\mathbf{X} = \mathbf{U}\mathbf{s}^{-1/2}\,. \tag{43}$$

The orthogonalized fitting functions are then defined as

$$\bar{q}^2_{2,\kappa}\left(Z_x\right) = \sum_{\kappa'} q^2_2\left(Z_x, Z_{x_{\kappa'}}\right) X_{\kappa'\kappa}\,, \tag{44}$$

and the two-dimensional orthogonalized fitting functions are defined by

$$Q_{jk}\left(r_1, r_2\right) = \bar{q}^2_{2,j}\left(Z_1\right)\bar{q}^2_{2,k}\left(Z_2\right). \tag{45}$$

By defining Ω to be a fixed point in the four-dimensional grid $\left(R, \theta_1, \theta_2, \phi\right)$, then for each value of Ω a two-dimensional potential is determined in the form

$$V\left(\Omega, r_1, r_2\right) = \sum_{jk} C_{jk} Q_{jk}\left(r_1, r_2\right), \tag{46}$$

where the indexes *j* and *k* run over the interpolated $r_{1,j}$ and $r_{2,k}$ points. The expansion coefficients C_{jk} are obtained by simple matrix multiplication

$$C_{jk} = \sum_{j'k'} Q_{jk}\left(r_{1,j'}, r_{2,k'}\right) V\left(\Omega, r_{1,j'}, r_{2,k'}\right), \tag{47}$$

due to the orthogonality of the fitting functions. This procedure avoids the necessity of inverting an ill-conditioned matrix which can occur if the direct product of the original reproducing kernel fitting functions is used. Hence the matrix elements in the VSCF calculation can then be calculated as follows.

$$\begin{aligned}\left\langle \psi_1^{(\upsilon_1)}\left(r_1\right)\middle| V\left(\Omega, r_1, r_2\right)\middle|\psi_1^{(\upsilon_1)}\left(r_1\right)\right\rangle = &\sum_{jk} C_{jk}\bar{q}^2_{2,k}\left(Z_2\right) \\ &\times \sum_{\eta=0}^{\left(N_{\mathrm{NC}}-1\right)}\sum_{\eta'=0}^{\left(N_{\mathrm{NC}}-1\right)} c_1^{(\upsilon_1,\eta)} c_1^{(\upsilon_1,\eta')}\left\langle \varphi_1^{(\eta)}\left(r_1\right)\middle|\bar{q}^2_{2,j}\left(Z_1\right)\middle|\varphi_1^{(\eta')}\left(r_1\right)\right\rangle\end{aligned} \tag{48}$$

$$\left\langle \psi_2^{(\upsilon_2)}(r_2)\middle| V(\Omega,r_1,r_2)\middle|\psi_2^{(\upsilon_2)}(r_2)\right\rangle = \sum_{jk} C_{jk}\bar{q}_{2,j}^2(Z_1) \times \sum_{\eta=0}^{(N_{NC}-1)}\sum_{\eta'=0}^{(N_{NC}-1)} c_2^{(\upsilon_2,\eta)}c_2^{(\upsilon_2,\eta')}\left\langle \varphi_2^{(\eta)}(r_2)\middle|\bar{q}_{2,k}^2(Z_2)\middle|\varphi_2^{(\eta')}(r_2)\right\rangle \quad (49)$$

$$\left\langle \varphi_1^{(\eta)}(r_1)\middle| V^{(\upsilon_2)}(\Omega,r_1)\middle|\varphi_1^{(\eta')}(r_1)\right\rangle = \sum_j C_j \left\langle \varphi_1^{(\eta)}(r_1)\middle|\bar{q}_{2,j}^2(Z_1)\middle|\varphi_1^{(\eta')}(r_1)\right\rangle \quad (50)$$

$$\left\langle \varphi_2^{(\eta)}(r_2)\middle| V^{(\upsilon_1)}(\Omega,r_2)\middle|\varphi_2^{(\eta')}(r_2)\right\rangle = \sum_k C_k \left\langle \varphi_2^{(\eta)}(r_2)\middle|\bar{q}_{2,k}^2(Z_2)\middle|\varphi_2^{(\eta')}(r_2)\right\rangle \quad (51)$$

$$\left\langle \psi_1^{(\upsilon_1)}(r_1)\psi_2^{(\upsilon_2)}(r_2)\middle| V(\Omega,r_1,r_2)\middle|\psi_1^{(\upsilon_1)}(r_1)\psi_2^{(\upsilon_2)}(r_2)\right\rangle = \sum_{jk} C_{jk} \times \sum_{\eta=0}^{(N_{NC}-1)}\sum_{\eta'=0}^{(N_{NC}-1)} \left(c_1^{(\upsilon_1,\eta)}c_1^{(\upsilon_1,\eta')}\left\langle \varphi_1^{(\eta)}(r_1)\middle|\bar{q}_{2,j}^2(Z_1)\middle|\varphi_1^{(\eta')}(r_1)\right\rangle\right) \times \sum_{\eta=0}^{(N_{NC}-1)}\sum_{\eta'=0}^{(N_{NC}-1)} \left(c_2^{(\upsilon_2,\eta)}c_2^{(\upsilon_2,\eta')}\left\langle \varphi_2^{(\eta)}(r_2)\middle|\bar{q}_{2,k}^2(Z_2)\middle|\varphi_2^{(\eta')}(r_2)\right\rangle\right) \quad (52)$$

In Eqs. (48) to (52), the indexes j and k run over the interpolated $r_{1,j}$ and $r_{2,k}$ points, while integrals of the reproducing kernel fitting functions, over the RKR basis sets, can be evaluated using the extended Simpson's rule [62].

In order to simplify the six-dimensional potential in Eq. (28), the stretching motion of the monomers are adiabatically separated from the bending and stretching motions of the complex. By doing this separation, the six-dimensional potential in Eq. (28) becomes $V^{(\upsilon_1,\upsilon_2)}(R,\theta_1,\theta_2,\phi)$ [23,52], (υ_1 is the first monomer vibrational quantum number and υ_2 is the second monomer vibrational quantum number) which represents the intermolecular potential of the complex averaged over the monomers vibrational states.

At each value of Ω the energy of the monomers stretching state, $E_{\upsilon_1}(\Omega)$ and $E_{\upsilon_2}(\Omega)$, are determined by using the VSCF calculation proposed by Bowman [63], solving the Eqs. (53) to (56) iteratively.

$$V^{(\upsilon_2)}(\Omega, r_1) = \left\langle \psi_2^{(\upsilon_2)}(r_2) \middle| V(\Omega, r_1, r_2) \middle| \psi_2^{(\upsilon_2)}(r_2) \right\rangle \tag{53}$$

$$V^{(\upsilon_1)}(\Omega, r_2) = \left\langle \psi_1^{(\upsilon_1)}(r_1) \middle| V(\Omega, r_1, r_2) \middle| \psi_1^{(\upsilon_1)}(r_1) \right\rangle \tag{54}$$

$$\mathbf{H}^{(1)}_{\eta\eta'} = E_{\eta}^{\mathrm{RKR},1}\delta_{\eta\eta'} + \left\langle \varphi_1^{(\eta)}(r_1) \middle| V^{(\upsilon_2)}(\Omega, r_1) \middle| \varphi_1^{(\eta')}(r_1) \right\rangle \tag{55}$$

$$\mathbf{H}^{(2)}_{\eta\eta'} = E_{\eta}^{\mathrm{RKR},2}\delta_{\eta\eta'} + \left\langle \varphi_2^{(\eta)}(r_2) \middle| V^{(\upsilon_1)}(\Omega, r_2) \middle| \varphi_2^{(\eta')}(r_2) \right\rangle \tag{56}$$

Where the potential matrix elements are computed as shown in Eqs. (48) to (51). Then the $V^{(\upsilon_1,\upsilon_2)}(R,\theta_1,\theta_2,\phi)$ potential is determined by

$$\begin{aligned} V^{(\upsilon_1,\upsilon_2)}(\Omega) = {} & \left(E_{\upsilon_1}(\Omega) - E_{\upsilon_1}^{\mathrm{RKR},1}\right) + \left(E_{\upsilon_2}(\Omega) - E_{\upsilon_2}^{\mathrm{RKR},2}\right) \\ & - \left\langle \psi_1^{(\upsilon_1)}(r_1)\psi_2^{(\upsilon_2)}(r_2) \middle| V(\Omega, r_1, r_2) \middle| \psi_1^{(\upsilon_1)}(r_1)\psi_2^{(\upsilon_2)}(r_2) \right\rangle \end{aligned}, \tag{57}$$

where $E_{\upsilon_x}^{\mathrm{RKR},x}$ (x = 1 and 2) are the energies of the monomers stretching state, determined from the monomers RKR potentials and where the potential matrix element is computed using Eq. (52). With an initial guess of the expansion coefficients $c_x^{(\upsilon_x,\eta)}$ (x = 1 and 2), the $\mathbf{H}^{(1)}_{\eta\eta'}$ and $\mathbf{H}^{(2)}_{\eta\eta'}$ matrixes can be diagonalized until the $E_{\upsilon_1}(\Omega)$ and $E_{\upsilon_2}(\Omega)$ energies converge to a given tolerance τ_{VSCF}.

The simplification of a six-dimensional potential to a four-dimensional potential by adiabatically separating the stretching motion of the monomers from the bending and stretching motions of the complex, significantly reduces the difficulty of the rovibrational energy calculations. Within this approximation, the rovibrational Hamiltonian becomes similar to the one used for two interacting linear rotors, Eq. (32), where the vibrational problem is reduced to a four-dimensional problem. Thus, the rovibrational energy levels can be calculated by the pseudo-spectral approach discussed previously [45,56]. Derivatives of the rovibrational eigenvalues, with respect to the morphing parameters, were computed using the Hellmann-Feynman theorem. The rotational constants $B_{\upsilon_x}\left(x = 1, 2\right)$ for monomers 1 and 2, in the vibrational state υ_x, were used in the expression of the kinetic energy for all the calculations. A consequence of the adiabatic approximation is that the value of B_{υ_x} will depend on Ω. To simplify the calculation, the value of B_{υ_x} was calculated at the equilibrium distance R_e, and at fixed angular coordinates as

$$B_{\upsilon_x}\left(R_e, \theta_1^f, \theta_2^f, \phi^f\right) = \frac{\hbar^2}{2\mu_x}\left\langle \psi_x^{(\upsilon_x)} \middle| \frac{1}{r_x^2} \middle| \psi_x^{(\upsilon_x)} \right\rangle \quad \text{for } x = 1 \text{ and } 2\,. \tag{58}$$

3.4 Calculation of the spectroscopic constants

Vibrational frequencies were calculated as the energy differences between the initial and final vibrational states involved in the transition, with the same J value. The

rotation and distortion constants have been calculated from first and second differences of the calculated rovibrational energy levels [23,49]. The expectation values of $\langle P_1(\cos\theta)\rangle$ and $\langle P_2(\cos\theta)\rangle$ were calculated by perturbation theory [23,64], with the perturbation $\delta P_n\left(\cos\theta\right)$, where the expectation value of the given operator $\hat{x}$ was calculated by

$$\left\langle i \mid x \mid i \right\rangle = \frac{1}{\delta}\left(E_i^{(\delta)} - E_i^{(\delta=0)} \right) + O\left(\delta\right). \tag{59}$$

In the present study, a value of δ = 0.01 cm^{-1} was chosen for both P_1 and P_2 expectation values. Finally, the J dependence of $\langle P_2(\cos\theta)\rangle$, D_θ, was calculated by [23]

$$D_\theta^{(J,J-1)} = \frac{1}{2J}\left\{ \left\langle P_2\left(\cos\theta\right)\right\rangle_J - \left\langle P_2\left(\cos\theta\right)\right\rangle_{J-1} \right\}. \tag{60}$$

3.5 Compound model morphing method

In the compound model morphing (CMM) method the potential is generated as

$$\begin{aligned} V_{\mathrm{CMM}}\left(R\right) = {} & C_1\left[V_{\mathrm{MP2}}\left(R'\right)\right]_{\mathrm{QZ}}^{\mathrm{CP}} + C_2\left\{\left[V_{\mathrm{CCSD(T)}}\left(R'\right)\right]_{\mathrm{TZ}}^{\mathrm{CP}} - \left[V_{\mathrm{CCSD(T)}}\left(R'\right)\right]_{\mathrm{TZ}}^{\mathrm{NO\ CP}}\right\} \\ & + C_3\left\{\left[V_{\mathrm{CCSD(T)}}\left(R'\right)\right]_{\mathrm{TZ}}^{\mathrm{CP}} - \left[V_{\mathrm{MP2}}\left(R'\right)\right]_{\mathrm{TZ}}^{\mathrm{CP}}\right\} + C_4\left\{\left[V_{\mathrm{HF/R}}\left(R'\right)\right]_{\mathrm{QZ}}^{\mathrm{CP}} - \left[V_{\mathrm{HF/NR}}\left(R'\right)\right]_{\mathrm{QZ}}^{\mathrm{CP}}\right\} \\ & + C_5\left\{\left[V_{\mathrm{HF}}\left(R'\right)\right]_{\mathrm{5Z}}^{\mathrm{CP}} - \left[V_{\mathrm{HF}}\left(R'\right)\right]_{\mathrm{QZ}}^{\mathrm{CP}}\right\} \end{aligned}, \tag{61}$$

$$R' = C_6\left(R - R_{\mathrm{f}}\right) + \left(1.0 + C_7\right)R_{\mathrm{f}}$$

where the C_α are the unitless morphing parameters. The reference, or unmorphed potential $V_{\mathrm{CMM}}^{(0)}$, is obtained by making C_1 = 1.0, C_2 = 0.0, C_3 = 1.0, C_4 = 1.0, C_5 = 1.0, C_6

= 1.0, and C_7 = 0.0. The morphing parameters C_α are obtained by a regularized nonlinear least-squares optimization [23], and by then minimizing the Eq. (7) were the C_x are the C_α. In Eq. (61) the parameter C_1 is the scaling parameter for the interaction energy of the dimer at the MP2/aug-cc-pVQZ level of theory, including the CP correction for the BSSE. The second term gives the correction for the BSSE at the CCSD(T) level of theory. The third term gives corrections for the correlation energy at the CCSD(T) level of theory. The fourth term gives the relativistic corrections which can be important in a six-dimensional potential, and the fifth term gives corrections for larger basis sets. Lastly, the radial transformation is included, with the parameters C_6 and C_7, to improve the fit of the rotational and distortion constants in the six-dimensional potential. Not all of these parameters are varied in any given morphed potential. The quality of the fit of the experimental data is characterized by the root mean square deviation of the experimental data, Eq. (8), where the C_x are the C_α.

Figure 2 shows the dependence of $G(\gamma)$ on γ for the CMM method, generated by using the OC:HCl data in Table 6. The value of $G(\gamma)$ varies between $G(\gamma = \infty)$ = 22.3 and $G(\gamma = 1)$ = 2.9. The interesting feature of the $G(\gamma)$ vs. γ curve is the break in the curve at $\gamma \leq 40$. This implies that lowering γ below 40 does not lead to further improvement on the fit. Thus, the most reliable morphed potential is obtained when the value of γ is chosen as large as possible, while still consistent with a good fit to the experimental data. Therefore, the value of γ used in the CMM fitting was chosen to be 10.0.

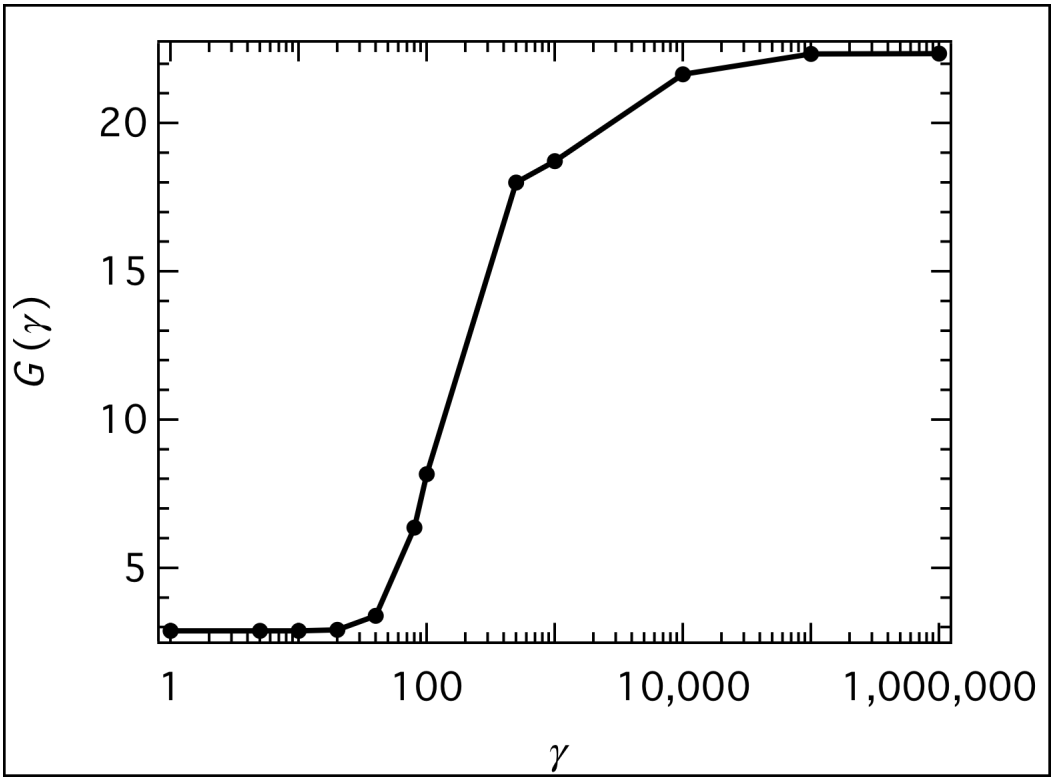

Figure 2. $G(\gamma)$ vs. γ curve for the CMM method. The figure was generated using the OC:HCl data in Table 6. The value of $G(\gamma = \infty) = 22.3$ corresponds to the value of G for the unmorphed potential, $V_{\mathrm{CMM}}^{(0)}$ in Table 6.

The optimal value of σ_k should be the experimental uncertainties of the observables. In general, vibrational frequencies are fitted to 0.01-0.05 cm^{-1}. The P_1 and P_2's expectation values can be fitted to 0.001-0.005. Rotational and distortion constants are normally fitted to 10^{-5} and 10^{-9} of a wavenumber, respectively. However, the specific value of σ_k for each observable depends on the system and the ability of the potential surface to predict each observable. Observables that are accurately predicted can have smaller uncertainties. On the other hand, with observables that are inaccurately predicted, such as distortion constants, should have significantly higher uncertainties. In addition, $1/\sigma_k$ can also be viewed as weights in the least-square procedure. Thus for strongly correlated data, sometimes σ_k must be increased in order to not overweight one type of data. It is important to point out that, since the morphing procedure is a nonlinear least-squares fit, there is always the possibility of other similar or better fits. In order to obtain a unique fit, the experimental data is fitted by adding the data to a least-squares fitting in a sequential manner. The CMM method can be easily applied to systems of any vibrational dimensionality.

4. APPLICATIONS*

In this section, applications of potential morphing methodology are presented for the systems: Ne:HCl, OC:HX (X = F, Cl, Br, I), and HI:CO_2. In section 4.1, the three-dimensional morphing method is applied to the atom-diatom system Ne:HCl. The PCM method for two linear rotors is applied to the system OC:HCl in section 4.2, OC:HI, in section 4.4, and HI:CO_2, in section 4.5. In addition, the CMM method is applied to morph the four-dimensional potential of the OC:HCl (section 4.2) and OC:HBr (section 4.3). Also, a comparison of the PCM and CMM methods is presented in the case of OC:HCl, and the advantages and disadvantages of both methods discussed. Lastly, in section 4.6, the CMM method is used to morphed the six-dimensional potential of OC:HF system. It is noted that the CMM method was not used for the OC:HI and HI:CO_2 systems, because *ab initio* potentials with large basis set are currently

*Reproduced in part with permission from: "A three-dimensional morphed potential of Ne-HCl including the ground state deuterated Σ bending vibration" by L.A. Rivera-Rivera, B.A. McElmurry, S.P. Belov, R.R. Lucchese, J.W. Bevan, Chemical Physics Letters 444 (2007) 9-16. Copyright 2007 Elsevier. "A morphed intermolecular bending potential of OC-HCl" by L.A. Rivera-Rivera, R.R. Lucchese, J.W. Bevan, Chemical Physics Letters 429 (2006) 68-76. Copyright 2006 Elsevier. "A parameterized compound-model chemistry for morphing the intermolecular potential of OC-HCl" by L.A. Rivera-Rivera, R.R. Lucchese, J.W. Bevan, Chemical Physics Letters 460 (2008) 352-358. Copyright 2008 Elsevier. "A four-dimensional compound-model morphed potential for the OC:HBr complex" by L.A. Rivera-Rivera, R.R. Lucchese, J.W. Bevan, Physical Chemistry Chemical Physics 12 (2010) 7258-7265. http://pubs.rsc.org/en/Content/ArticleLanding/2010/CP/C000972E Reproduced by permission of the PCCP Owner Societies. "A ground state morphed intermolecular potential for the hydrogen bonded and van der Waals isomers in OC:HI and a prediction of an anomalous deuterium isotope effect" by L.A. Rivera-Rivera, Z. Wang, B.A. McElmurry, F.F. Willaert, R.R. Lucchese, J.W. Bevan, R.D. Suenram, F.J. Lovas, Journal of Chemical Physics 133 (2010) 184305-13. Copyright 2010 American Institute of Physics. http://jcp.aip.org/resource/1/jcpsa6/v133/i18/p184305_s1 "Microwave-based structure and four-dimensional morphed intermolecular potential for HI-CO_2" by W. Jabs, F.F. Willaert, B.A. McElmurry, L.A. Rivera-Rivera, R. Montuoro, R.R. Lucchese, J.W. Bevan, R.D. Suenram, Journal of Physical Chemistry A 111 (2007) 11976-11985. Copyright 2007 American Chemical Society.

computationally too expensive to be calculated for these systems. Thus, in these cases the PCM method is preferred over the CMM method.

4.1 Ne:HCl

In the Ne:HCl complex, the rovibrational states are labeled using the notation $\left(v_1, v_2^l, v_3\right)_J$, as in linear triatomic molecule. In this notation, the quantum number l describes the vibrational angular momentum of the triatom and it is used with v_2, the bending quantum number, to characterize the bending mode of the complex with the label v_2^l. The quantum number v_1 labels the intramolecular stretch of the diatom H-Cl, and v_3 describes the intermolecular vibrational motion of the complex. Lastly, the quantum number J is the total angular momentum. The Coriolis interactions split the Π states (l = 1) into the ($l = 1^e$ or +1) and ($l = 1^f$ or -1) states, where e and f, or + and -, refer to the parity of the state [65].

Ne-HCl was first observed experimentally in supersonic expansions by Novick et al. [66]. Their results were consistent with the almost free rotation of the HCl molecule within the complex. Barton et al. [67] subsequently investigated ground vibrational state microwave and radiofrequency Stark spectra for Ne-DCl, and a partially resolved rotational spectrum of Ne-HCl was obtained by Prout [68]. Hutson and Howard [69] calculated an anisotropic PES for Ne:HCl, and determined a small barrier to internal rotation in the complex. It was found that PES has a global minimum at the linear Ne-

HCl configuration, and a secondary minimum at the Ne-ClH configuration. Lovejoy and Nesbitt [70] later obtained a near-infrared spectrum of jet-cooled Ne-HCl, reporting the HCl stretching fundamental and three combination bands. The latter included those of the van der Waals stretching and bending modes in the excited state. Subsequently, Hutson [71] calculated a two-dimensional PES for Ne:HCl with HCl in its $v_1 = 1$ state, by least-squares fitting to the near infrared laser spectra. This surface was also characterized by a global minimum at the linear Ne-HCl geometry, and a secondary minimum at the Ne-ClH linear geometry. Schuder et al. [72] later observed the Ne-DCl complex in a slit-jet supersonic expansion, analyzing the mid-infrared absorption spectra for the DCl stretch fundamental, and the DCl bending combination bands. The DCl component was also found to be a nearly free rotor from anomalous intensity patterns for Ne-DCl, which is in contrast to the more restricted librational motion of DCl in Ar-DCl. More recently Rivera-Rivera et al. [27] reported the ground state submillimeter spectrum, of the Σ bending vibration of Ne-DCl, recorded in a coaxially-configured supersonic jet.

Potentials based on ground state *ab initio* calculations are available for the complex [73,74]. Those potentials also indicated a global minimum Ne-HCl and a secondary minimum Ne-ClH. Recently, Jiang et al. [75] performed *ab initio* calculations at the CCSD(T)/aug-cc-pVTZ-332 level of theory and found that Ne-ClH linear geometry is more stable than the Ne-HCl linear geometry, thus contradicting previous studies. However, a further investigation by Cagide Fajín et al. [76] at the CCSD(T)/aug-cc-pV5Z-33211 level of theory attributed the results of Jiang et al. [75] to

the use of an inadequate basis set. This surface was characterized by two linear minima, the global minimum Ne-HCl and the secondary minimum Ne-ClH, with a difference in energy less than 3 cm^{-1}.

Substantial differences exist between the available two-dimensional potentials of Ne:HCl. These discrepancies make the comparison between the potentials for $v_1 = 0$ and $v_1 = 1$ states of HCl difficult and unreliable. Furthermore, it has been claimed that high quality *ab initio* potentials are more reliable than the semi-empirical ones [76]. Consequently, in order to get more insight about the dependence of the potential on the HCl bond length *r*, a three-dimensional surface is indispensable.

In this work, the non-relativistic interaction energy of the Ne:HCl complex was calculated at the CCSD(T)/aug-cc-pVTZ level of theory. The PES was calculated on a grid of 780 points. The HCl bond distance was varied using 6 grid points (1.074552 Å, 1.174552 Å, 1.274552 Å, 1.374552 Å, 1.474552 Å, and 1.574552 Å); the distance Ne-Cl was varied using 13 grid points (3.00 Å, 3.30 Å, 3.40 Å, 3.50 Å, 3.70 Å, 3.80 Å, 3.85 Å, 3.90 Å, 4.00 Å, 4.50 Å, 5.00 Å, 5.50 Å, and 6.00 Å); and the H-Cl-Ne angle was varied using 10 equally spaced points between 0° and 180°.

The fully BSSE corrected three-dimensional PES was obtained using

$$V\left(R,\theta,r\right) = V^{\text{int}}\left(R,\theta,r\right) + V^{\text{HCl}}\left(r\right), \tag{62}$$

where $V^{\text{int}}\left(R,\theta,r\right)$ is the *ab initio* BSSE corrected interaction energy, and $V^{\text{HCl}}\left(r\right)$ the interatomic potential for the isolated HCl molecule. The $V^{\text{HCl}}\left(r\right)$ potential was chosen

to be a one-dimensional Morse potential, defined in Eq. (63) [77] with the parameters [78,79] $2\beta = 2.232932$, $D = 42341.90$ cm^{-1}, and $r_e = 1.274552$ Å.

$$V^{HCl}(r) = D\left[1 - \exp\left(-2\beta\left(\frac{r - r_e}{r_e}\right)\right)\right]^2 \tag{63}$$

The value of the parameters used in the calculation of the rovibrational energy levels were: $N_{RF} = 50$ (the number of radial functions), $R_{start} = 2.70$ Å, $R_{end} = 6.60$ Å, and $j_{max} = 14$. In addition, the rotational constants for the diatomic fragments were taken to be the same as for the isolated molecules: 10.4401992 cm^{-1} [80] for $H^{35}Cl\ (v_1 = 0)$, 10.136228 cm^{-1} [78] for $H^{35}Cl\ (v_1 = 1)$, 5.3922717 cm^{-1} [80] for $D^{35}Cl\ (v_1 = 0)$, 5.27978 cm^{-1} [72] for $D^{35}Cl\ (v_1 = 1)$, and 5.3764902 cm^{-1} [80] for $D^{37}Cl\ (v_1 = 0)$.

The *ab initio* potential was morphed using the transformation described by Eqs. (5) and (6), where R_f was selected to be 3.70 Å and β was chosen to be 1.0. The experimental data used in the morphed potential energy surface of Ne:HCl is shown in Table 1. The data includes previously reported submillimeter, microwave, and infrared (IR) experiments [27,67,70,72]. Rotational constants and centrifugal distortion constants for the states $(1,2^0,0)$, $(1,0^0,1)$, and $(1,1^{1e},0)$ were not included in the fitting because such constants are significantly perturbed by Coriolis interactions. The values of G in Table 1 for the *ab initio* and morphed potentials are $G = 161.1$ and $G = 3.9$ respectively, thus indicating the improvement in the overall agreement with experimental data; obtained from the morphing procedure.

Table 1
Experimental data of Ne:HCl used in the fits and fitted values, and the uncertainties used.

Observable	$V_{ab\ initio}$	V_{morphed}	Exp	Reference	σ_k
^{20}Ne-D^{35}Cl $\{E[(0,2^0,0)_0]- E[(0,0^0,0)_0]\}$/cm^{-1}	13.54	8.41	8.64	[27]	0.05
^{20}Ne-D^{37}Cl $\{E[(0,2^0,0)_0]- E[(0,0^0,0)_0]\}$/cm^{-1}	13.65	8.41	8.61	[27]	0.05
^{20}Ne-H^{35}Cl $\{E[(1,0^0,0)_0]- E[(0,0^0,0)_0]\}$/cm^{-1}	-0.17	0.29	0.30	[70]	0.03
^{20}Ne-D^{35}Cl $\{E[(1,0^0,0)_0]- E[(0,0^0,0)_0]\}$/cm^{-1}	-0.28	0.14	0.31	[72]	0.03
^{20}Ne-H^{35}Cl $\{E[(1,2^0,0)_0]- E[(1,0^0,0)_0]\}$/cm^{-1}	18.86	15.79	15.68	[70]	0.05
^{20}Ne-D^{35}Cl $\{E[(1,2^0,0)_0]- E[(1,0^0,0)_0]\}$/cm^{-1}	13.57	8.30	8.20	[72]	0.05
^{20}Ne-H^{35}Cl $\{E[(1,0^0,1)_0]- E[(1,0^0,0)_0]\}$/cm^{-1}	20.65	20.82	20.85	[70]	0.05
^{20}Ne-H^{35}Cl $\{E[(1,1^{1f},0)_1]- E[(1,0^0,0)_1]\}$/cm^{-1}	25.15	22.95	22.52	[70]	0.05
^{20}Ne-D^{35}Cl $\{E[(1,1^{1f},0)_1]- E[(1,0^0,0)_1]\}$/cm^{-1}	17.92	13.55	13.57	[72]	0.05
^{20}Ne-H^{35}Cl $B[(0,0^0,0)_{1,0}]$/(0.01 cm^{-1})	8.193	9.105	9.111	[69]	0.003
^{20}Ne-D^{35}Cl $B[(0,0^0,0)_{1,0}]$/(0.01 cm^{-1})	8.103	9.006	9.000	[67]	0.003
^{20}Ne-D^{37}Cl $B[(0,0^0,0)_{1,0}]$/(0.01 cm^{-1})	7.958	8.836	8.836	[67]	0.003
^{20}Ne-D^{35}Cl $B[(0,2^0,0)_{1,0}]$/(0.01 cm^{-1})	7.830	8.845	8.855	[27]	0.003
^{20}Ne-D^{37}Cl $B[(0,2^0,0)_{1,0}]$/(0.01 cm^{-1})	7.702	8.729	8.722	[27]	0.003
^{20}Ne-H^{35}Cl $B[(1,0^0,0)_{1,0}]$/(0.01 cm^{-1})	8.146	9.053	9.057	[70]	0.003
^{20}Ne-D^{35}Cl $B[(1,0^0,0)_{1,0}]$/(0.01 cm^{-1})	8.060	8.957	8.949	[72]	0.003
^{20}Ne-H^{35}Cl $B[(1,1^{1f},0)_{2,1}]$/(0.01 cm^{-1})	8.152	9.097	9.091	[70]	0.003
^{20}Ne-D^{35}Cl $B[(1,1^{1f},0)_{2,1}]$/(0.01 cm^{-1})	8.099	9.038	9.040	[72]	0.003
^{20}Ne-H^{35}Cl D_J $[(0,0^0,0)_{2,1,0}]$/(10^{-7} cm^{-1})	36.9	70.0	69.1	[70]	4.0
^{20}Ne-D^{35}Cl D_J $[(0,0^0,0)_{2,1,0}]$/(10^{-7} cm^{-1})	28.7	66.2	61.1	[67]	4.0
^{20}Ne-D^{37}Cl D_J $[(0,0^0,0)_{2,1,0}]$/(10^{-7} cm^{-1})	27.4	63.4	59.0	[67]	4.0
^{20}Ne-D^{35}Cl D_J $[(0,2^0,0)_{2,1,0}]$/(10^{-7} cm^{-1})	21.7	42.4	22.5	[27]	4.0
^{20}Ne -D^{37}Cl D_J $[(0,2^0,0)_{2,1,0}]$/(10^{-7} cm^{-1})	21.9	48.0	24.3	[27]	4.0
^{20}Ne-H^{35}Cl D_J $[(1,0^0,0)_{2,1,0}]$/(10^{-7} cm^{-1})	36.4	69.6	70.4	[70]	4.0
^{20}Ne-D^{35}Cl D_J $[(1,0^0,0)_{2,1,0}]$/(10^{-7} cm^{-1})	28.0	65.4	66.0	[72]	4.0
^{20}Ne-H^{35}Cl D_J $[(1,1^{1f},0)_{3,2,1}]$/(10^{-7} cm^{-1})	50.2	76.0	66.9	[70]	4.0
^{20}Ne-D^{35}Cl D_J $[(1,1^{1f},0)_{3,2,1}]$/(10^{-7} cm^{-1})	47.0	73.8	66.5	[72]	4.0
^{20}Ne-H^{35}Cl $\langle P_1(\cos\theta)\rangle$ for $(0,0^0,0)_0$	0.40	0.19	0.20	[69]	0.03
^{20}Ne-D^{35}Cl $\langle P_1(\cos\theta)\rangle$ for $(0,0^0,0)_0$	0.67	0.34	0.42	[67]	0.03
^{20}Ne-D^{37}Cl $\langle P_1(\cos\theta)\rangle$ for $(0,0^0,0)_0$	0.67	0.36	0.42	[67]	0.03
^{20}Ne-H^{35}Cl $\langle P_2(\cos\theta)\rangle$ for $(0,0^0,0)_0$	0.166	0.085	0.081	[69]	0.004
^{20}Ne-D^{35}Cl $\langle P_2(\cos\theta)\rangle$ for $(0,0^0,0)_0$	0.370	0.175	0.197	[67]	0.004
^{20}Ne-D^{37}Cl $\langle P_2(\cos\theta)\rangle$ for $(0,0^0,0)_0$	0.374	0.181	0.198	[67]	0.004
^{20}Ne-D^{35}Cl $\langle P_2(\cos\theta)\rangle$ for $(0,2^0,0)_0$	0.264	0.417	0.459	[27]	0.004
^{20}Ne-D^{37}Cl $\langle P_2(\cos\theta)\rangle$ for $(0,2^0,0)_0$	0.261	0.415	0.459	[27]	0.004
^{20}Ne-D^{35}Cl $D_\theta^{(1,0)}/10^{-6}$ for $(0,0^0,0)$	17.4	76.4	73.0	[67]	4.0
G	161.1	3.9			

Table 2
Optimized morphing parameters $C_{\alpha,i,j}$ and their corresponding uncertainties for Ne:HCl.

(α,i,j)	$C_{\alpha,i,j}$	$C^{(0)}_{\alpha,i,j}$	σ
(1,0,0)	1.5339	1.0	0.0060
(1,0,1)	-1.2605	0.0	0.0352
(2,0,0)	(1.0)	1.0	Constrained
(2,1,0)	0.1767	0.0	0.0014
(2,2,0)	0.1314	0.0	0.0027
(3,0,0)	0.0893	0.0	0.0001
(3,1,0)	0.0195	0.0	0.0003
(3,2,0)	0.0222	0.0	0.0006

Table 3
Correlation matrix of the morphing parameters ($C_{\alpha,i,j}$) for Ne:HCl.

(α,i,j)	(1,0,0)	(1,0,1)	(2,1,0)	(2,2,0)	(3,0,0)	(3,1,0)	(3,2,0)
(1,0,0)	1.00						
(1,0,1)	-0.38	1.00					
(2,1,0)	0.37	-0.18	1.00				
(2,2,0)	0.29	-0.19	0.54	1.00			
(3,0,0)	-0.45	0.12	-0.07	0.47	1.00		
(3,1,0)	0.47	-0.09	0.47	-0.36	-0.66	1.00	
(3,2,0)	0.33	-0.12	0.34	0.88	0.26	-0.43	1.00

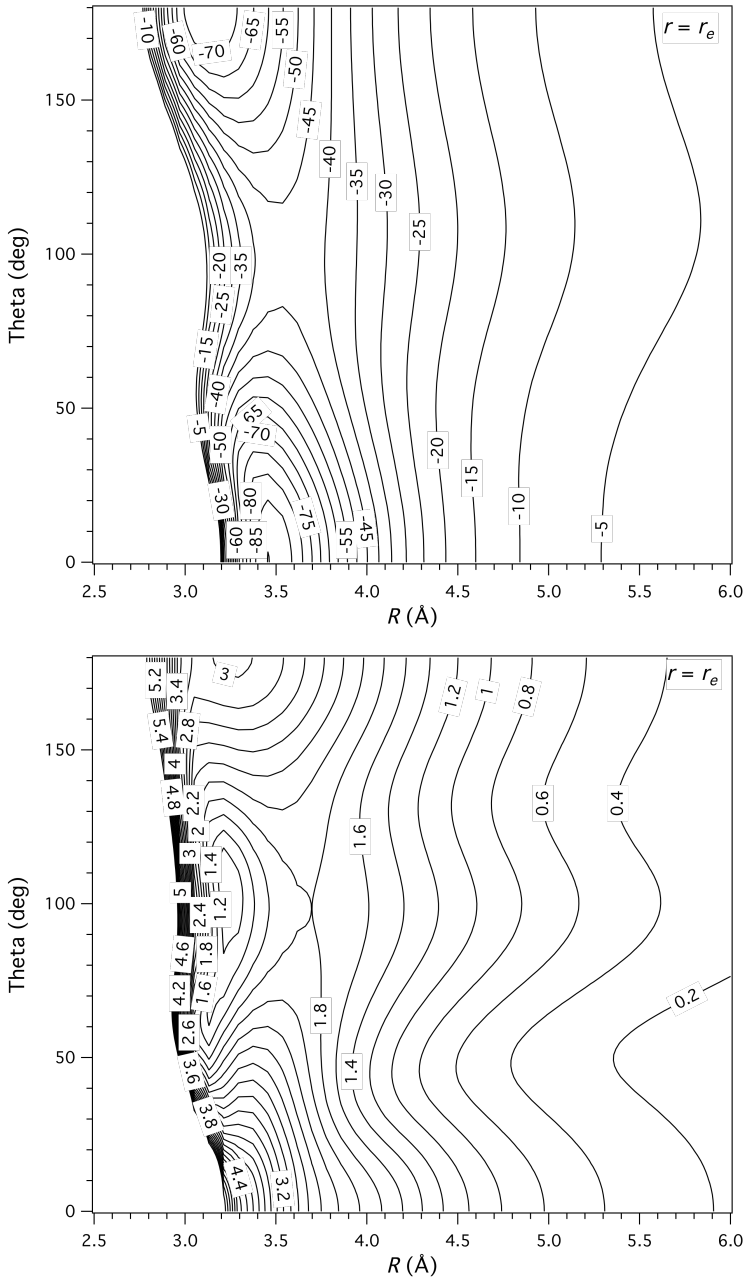

Figure 3. Morphed interaction potential of Ne:HCl. A two-dimensional cut of the morphed interaction potential is shown in the top of the figure. The corresponding statistical uncertainties relative to the value of the potential, at infinite separation, are shown in the bottom of the figure. All contours are given in cm^{-1}. The coordinates used (R,θ,r) are the Jacobi coordinates for the $^{20}Ne:H^{35}Cl$ isotopomer, defined in Figure 1(a).

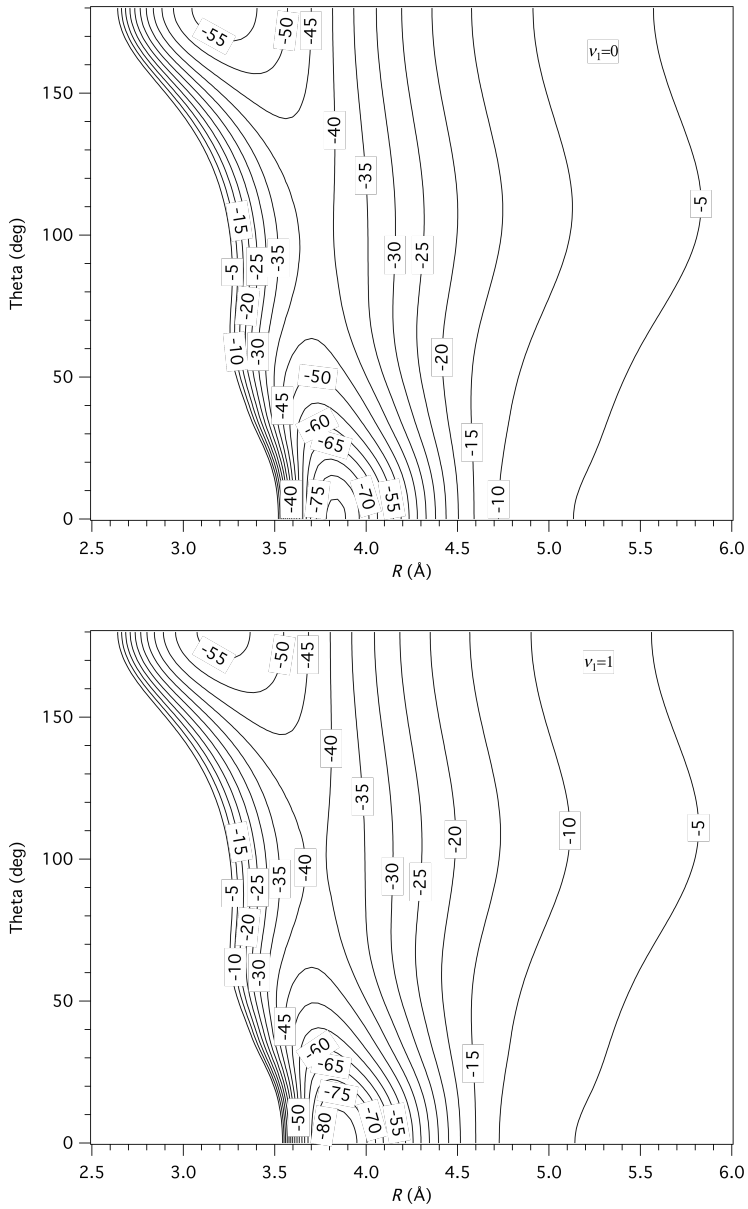

Figure 4. Adiabatic potential surfaces for the ^{20}Ne:H^{35}Cl isotopomer. In the top of the figure, the H-^{35}Cl $v_1 = 0$ surface is shown, and in the bottom, the H-^{35}Cl $v_1 = 1$ surface. All contours are given in cm^{-1}. The coordinates used (R, θ, r) are the Jacobi coordinates defined in Figure 1(a).

Table 4
Features of various Ne:HCl potentials.

Parameter	$V_{\text{morphed}}\left(\nu_1 = 0\right)$	$V_{\text{morphed}}\left(\nu_1 = 1\right)$	M4[a]	M5[a]	H6$\left(\nu_1 = 1\right)$[a]
$V_{\text{min}}(0°)$/cm^{-1}	-81.4	-84.4	-67.36	-68.22	-64.26
$V_{\text{min}}(180°)$/cm^{-1}	-57.5	-56.6	-56.02	-53.50	-56.83
$V_{\text{min}}(0°)$-$V_{\text{min}}(180°)$/cm^{-1}	-23.9	-27.8	-11.34	-14.72	-7.43
Barrier height/cm^{-1}	40.4	44.0	27.16	27.87	22.04
$R_{\text{min}}(0°)$/Å	3.84	3.84	3.79	3.76	3.78
$R_{\text{min}}(180°)$/Å	3.21	3.21	3.51	3.52	3.44
$R_{\text{min}}(0°)$-$R_{\text{min}}(180°)$/Å	0.63	0.63	0.28	0.24	0.34
Parameter	$V_{ab\ initio}$	V_{morphed}	*ab initio*[b]	*ab initio*[c]	
$V_{\text{min}}(0°)$/cm^{-1}	-58.58	-90.2(37)	-58.99	-66.85	
$V_{\text{min}}(180°)$/cm^{-1}	-48.49	-74.8(30)	-61.55	-65.10	
$V_{\text{min}}(0°)$-$V_{\text{min}}(180°)$/cm^{-1}	-10.09	-15.4(48)	2.56	-1.75	
Barrier height/cm^{-1}	30.38	46.7(41)	21.11	21.85	
$R_{\text{min}}(0°)$/Å	3.91	3.45(1)	3.87	3.83	
$R_{\text{min}}(180°)$/Å	3.45	3.13(1)	3.41	3.40	
$R_{\text{min}}(0°)$-$R_{\text{min}}(180°)$/Å	0.46	0.32(2)	0.46	0.43	

[a]From [71].
[b]From [75] CCSD(T)/aug-cc-pVTZ-332 level of theory.
[c]From [76] CCSD(T)/aug-cc-pV5Z-33211 level of theory.

In Table 2, the final morphing parameters that yielded the best fit of the experimental data are given. The correlation matrix for the final morphing parameters is given in Table 3. The morphed potential is characterized by two linear minima (see Figures 3 and 4), with the Ne-H-Cl minimum having R = 3.45(1) Å corresponding to V_{min} = -90.2(37) cm^{-1}, and the Ne-Cl-H minimum having R = 3.13(1) Å and V_{min} = -74.8(30) cm^{-1}.

In Table 4, the generated three-dimensional morphed potential has been compared with other available potentials for Ne:HCl. The three-dimensional morphed potential is found to give significantly deeper minima than the corresponding parameters in other determined potentials. Furthermore, the values of $R(0°)$ and $R(180°)$ are significantly smaller for the three-dimensional morphed potential. However, the dissociation energy, D_0, is determined to be within the same range of previous calculated values [27,69,71,72,75,76]. In addition, the absolute value of the energy difference between the two minima, in the three-dimensional morphed potential of 15.4(48) cm^{-1}, compares with the 14.72 cm^{-1} obtained from the M5 potential [71]; but is significantly larger than the value determined from the H6$\left(\nu_1 = 1\right)$ potential (Table 4). Lastly, the barrier height for the internal rotation of HCl subunit was determined to be 46.7(41) cm^{-1}, which is considerably larger than the previously determined values [71,75,76] (Table 4).

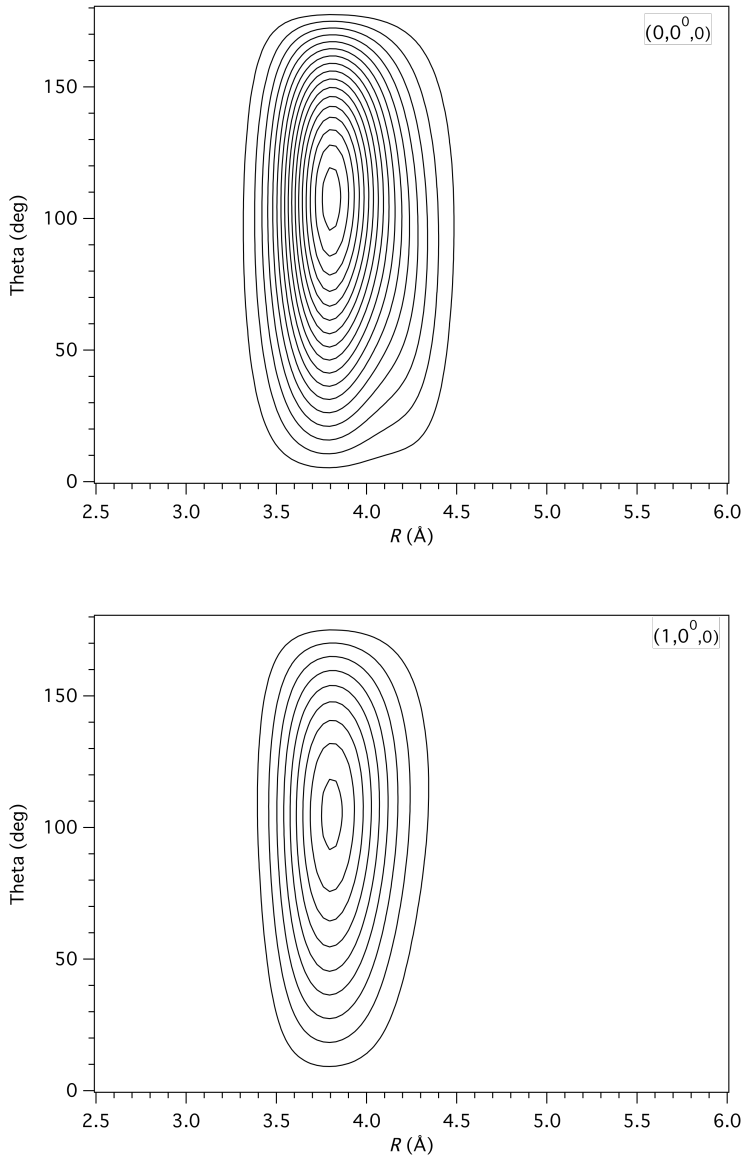

Figure 5. Ground state probability densities for the ^{20}Ne-H^{35}Cl isotopomer. In the top of the figure the probability density for H-^{35}Cl in the $v_1 = 0$ state is shown, and in the bottom of the figure the probability density for the H-^{35}Cl $v_1 = 1$ state is shown.

Table 5
Predicted spectroscopic constants from the morphed potential for Ne-HCl.

Isotopomer	State	B ($\times 10^{-2}$ cm^{-1})	D_J ($\times 10^{-7}$ cm^{-1})	$\langle P_1(\cos\theta)\rangle$	$\langle P_2(\cos\theta)\rangle$
^{20}Ne-H^{35}Cl	$(0,2^0,0)$	9.326	95.17	-0.1592	0.3424
^{20}Ne-H^{35}Cl	$(0,0^0,1)$	7.364	-78.71	-0.0294	0.0929
^{20}Ne-H^{35}Cl	$(0,1^{1f},0)$	9.116	75.25	0.0337	-0.1832
^{20}Ne-D^{35}Cl	$(0,0^0,1)$	7.951	181.14	-0.1725	0.0698
^{20}Ne-D^{35}Cl	$(0,1^{1f},0)$	9.051	73.44	0.0593	-0.1658
^{20}Ne-D^{35}Cl	$(1,0^0,1)$	7.923	184.67	-0.1775	0.0710

Additional experimental data for Ne:H(D)Cl, with H(D)Cl in its $v_1 = 0$ state, especially D_0, will be necessary in order to determine an accurate potential well depth, D_e. The fact that the D_0 does not change with a deeper morphed potential can be attributed to the fact that the morphed potential has a bigger barrier for the internal rotation of HCl subunit. Since the wave functions (see Figure 5) for the states considered here are delocalized, corresponding to nearly free rotor states, the net shift of the rovibrational energy levels, upon morphing, results from the near cancellation of the positive shift in the energies, due to the increase in the barrier height, and a negative shift in the energies, due to deeper minima.

The morphed potentials in the $v_1 = 0$ and $v_1 = 1$ states of HCl, in Table 4, provide a more relevant comparison with the M4, M5, and H6$\left(v_1 = 1\right)$ potentials respectively. The well depth for the morphed potentials in the $v_1 = 0$ and $v_1 = 1$ states are deeper in the Ne-HCl configuration, but substantially the same in the Ne-ClH configuration. This is noted when compared to the M4, M5, and H6$\left(v_1 = 1\right)$ potentials. In addition, the barrier height is larger for the morphed potentials in the $v_1 = 0$ and $v_1 = 1$ states when again compared to the M4, M5, and H6$\left(v_1 = 1\right)$ potentials. Furthermore, the values of $R(0°)$ and $R(180°)$ for the morphed potentials, in the $v_1 = 0$ and $v_1 = 1$ states, are significantly different from the values determined for the M4, M5, and H6$\left(v_1 = 1\right)$ potentials. Lastly, in Table 5, predictions from the morphed potential have been given to some yet to be observed transitions in ^{20}Ne-H^{35}Cl and ^{20}Ne-D^{35}Cl.

Experimental observation of such transition will provide a valuable criterion for determining the preferred model for the complex.

The morphed potential for the Ne:HCl complex is a double minimum potential with $V_{min}(0°)$ = -90.2(37) cm^{-1}, $R(0°)$ = 3.45(1) Å, and $V_{min}(180°)$ = -74.8(30) cm^{-1}, $R(180°)$ = 3.13(1) Å with a barrier of 46.7(41) cm^{-1}. From the present analysis, it can be concluded that the global and local minima in Ne-HCl, have significantly deeper minima, a larger barrier, and smaller $R_{min}(0°)$ and $R_{min}(180°)$, than what was determined in previous potentials. Comparable trends have been determined from the extensive morphing studies of the Ar:HBr complex [23,26]. This is in contrast to the corresponding morphed potentials determined for Ne:HBr [21], particularly Ne:HI [20] which gave convincing evidence for the existence of Ne-XH (X = Br, I) global minima. This occurred in cases where multipole-induced multipole interactions are expected to be smaller, and dispersion effects larger, thus favoring van der Waals global minima.

4.2 OC:HCl

In the previous section, the three-dimensional morphed potential was generated for the Ne:HCl complex. In this section, the potential morphing methodology is applied to OC:HCl, which is a system of higher dimension than considered previously. The OC:HCl system is treated as two interacting linear rotors, thus the vibrational problem is reduced to a four-dimensional problem.

The linear OC:HX (X = F, Cl, Br, I) dimers have five modes of intermolecular vibrational motion: one stretch of the intermolecular hydrogen bond ν_3, a doubly degenerate high-frequency bending vibration ν_4^1 (libration of HX), and a doubly degenerate low-frequency bending vibration ν_5^1 (libration of CO). In addition, the dimer has the intramolecular H-X and C-O stretching vibrations, ν_1 and ν_2 respectively.

Experiment and theory concur that the hydrogen-bonded complex OC-HCl has a linear equilibrium geometry [81-92]. *Ab initio* calculations [84,86,89,90] also suggest that the CO-HCl isomer has linear equilibrium geometry, although experimentally it has not yet been observed in the gas phase. Initial experimental work using pulse-nozzle Fourier transform microwave spectroscopy [91,93] provided a precise ground state molecular structure for the OC-HCl isomer. A Rabi-type molecular beam electric resonance spectrometer gave additional microwave and radio-frequency data [81]. The values of the ν_1, ν_2, and ν_4^1 vibrational frequencies were initially determined to be 2815.2(3) cm^{-1}, 2154.3(3) cm^{-1}, and 247.1(5) cm^{-1} by using infrared spectra in solid argon matrices [94]. In the gas phase, the analysis of the intramolecular bands ν_1 and ν_2, located at 2851.761(2) cm^{-1} and 2155.500(2) cm^{-1}, were reported using diode-laser [92] and Fourier transform supersonic-jet spectroscopy [88]. Subsequently, the static gas-phase Fourier transform IR spectrum was recorded [87] and used to evaluate [83] the ν_5^1 bending band, which was found to be at 48.9944(2) cm^{-1}. Recently, a gas phase study of the OC-HCl dimer, using synchrotron radiation, was reported [85] and the ν_4^1

intermolecular vibrational frequency of OC-HCl was determined to be 201.20464(27) cm^{-1}.

In the *ab initio* calculation, the bond lengths of the monomer components were fixed at the experimental r_e: 1.128323 Å for CO [79] and 1.274552 Å for HCl [79]. The five *ab initio* potentials calculated for the OC:HCl complex were: (i) CCSD(T)/aug-cc-pVTZ, (ii) MP2/aug-cc-pVQZ, (iii) MP2/aug-cc-pVTZ, (iv) HF/aug-cc-pV5Z, and (v) HF/aug-cc-pVQZ. These five potentials were corrected for the BSSE. The CCSD(T)/aug-cc-pVTZ potential without the CP correction was also calculated. All six of these *ab initio* potentials were calculated in a four-dimensional grid of 1,813 $\left(R,\theta_1,\theta_2,\phi\right)$ points, defined in Figure 1(b). R, which is the distance between the center of mass of CO and HCl, takes the values of 3.00 Å, 4.00 Å, 4.25 Å, 4.50 Å, 4.75 Å, 5.50 Å, and 8.00 Å. The angles θ_1 and θ_2 take the values of 18.0º, 54.0º, 90.0º, 126.0º, and 162.0º. Lastly, the dihedral angle ϕ takes the values of 18.0º, 54.0º, 90.0º, 126.0º, 162.0º, 198.0º, 234.0º, 270.0º, 306.0º, and 342.0º. The four-dimensional grid was supplemented with additional points at all values of R, and with ϕ = 0.0º, θ_1 = 2.0º, 8.0º, and 14.0º, and θ_2 = 166.0º, 172.0º, and 178.0º. In the fitting of the *ab initio* potential the weighing factor, in Eq. (21), F_w = 25 cm^{-1} was used. This was selected in order to obtain an absolute average difference less than 6.0 cm^{-1} between the *ab initio* and fitted potential for the points within 270 cm^{-1} from the minimum of the potential [45,49]. The value of the V_{min} in Eq. (22) was chosen to be 1000 cm^{-1}. The values of the parameters used in the rovibrational calculations were: R_{start} = 3.50 Å, R_{end} = 8.00 Å, N_R = 38, N_{θ_1} = 48,

$N_{\theta_2} = 24$, $N_\phi = 40$, $N_F = 34$, $j_{max_1} = 20$, $j_{max_2} = 16$, and $\tau_L = 10^{-12}$ atomic units. In addition, the rotational constants for the diatomic fragments selected were [91]: 1.92252905 cm^{-1} for $^{12}C^{16}O$, 1.83792976 cm^{-1} for $^{13}C^{16}O$, 10.4401992 cm^{-1} for $H^{35}Cl$, 10.42451578 cm^{-1} for $H^{37}Cl$, and 5.392271676 cm^{-1} for $D^{35}Cl$.

The CMM method in Eq. (61) was used to morph the interaction potential of OC:HCl. The PCM method described in Eqs. (9) to (12) was also applied to the OC:HCl system, where the R_f value was selected to be 4.30 Å. For the CMM method the parameters C_4 and C_7 were constrained to zero, and C_6 to one, i.e. no relativistic and radial corrections for the CMM potential of OC:HCl. The experimental data used to morph the intermolecular PES of OC:HCl is shown in Table 6. This data includes ground vibrational state microwave spectra [91] as well as supersonic jet infrared spectra [83]. The values of G shown in Table 6 for the $V_{CMM}^{(0)}$ and CCSD(T)/aug-cc-pVTZ potentials are $G = 22.3$ and $G = 37.1$, respectively. When using the same data and σ_k, for the morphed potentials, the values of G are $G = 2.9$ (for the CMM method) and $G = 9.3$ (for the PCM method). Thus there is an indication of improvement in the overall agreement with experimental data obtained from the application of the morphing procedure.

Table 6
Experimental data of OC:HCl used in the fits and fitted values, and their uncertainties.

Observable[a]	Isotopomer	$V_{\mathrm{CMM}}^{(0)}$	$V_{\mathrm{CMM}}^{(2)}$	$\left(V_{\mathrm{CCSD(T)}}\right)_{\mathrm{TZ}}^{\mathrm{CP}}$	V_{PCM}[b]	Exp	σ_k
B (GS)/10^{-2} cm^{-1}	^{16}O^{12}C-H^{35}Cl	5.525	5.583	5.481	5.580	5.576[c]	0.002
D_J (GS)/10^{-8} cm^{-1}	^{16}O^{12}C-H^{35}Cl	15.7	15.8	16.1	16.2	16.0[c]	0.2
B (GS)/10^{-2} cm^{-1}	^{16}O^{12}C-D^{35}Cl	5.538	5.597	5.495	5.595	5.590[c]	0.002
D_J (GS)/10^{-8} cm^{-1}	^{16}O^{12}C-D^{35}Cl	14.6	14.8	15.0	15.1	15.0[c]	0.2
B (ν_5^1)/10^{-2} cm^{-1}	^{16}O^{12}C-H^{35}Cl	5.597	5.655	5.550	5.649	5.657[d]	0.002
D_J (ν_5^1)/10^{-8} cm^{-1}	^{16}O^{12}C-H^{35}Cl	18.4	18.7	18.7	18.8	19.1[d]	0.5
$\langle P_2(\cos\theta_2)\rangle$ (GS)	^{16}O^{12}C-H^{35}Cl	0.807	0.780	0.806	0.808	0.770[c]	0.002
$\langle P_2(\cos\theta_2)\rangle$ (GS)	^{16}O^{12}C-D^{35}Cl	0.859	0.829	0.858	0.860	0.820[c]	0.002
ν_5^1/cm^{-1}	^{16}O^{12}C-H^{35}Cl	48.60	48.98	48.34	48.99	48.99[d]	0.01
G		22.3	2.9	37.1	9.3		

[a]GS = ground state.
[b]The *ab initio* potential used in the PCM procedure was the CCSD(T)/aug-cc-pVTZ, with the CP correction, which is the same potential used in the CMM procedure.
[c]From [91].
[d]From [83].

Table 7
Optimized values for the morphing parameters of OC:HCl.

PCM method									
α	i	$\lambda_{\alpha,i} = (l_x$	n	θ'_1	θ'_2	$\phi')$	$C^{(0)}_{\alpha,i}$	$C_{\alpha,i}$	σ
1	1	0					1.0	1.0210	0.0004
2	1	0					1.0	1.0125	0.0047
3	1	0					0.0	0.0092	0.0001
CMM method									
α							$C^{(0)}_{\alpha}$	$C^{(2)}_{\alpha}$	σ
1							1.0	0.9602	0.0009
2							0.0	(0.0)	Constrained
3							1.0	0.5408	0.0078
4							0.0	(0.0)	Constrained
5							1.0	(1.0)	Constrained
6							1.0	(1.0)	Constrained
7							0.0	(0.0)	Constrained

In Table 7, final morphing parameters are given that yield the best fit compared to the experimental data. The magnitude of the values of these parameters gives the contribution needed in order to improve the $V_{\mathrm{CMM}}^{(0)}$ and CCSD(T)/aug-cc-pVTZ potentials and obtain the best agreement with the experimental data. The value of the C_5 parameter in the CMM potential shown in Table 7 was constrained to one because its value could not be determined with statistical significance and it did not change the quality of the final fit. Similarly, the value of the C_2 parameter in the CMM potential could not be determined with statistical significance, and was consequently constrained to zero. In addition, as expected the C_3 parameter is close to 0.5. Since the MP2 potential overestimates the correlation energy and the CCSD(T) potential under estimates the correlation energy, it is reasonable that this value of the C_3 parameter be close to 0.5. In contrast to the PCM method [28-30], the CMM approach does not involve angular morphing functions (Eq. (11)). In Table 7, the morphing parameters of the PCM and CMM methods are compared. The parameter C_1 in the CMM approach is similar to the parameter $C_{1,1}$ in the PCM method, which is the scaling of the reference potential.

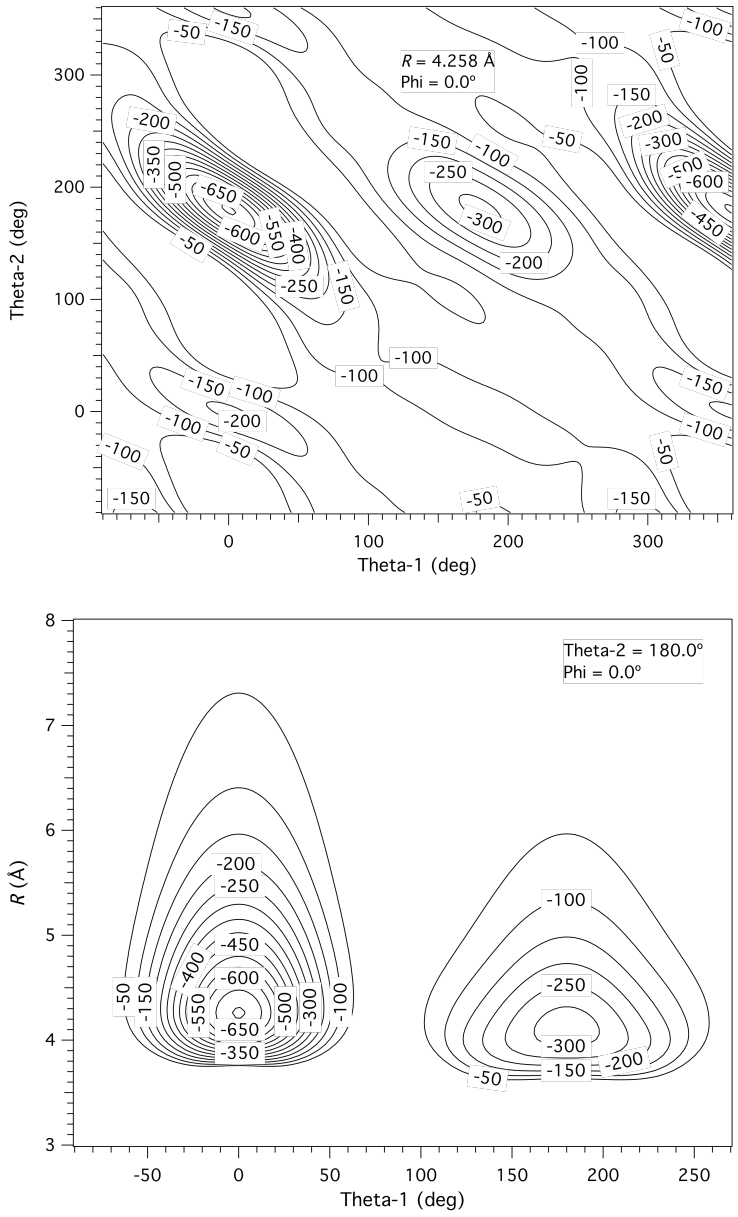

Figure 6. Two-dimensional slices of the interaction potential of $^{16}O^{12}C{:}H^{35}Cl$ generated using the CMM method. The coordinates used are the Jacobi coordinates defined in Figure 1(b). All contours are in cm^{-1}.

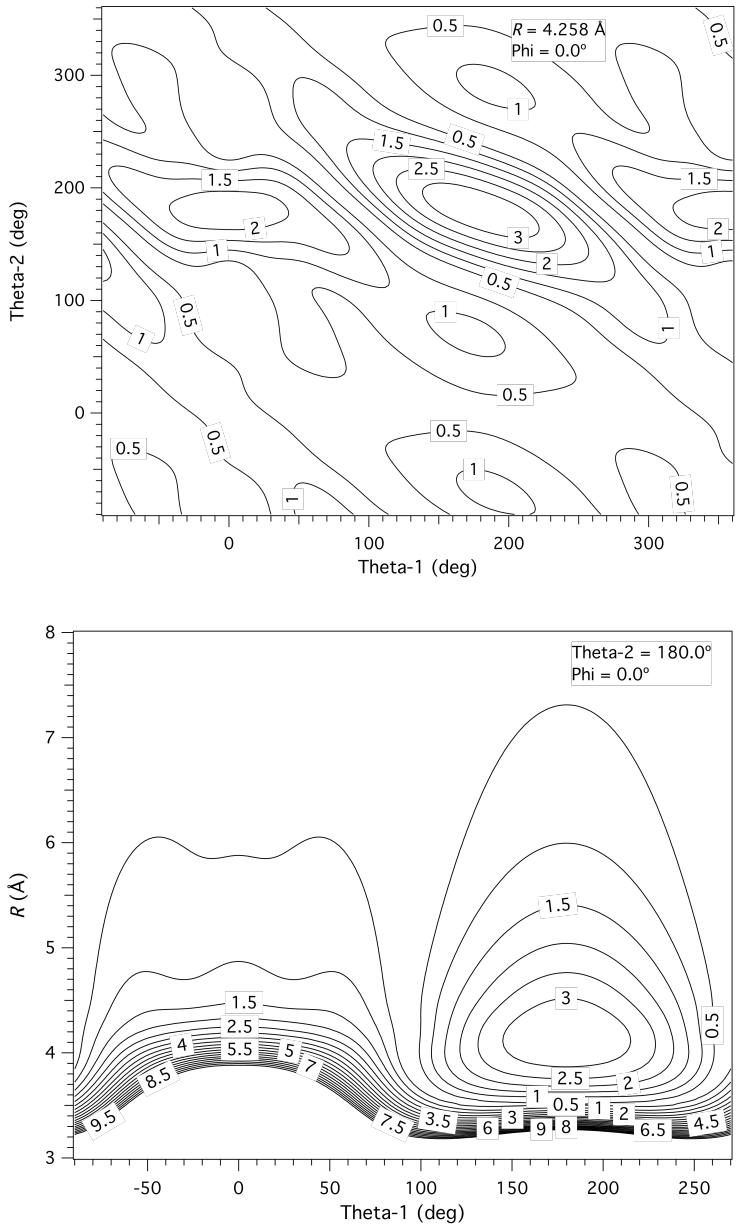

Figure 7. The corresponding estimated errors on the $^{16}O^{12}C{:}H^{35}Cl$ CMM potential, relative to the potential at infinite separation. The coordinates used are the Jacobi coordinates defined in Figure 1(b). All contours are in cm^{-1}.

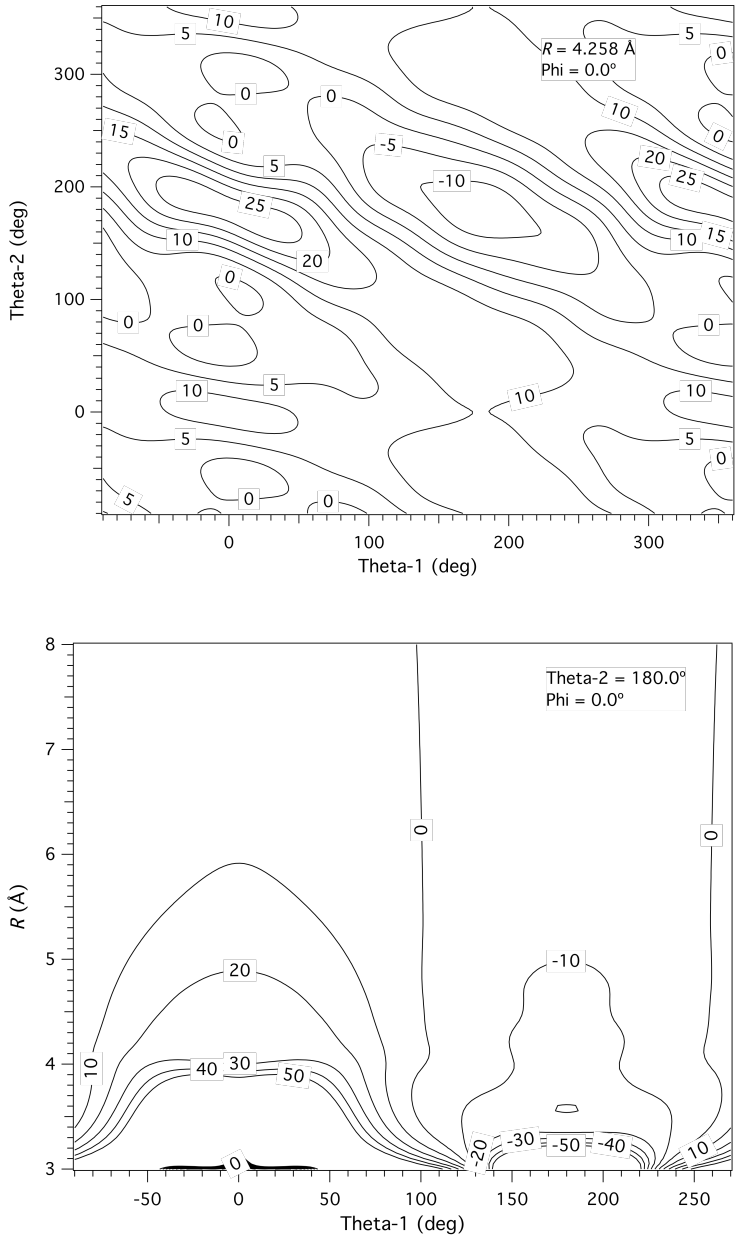

Figure 8. Differences between interaction potentials of $^{16}O^{12}C$:$H^{35}Cl$ generated by the PCM and CMM methods. The coordinates used are the Jacobi coordinates defined in Figure 1(b). All contours are in cm^{-1}.

Table 8
Features of morphed potentials of OC:HCl.

Isomer	Parameter	PCM method	$V_{CMM}^{(2)}$ CMM method
OC-HCl	D_e/cm^{-1}	677(4)	705(3)
	R/Å	4.255(2)	4.258(8)
CO-HCl	D_e/cm^{-1}	341(2)	325(4)
	R/Å	4.11(2)	4.11(4)

Table 9
Comparison of predicted vibrational frequencies and D_0 energy of $^{16}O^{12}C$-$H^{35}Cl$.

Observable	PCM method	$V_{CMM}^{(2)}$ CMM method	Exp
D_0/cm^{-1}	365(3)	387(2)	-
ν_3/cm^{-1}	62(4)	63.3(1)	-
$B(\nu_3)/10^{-2}$ cm^{-1}	5.43(2)	5.454(8)	-
$D_J(\nu_3)/10^{-8}$ cm^{-1}	24(1)	25.5(2)	-
ν_4^1/cm^{-1}	194.0(7)	199.1(6)	201.20464(27)[a]
$B(\nu_4^1)/10^{-2}$ cm^{-1}	5.44(2)	5.442(6)	5.42994(13)[a]
$D_J(\nu_4^1)/10^{-8}$ cm^{-1}	23(3)	21.90(8)	21.42(15)[a]

[a]From [85].

Table 10
Comparison of previous potentials of OC:HCl.

Reference	D_e (cm^{-1}) $^{16}O^{12}C$-$H^{35}Cl$	D_e (cm^{-1}) $^{12}C^{6}O$-$H^{35}Cl$
[84][a]	340	323
[89][a]	899	745
[90][a]	740	480
[86][a]	750.16	485.88
[91][b]	443	-
[91][c]	569	-
[85][a]	654	-
PCM[c]	677(4)	341(2)
CMM[c]	705(3)	325(4)

[a]*Ab initio* calculations.
[b]MMC calculations.
[c]Empirical model.

In Figure 6, two-dimensional slices of the CMM interaction potential of $^{16}O^{12}C$:$H^{35}Cl$ are shown. The corresponding estimated errors relative to the potential at infinite separation are given in Figure 7. The CMM potential has a global minimum with a well depth of 705(3) cm^{-1}, that corresponds to the linear structure $^{16}O^{12}C$-$H^{35}Cl$ with a R = 4.258(8) Å. The linear isomer $^{12}C^{16}O$-$H^{35}Cl$ has a corresponding well depth of 325(4) cm^{-1} with R = 4.11(4) Å. This results in a ΔE of 380(5) cm^{-1} between the minima in the potential energy of two isomers. Furthermore, the PCM and CMM methods give very similar surfaces (see Figure 8 and Table 8). However, the principal difference between these two surfaces lies in the relative well depth of the OC-HCl and CO-HCl isomers. The value of D_e of 705(3) cm^{-1} from the CMM potential compares to the 696 cm^{-1} from the complete basis set limit predicted by Larsen and coworker [85].

To test the accuracy of both surfaces, the ν_4^1 frequency of $^{16}O^{12}C$-$H^{35}Cl$ was predicted as is shown in Table 9, and compared with the experimental value. It is found that the CMM surface gives more accurate predictions than did the PCM surface. The binding energies, D_e and D_0, for the isomers $^{16}O^{12}C$-$H^{35}Cl$ and $^{12}C^{16}O$-$H^{35}Cl$ have been predicted in different theoretical and empirical studies [82,84-86,89-91]. Moreover, a comparison for the predicted values of D_e and D_0, with previous theoretical and empirical calculations, is given in Table 10. It is found that the predictions from the morphed potential are at an intermediate range within the calculated values.

One advantage of the CMM method is that the fitting procedure involves fewer arbitrary choices. However, larger basis set potentials are needed in order to implement the CMM method. There can thus be a disadvantage in using the CMM method in

systems with large vibrational dimensionality, and in systems that contain heavy elements and thus more electrons such as iodine. In contrast, the PCM method offers the advantage of being able to add localized angular morphing functions to better fit the experimental observables. However, the location on the potential where these localized angular morphing functions are placed is arbitrary. In addition, as the number of localized angular morphing functions increases, the morphing parameters associated with these functions may become linearly dependent. Consequently, the inversion process (i.e., obtaining a potential from a set of experimental observables) can become ill conditioned [23]. The CMM method has been compared with the PCM method and is found to generate very similar surfaces in the specific case of the OC:HCl system. With only two morphing parameters, the CMM method gives a more accurate surface than the PCM method, which uses three morphing parameters, for OC:HCl.

4.3 OC:HBr

In the previous section, the CMM method was applied to the OC:HCl complex, and it was found to be more accurate than the PCM method. In this section, the CMM method is applied to the OC:HBr system to investigate the transferability of the morphing parameters.

The OC:HBr complex was first observed using pulsed microwave Fourier transform spectroscopy [95,96]. These results were found to be consistent with the linear equilibrium ground state structure OC-HBr. For the $^{16}O^{12}C$-$H^{79}Br$ isotopomer, the

ground state structural parameters were determined to be: R = 4.5469 Å, θ_2 = 23.16°, and $\theta_1 = \phi = 0.0°$ [96]. The values of the fundamental frequencies of ν_1, ν_2, and ν_4^1, for $^{16}O^{12}C$-$H^{79}Br$, were reported to be 2520.1(3) cm^{-1}, 2152.4(3) cm^{-1}, and 158.3(5) cm^{-1} using matrix infrared spectroscopy [94]. Subsequently, the ν_1 and ν_2 vibrations, in isolated $^{16}O^{12}C$-$H^{79}Br$, were determined, with greater accuracy to be 2542.45245(13) cm^{-1} and 2152.605023(60) cm^{-1} respectively [97-99]. Lastly, the low frequency intermolecular bending vibration ν_5^1, in $^{16}O^{12}C$-$H^{79}Br$, was determined to be 39.65242(42) cm^{-1} using frequency differences observed by near infrared diode-laser cw slit jet spectroscopy [99]. It is important to point out that in $^{16}O^{12}C$-$H^{79}Br$, the intermolecular hydrogen bond stretching (ν_3), and the high frequency intermolecular bending vibration (ν_4^1), have yet to be observed experimentally in the gas phase.

The *ab initio* potentials calculated in this work are: (i) CCSD(T)/aug-cc-pVTZ, (ii) MP2/aug-cc-pVQZ, (iii) MP2/aug-cc-pVTZ, (iv) HF/aug-cc-pV5Z, and (v) HF/aug-cc-pVQZ. These five potentials were corrected for BSSE. In addition, the CCSD(T)/aug-cc-pVTZ potential, without the CP correction, was calculated. All six of these *ab initio* potentials were calculated on a four-dimensional grid $\left(R,\theta_1,\theta_2,\phi\right)$ of 2032 points, defined in Figure 1(b). The variable R, which is the distance between the center of masses of CO and HBr, takes the values of 2.75 Å, 3.75 Å, 4.25 Å, 4.50 Å, 4.75 Å, 5.25 Å, 6.25 Å, and 8.25 Å. The angles θ_1 and θ_2 take the values of 10.0º, 50.0º, 90.0º, 130.0º, and 170.0º. Lastly, the dihedral angle ϕ takes the values of 10.0º, 50.0º, 90.0º,

130.0º, 170.0º, 190.0º, 230.0º, 270.0º, 310.0º, and 350.0º. The four-dimensional grid was supplemented with additional points at all values of R, and with $\phi = 0.0º$, and $\theta_1 = \theta_2 = 0.0º$ and 180.0º. In all calculations, the bond lengths of both monomer components were fixed at r_e of 1.128323 Å for CO and 1.41443 Å for HBr [79]. In the fitting of the *ab initio* potential, the weighing factor, in Eq. (21), F_w = 50 cm^{-1} was used. This was undertaken in order to obtain an absolute average difference less than 6.0 cm^{-1}, between the *ab initio* and fitted potential, for the points within 200 cm^{-1} from the minimum of the potential [45,49]. The value of the V_{min} in Eq. (22) was chosen to be 800 cm^{-1}. The value of the parameters used in the rovibrational calculations were: R_{start} = 2.80 Å, R_{end} = 8.25 Å, $N_R = 46$, $N_{\theta_1} = 24$, $N_{\theta_2} = 24$, $N_\phi = 36$, $N_F = 42$, $j_{max_1} = 16$, $j_{max_2} = 16$, and τ_L = 10^{-12} atomic units. In addition, the rotational constants for the diatomic fragments used were [96]: 1.92252905 cm^{-1} for $^{12}C^{16}O$, 8.35106099 cm^{-1} for $H^{79}Br$, and 4.24819356 cm^{-1} for $D^{79}Br$.

The CMM method in Eq. (61) was used to morph the interaction potential of OC:HBr. The parameters C_4 and C_7 were constrained to zero and C_6 to one, i.e. no relativistic and radial corrections for the CMM potential of OC:HBr. The experimental data used to morph the intermolecular potential energy surface of OC:HBr is shown in Table 11. This data includes ground vibrational state microwave spectra, as well as supersonic jet infrared spectra [96,99].

Table 11
Experimental data of OC:HBr used in the fits and fitted values, and their uncertainties.

Observable[a]	Isotopomer	$V_{CMM}^{(0)}$	$V_{CMM}^{(3)}$	Exp	σ_k
B (GS)/10^{-2} cm^{-1}	^{16}O^{12}C-H^{79}Br	3.810	3.841	3.838[b]	0.002
D_J (GS)/10^{-8} cm^{-1}	^{16}O^{12}C-H^{79}Br	8.83	9.05	9.02[b]	0.02
B (GS)/10^{-2} cm^{-1}	^{16}O^{12}C-D^{79}Br	3.816	3.849	3.849[b]	0.002
D_J (GS)/10^{-8} cm^{-1}	^{16}O^{12}C-D^{79}Br	8.27	8.48	8.39[b]	0.02
B (ν_5^1)/10^{-2} cm^{-1}	^{16}O^{12}C-H^{79}Br	3.871	3.902	3.911[c]	0.002
D_J (ν_5^1)/10^{-8} cm^{-1}	^{16}O^{12}C-H^{79}Br	10.5	10.8	12.0[c]	0.5
$\langle P_2(\cos\theta_2)\rangle$ (GS)	^{16}O^{12}C-H^{79}Br	0.793	0.774	0.770[b]	0.002
$\langle P_2(\cos\theta_2)\rangle$ (GS)	^{16}O^{12}C-D^{79}Br	0.845	0.824	0.824[b]	0.002
ν_5^1/cm^{-1}	^{16}O^{12}C-H^{79}Br	39.99	39.66	39.65[c]	0.01
G		16.2	2.5		

[a]GS = ground state.
[b]From [96].
[c]From [99].

Table 12
Optimized values for the morphing parameters of OC:HBr.

α	$C_\alpha^{(0)}$	$C_\alpha^{(3)}$	σ
1	1.0	0.9703	0.0014
2	0.0	0.1645	0.0109
3	1.0	0.4849	0.0200
4	(0.0)	(0.0)	Constrained
5	(1.0)	(1.0)	Constrained
6	(1.0)	(1.0)	Constrained
7	(0.0)	(0.0)	Constrained

Table 13

Predictions of ν_3 and ν_4^1 frequencies, for ^{16}O^{12}C-H^{79}Br, using the $V_{CMM}^{(3)}$ potential.

B (ν_3) ($\times10^{-2}$ cm^{-1})	B (ν_4^1) ($\times10^{-2}$ cm^{-1})	D_J (ν_3) ($\times10^{-8}$ cm^{-1})	D_J (ν_4^1) ($\times10^{-8}$ cm^{-1})	ν_3 (cm^{-1})	ν_4^1 (cm^{-1})
3.770(7)	3.767(5)	14.03(9)	12.1(1)	48.2(1)	157(1)

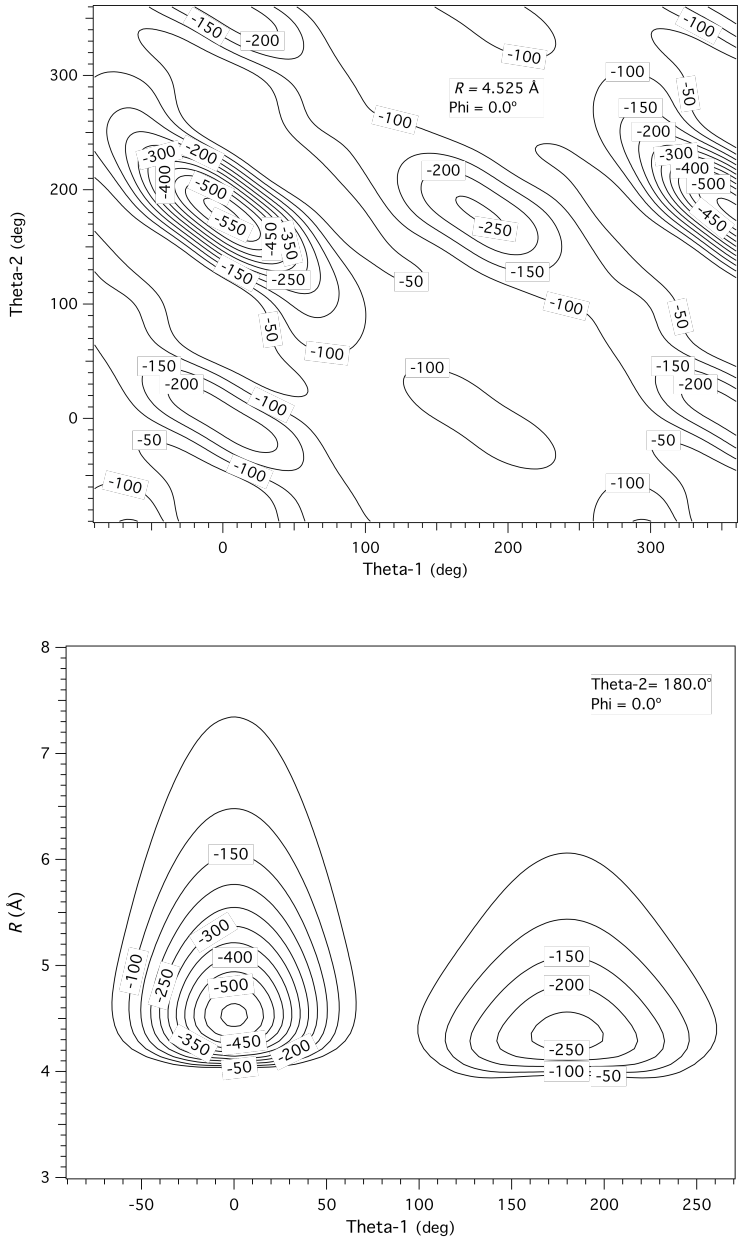

Figure 9. Two-dimensional slices of the $V_{\mathrm{CMM}}^{(3)}$ interaction potential of $^{16}O^{12}C{:}H^{79}Br$. The coordinates used are the Jacobi coordinates defined in Figure 1(b). All contours are in cm^{-1}.

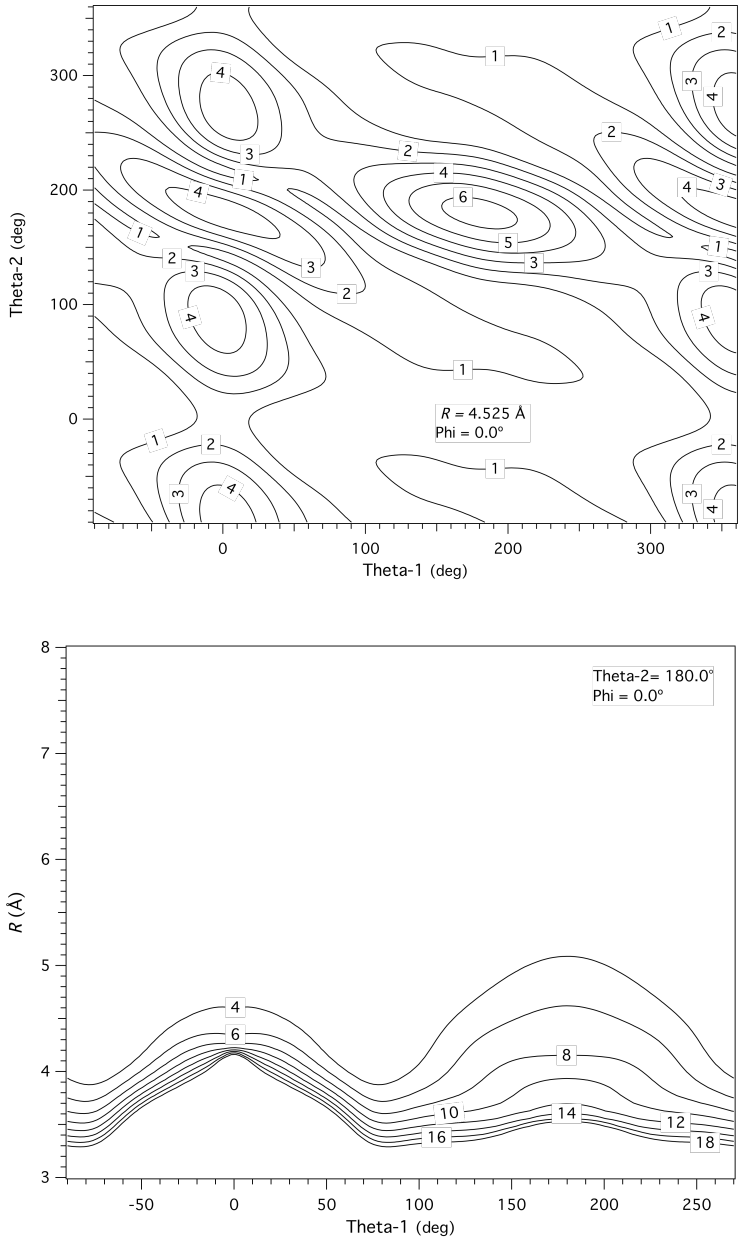

Figure 10. The corresponding estimated errors on the $^{16}O^{12}C$:$H^{79}Br$ CMM potential, relative to the potential at infinite separation. The coordinates used are the Jacobi coordinates defined in Figure 1(b). All contours are in cm^{-1}.

The values of G for the $V_{CMM}^{(0)}$ and morphed potential ($V_{CMM}^{(3)}$), given by Table 11, are G = 16.2 and G = 2.5, respectively. This indicates the improvement in the overall agreement with experimental data obtained through the morphing procedure. In Table 12, final morphing parameters are given that yield the best fit of the experimental data. The value of the C_5 parameter was constrained to one, because its value could not be determined with statistical significance and it did not change the quality of the final fit.

In Figure 9, two-dimensional slices of the $V_{CMM}^{(3)}$ interaction potential of $^{16}O^{12}C$:$H^{79}Br$ are shown. The corresponding estimated errors relative to the potential, at infinite separation, are given in Figure 10. The potential has a global minimum with well depth of 564(5) cm^{-1}, corresponding to the equilibrium linear structure $^{16}O^{12}C$-$H^{79}Br$, with R = 4.525(7) Å. The linear isomers $^{12}C^{16}O$-$H^{79}Br$ and $^{16}O^{12}C$-^{79}BrH have corresponding local well depths of 273(7) cm^{-1} and 269(2) cm^{-1}, with R = 4.35(4) Å and 4.24(3) Å respectively. This results in a ΔE of 293(9) cm^{-1}, between the minima, of the potential energy of three isomers.

In Table 13, predictions of the ν_3 and ν_4^1 frequencies for $^{16}O^{12}C$-$H^{79}Br$, using the $V_{CMM}^{(3)}$ potential are given. The prediction of 157(1) cm^{-1} for ν_4^1 can be compared with 158.3(5) cm^{-1}, obtained using matrix infrared spectroscopy. This is expected to be frequency shifted, relative to the gas phase value, due to the matrix environment [94]. In addition, the ν_3 vibrational frequency in $^{16}O^{12}C$-$H^{79}Br$ is predicted to be 48.2(1) cm^{-1}.

An *ab initio* potential for the OC:HBr interaction has been morphed, using spectroscopic data, to give a compound model morphed potential. The fact that the

$^{12}C^{16}O$-$H^{79}Br$ and $^{16}O^{12}C$-^{79}BrH isomers have about the same local well depths, within the estimated errors, indicates the importance of the dispersion contributions to the interaction potential. It is found that the counterpoise method under corrected the BSSE in OC:HBr by 16(7)%, as seen by the positive value of the $C_2^{(3)}$ parameter in Table 12, and the definition of the morphing parameters in Eq. (61).

4.4 OC:HI

In the previous section, it was found that dispersion interactions make a significant contribution to the interaction potential of OC:HBr. This implies that in OC:HBr, the van der Waals interactions make larger contributions to the interaction potential than in the OC:HCl complex. It is also expected that in the OC:HI complex the van der Waals interactions would dominate over the hydrogen bond interactions. In this section, the potential morphing methodology is applied to the OC:HI complex to gain insight concerning intermolecular forces acting in this family of complexes.

The OC:HI complex has been characterized by microwave [100], and near infrared diode-laser spectroscopy [101,102], giving a linear OC-HI ground state structure. In addition, the values of the ν_1, ν_2, and ν_5^1 vibrational frequencies were determined to be 2228.31996(11) cm^{-1}, 2148.54904(3) cm^{-1}, and 25.89167(41) cm^{-1} respectively [101]. The isomer OC-IH was also identified by near infrared diode-laser spectroscopy, providing the values for the ν_1, ν_2, and ν_5^1 vibrational frequencies which

were 2222.6684(1) cm^{-1}, 2146.68233(16) cm^{-1}, and 28.31000(25) cm^{-1} respectively [101,102]. Finally, *ab initio* calculations suggested the existence of the isomers CO-HI and CO-IH [102].

In the *ab initio* calculation, the bond lengths of the monomer components were fixed at the experimental r_e: 1.128323 Å for CO [79] and 1.60916 Å for HI [79]. The interaction energy of the OC:HI dimer was calculated at the CCSD(T) level of theory. The aug-cc-pVTZ basis set was used for all of the atoms except for iodine, for which the basis set was the pseudopotential aug-cc-pVTZ-pp [103]. The potential energy surface was calculated on a grid built, taking 14 different R points (3.00 Å, 3.30 Å, 3.60 Å, 3.90 Å, 4.20 Å, 4.50 Å, 4.70 Å, 4.90 Å, 5.20 Å, 5.50 Å, 6.00 Å, 6.50 Å, 7.00 Å, and 8.00 Å), 5 points for both θ_1 and θ_2 (30.0°, 60.0°, 90.0°, 120.0°, and 150.0°), and 10 points for ϕ (30.0°, 60.0°, 90.0°, 120.0°, 150.0°, 210.0°, 240.0°, 270.0°, 300.0°, and 330.0°). This set of points was supplemented with additional points at all values of R and with $\theta_1 = \theta_2 = \phi = 0.0°$ and 180.0°; $\theta_1 = \theta_2 = 2.0°$ and 178.0°, and $\phi = 0.0°$ and 180.0°; $\theta_1 = \theta_2 = 5.0°$ and 175.0°, and $\phi = 0.0°$ and 180.0°; giving a final grid composed of 3,836 points, defined in Figure 1(b). In the fitting of the *ab initio* potential, the weighing factor, in Eq. (21), F_w = 75 cm^{-1} was used. This was done in order to obtain an absolute average difference less than 6.0 cm^{-1}, between the *ab initio* and fitted potential, for the points within 250 cm^{-1} from the minimum of the potential [45,49]. The value of the V_{min} in Eq. (22) was chosen to be 700 cm^{-1}. The value of the parameters used in the rovibrational calculations were: R_{start} = 3.50 Å, R_{end} = 8.00 Å, N_R = 38, N_{θ_1} = 48, N_{θ_2} = 24, N_ϕ = 40,

$N_F = 34$, $j_{max_1} = 20$, $j_{max_2} = 16$, and $\tau_L = 10^{-12}$ atomic units. In addition, the value of the rotational constants for the diatomic fragments were taken to be: 1.92252905 cm^{-1} [104] for $^{12}C^{16}O$, 1.83797220 cm^{-1} [105] for $^{13}C^{16}O$, 1.746408537 cm^{-1} [105] for $^{13}C^{18}O$, 6.4263650 cm^{-1} [80] for HI, and 3.25348718 cm^{-1} [80] for DI.

Ab initio potentials, with a large basis set, are computationally expensive to be calculated for the OC:HI complex. Thus, the PCM method is preferred over the CMM method. For the OC:HI system the PCM method, described in Eq. (9), was used with R_f selected to be 4.20 Å. However, the S_α has been expanded in Legendre polynomials $P_1(\cos\theta)$ in terms of θ_1 and θ_2 as

$$S_\alpha(\theta_1,\theta_2) = C_{\alpha,0,0} + C_{\alpha,1,0}\cos\theta_1 + C_{\alpha,0,1}\cos\theta_2 . \quad (64)$$

The dimensionless morphing parameters $C_{\alpha,i,j}$, in Eq. (64), are obtained by a regularized nonlinear least-squares optimization that minimizes the function in Eq. (7).

The experimental data used to morph the interaction potential of OC:HI is shown in Table 14. Such data includes previously reported IR experiments [101] as well as new microwave and IR data [106]. The values of G for the *ab initio* and morphed potentials, in Table 14, are G = 265.2 and G = 2.9 respectively, indicating the improvement in the overall agreement with experimental data obtained from the morphing procedure. In Table 15, final morphing parameters that yielded the best fit of the experimental data are given.

Table 14
Experimental data of OC:HI used in the fits and fitted values, and their uncertainties.

Observable[a]	Isotopomer/Isomer	$V_{ab\ initio}$	V_{morphed}	Exp	σ_k
B (GS)/10^{-2} cm^{-1}	^{16}O^{12}C-HI	2.954	3.009	3.005[b]	0.003
D_J (GS)/10^{-8} cm^{-1}	^{16}O^{12}C-HI	7.9	10.0	8.4[b]	0.5
B (GS)/10^{-2} cm^{-1}	^{16}O^{12}C-DI	2.946	2.999	3.000[b]	0.003
D_J (GS)/10^{-8} cm^{-1}	^{16}O^{12}C-DI	7.2	8.9	7.5[b]	0.5
B (GS)/10^{-2} cm^{-1}	^{16}O^{13}C-HI	2.894	2.948	2.944[b]	0.003
D_J (GS)/10^{-8} cm^{-1}	^{16}O^{13}C-HI	7.6	9.5	8.0[b]	0.5
B (GS)/10^{-2} cm^{-1}	^{16}O^{13}C-DI	2.887	2.938	2.940[b]	0.003
D_J (GS)/10^{-8} cm^{-1}	^{16}O^{13}C-DI	6.8	8.5	7.1[b]	0.5
B (GS)/10^{-2} cm^{-1}	^{18}O^{13}C-HI	2.708	2.758	2.755[b]	0.003
D_J (GS)/10^{-8} cm^{-1}	^{18}O^{13}C-HI	6.5	8.2	6.9[b]	0.5
B (ν_5^1)/10^{-2} cm^{-1}	^{16}O^{12}C-HI	3.046	3.132	3.110[c]	0.005
D_J (ν_5^1)/10^{-8} cm^{-1}	^{16}O^{12}C-HI	12.4	18.6	12.7[c]	2.0
$\langle P_2(\cos\theta_2)\rangle$ (GS)	^{16}O^{12}C-HI	0.764	0.752	0.736[b]	0.005
$\langle P_2(\cos\theta_2)\rangle$ (GS)	^{16}O^{12}C-DI	0.831	0.821	0.804[b]	0.005
$\langle P_2(\cos\theta_2)\rangle$ (GS)	^{16}O^{13}C-HI	0.766	0.754	0.738[b]	0.005
$\langle P_2(\cos\theta_2)\rangle$ (GS)	^{16}O^{13}C-DI	0.832	0.823	0.806[b]	0.005
$\langle P_2(\cos\theta_2)\rangle$ (GS)	^{18}O^{13}C-HI	0.767	0.755	0.739[b]	0.005
ν_5^1/cm^{-1}	^{16}O^{12}C-HI	30.41	25.96	25.89[c]	0.01
D_0 (^{16}O^{12}C-HI) - D_0 (^{16}O^{12}C-IH)		18.35	3.46	3.47[b]	0.01
B (GS)/10^{-2} cm^{-1}	^{16}O^{12}C-IH	3.710	3.866	3.865[b]	0.003
D_J (GS)/10^{-8} cm^{-1}	^{16}O^{12}C-IH	14.8	16.2	15.1[b]	1.0
B (GS)/10^{-2} cm^{-1}	^{16}O^{12}C-ID	3.716	3.871	3.869[b]	0.003
D_J (GS)/10^{-8} cm^{-1}	^{16}O^{12}C-ID	13.0	14.3	13.2[b]	1.0
B (GS)/10^{-2} cm^{-1}	^{16}O^{13}C-IH	3.639	3.793	3.791[b]	0.003
D_J (GS)/10^{-8} cm^{-1}	^{16}O^{13}C-IH	14.3	15.6	14.5[b]	1.0
B (ν_5^1)/10^{-2} cm^{-1}	^{16}O^{12}C-IH	3.737	3.893	3.932[c]	0.005
D_J (ν_5^1)/10^{-8} cm^{-1}	^{16}O^{12}C-IH	18.0	21.2	18.8[c]	2.0
$\langle P_2(\cos\theta_2)\rangle$ (GS)	^{16}O^{12}C-IH	0.811	0.814	0.817[b]	0.005
$\langle P_2(\cos\theta_2)\rangle$ (GS)	^{16}O^{12}C-ID	0.867	0.868	0.873[b]	0.005
$\langle P_2(\cos\theta_2)\rangle$ (GS)	^{16}O^{13}C-IH	0.813	0.816	0.819[b]	0.005
ν_5^1/cm^{-1}	^{16}O^{12}C-IH	29.97	28.24	28.31[c]	0.01
B (GS)/10^{-2} cm^{-1}	^{12}C ^{16}O-IH	4.069	4.045	4.044[b]	0.005
D_J (GS)/10^{-8} cm^{-1}	^{12}C ^{16}O-IH	-108.2	23.6	20.9[b]	5.0
B (GS)/10^{-2} cm^{-1}	^{12}C ^{16}O-HI	3.403	3.101	3.114[b]	0.005
D_J (GS)/10^{-8} cm^{-1}	^{12}C ^{16}O-HI	31.5	19.4	12.3[b]	5.0
G		265.2	2.9		

[a]GS = ground state.
[b]From [106].
[c]From [101].

Table 15
Optimized values for the morphing parameters of OC:HI.

(α,i,j)	$C^{(0)}_{\alpha,i,j}$	$C_{\alpha,i,j}$	σ
(1,0,0)	1.0	1.2556	0.0012
(1,1,0)	0.0	-0.2203	0.0007
(1,0,1)	0.0	0.0309	0.0006
(2,0,0)	1.0	0.8789	0.0084
(2,1,0)	0.0	0.0727	0.0035
(2,0,1)	0.0	0.0219	0.0087
(3,0,0)	0.0	0.0041	0.0003
(3,1,0)	0.0	0.0173	0.0003
(3,0,1)	0.0	(0.0)	Constrained

Table 16
Features of OC:HI potentials.

	Ab initio			Morphed		
Isomer	D_e (cm^{-1})	R (Å)	ΔD_e (cm^{-1})	D_e (cm^{-1})	R (Å)	ΔD_e (cm^{-1})
OC-IH	388.828	4.271	0.000	415(3)	4.180(11)	0
OC-HI	380.108	4.940	8.720	382(2)	4.900(7)	33(4)
CO-IH	240.882	4.029	147.946	363(3)	4.058(19)	52(4)
CO-HI	224.686	4.723	164.142	325(3)	4.941(17)	90(4)

Table 17
D_0 value for $^{16}O^{12}C$:HI and $^{16}O^{12}C$:DI isomers predicted from the morphed potential.

OC:HI			OC:DI		
Isomer	D_0 (cm^{-1})	ΔD_0 (cm^{-1})	Isomer	D_0 (cm^{-1})	ΔD_0 (cm^{-1})
$^{16}O^{12}C$-HI	213(1)	0.0	$^{16}O^{12}C$-ID	243(1)	0.0
$^{16}O^{12}C$-IH	209(1)	3.46(6)	$^{16}O^{12}C$-DI	238(1)	5.30(8)
$^{12}C\,^{16}O$-IH	200(2)	13(2)	$^{12}C\,^{16}O$-ID	226(2)	17(2)
$^{12}C\,^{16}O$-HI	198(2)	15(2)	$^{12}C\,^{16}O$-DI	217(2)	26(2)

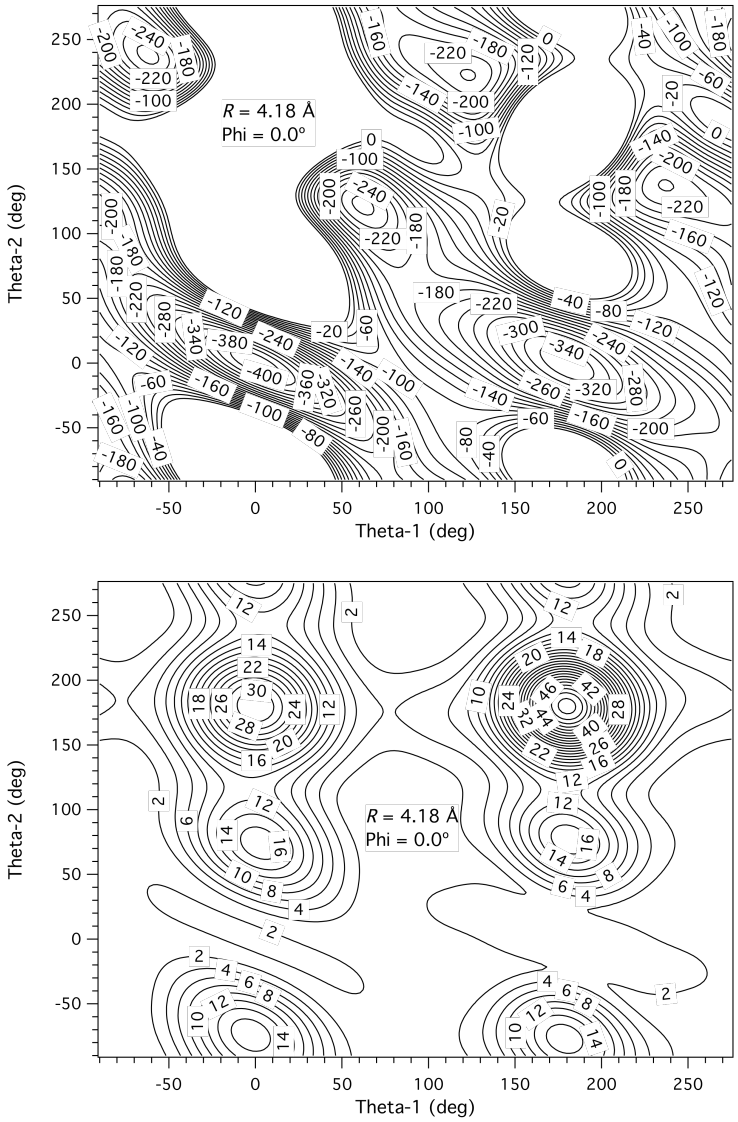

Figure 11. Morphed potential of $^{16}O^{12}C$:HI at R = 4.18 Å. In the top of the figure a two-dimensional slice of the interaction potential of $^{16}O^{12}C$:HI is shown. The corresponding estimated errors relative to the potential at infinite separation are shown in the bottom of the figure. The coordinates used are the Jacobi coordinates defined in Figure 1(b). All contours are in cm^{-1}.

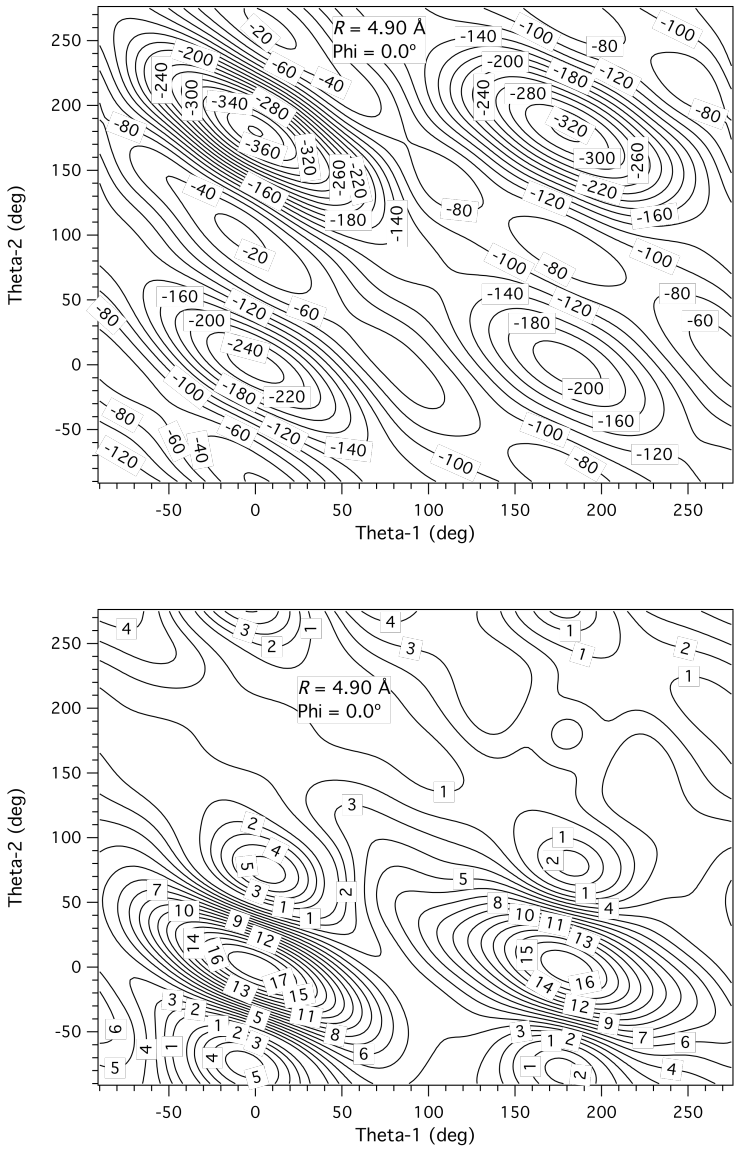

Figure 12. Morphed potential of $^{16}O^{12}C$:HI at R = 4.90 Å. In the top of the figure, a two-dimensional slice of the interaction potential of $^{16}O^{12}C$:HI is shown. The corresponding estimated errors relative to the potential at infinite separation are shown in the bottom of the figure. The coordinates used are the Jacobi coordinates defined in Figure 1(b). All contours are in cm^{-1}.

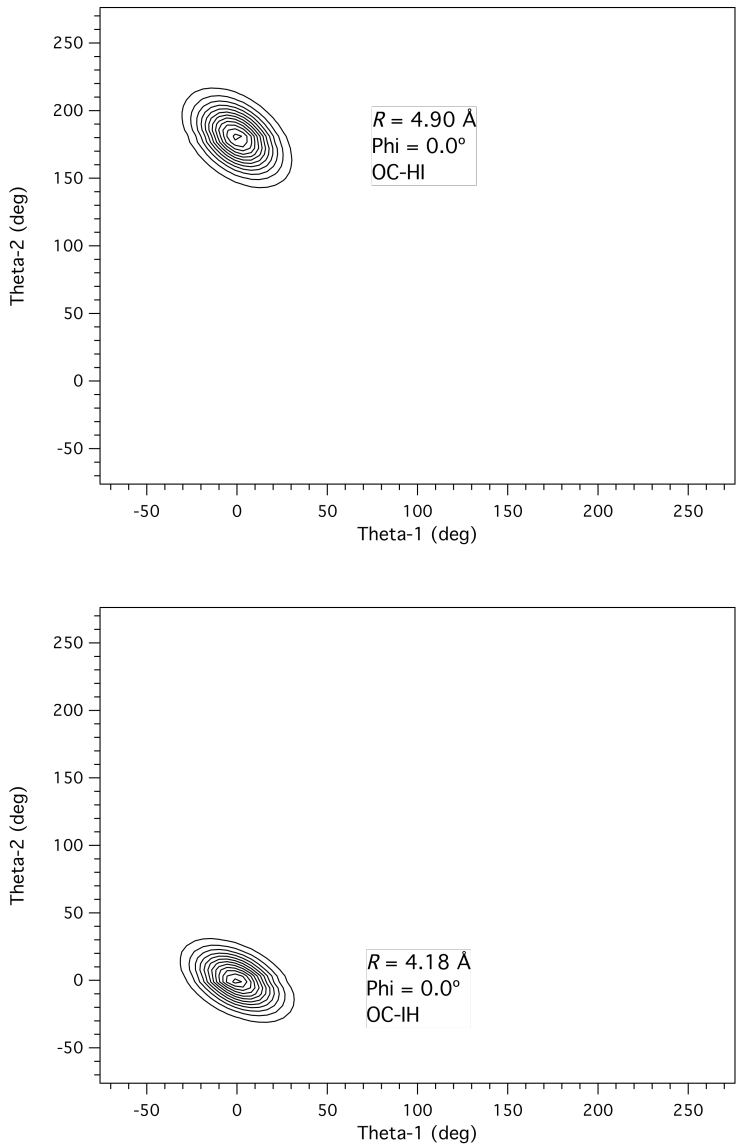

Figure 13. Ground state probability densities for $^{16}O^{12}C$-HI and $^{16}O^{12}C$-IH. The $^{16}O^{12}C$-HI isomer is the overall ground state of the complex. The coordinates used are the Jacobi coordinates defined in Figure 1(b).

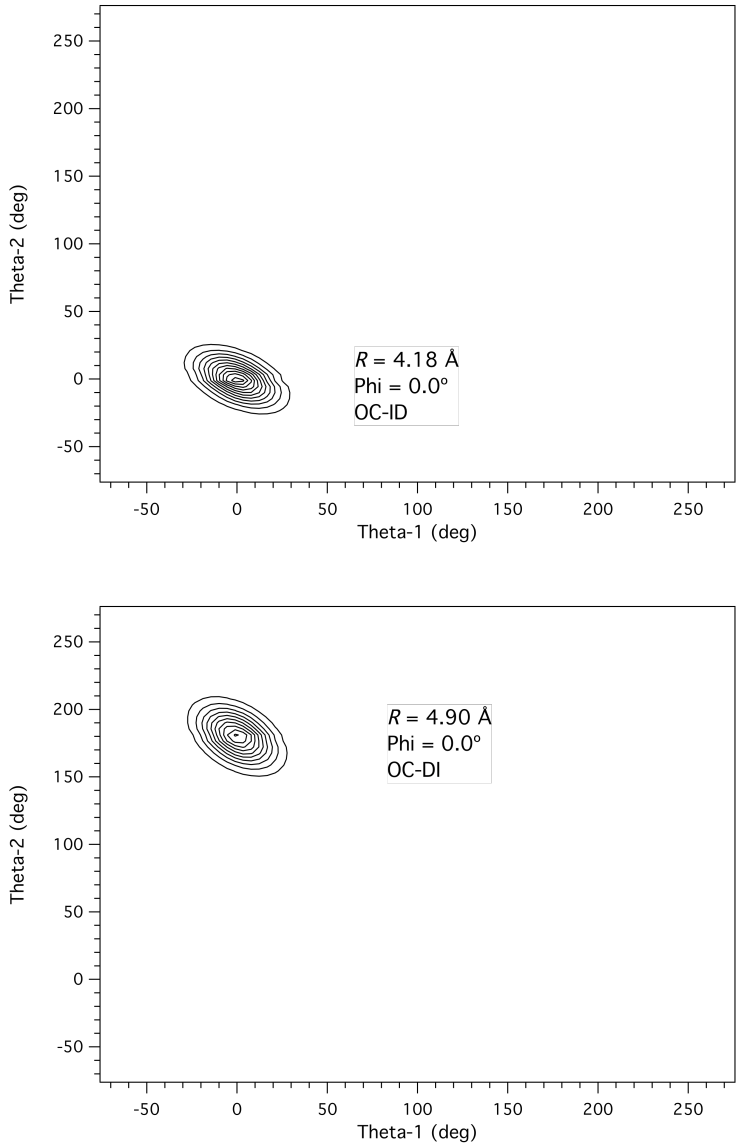

Figure 14. Ground state probability densities for $^{16}O^{12}C$-ID and $^{16}O^{12}C$-DI. The $^{16}O^{12}C$-ID isomer is the overall ground state of the complex. The coordinates used are the Jacobi coordinates defined in Figure 1(b).

The global minimum from the morphed potential (Figures 11 and 12) is consistent with a linear van der Waals OC-IH structure, with a value of $R = 4.180(11)$ Å. Table 16 indicates the minimum energy (expressed as D_e) associated with the four minima, OC-IH, OC-HI, CO-IH, and CO-HI, and the corresponding R values that are associated with each minimum. The predicted ground state energies, or D_0, from the morphed potential, for the isomers of $^{16}O^{12}C$:HI and $^{16}O^{12}C$:DI, are given in Table 17. Furthermore, the ground state probability densities for the two lowest isomers of $^{16}O^{12}C$:HI and $^{16}O^{12}C$:DI are shown in Figures 13 and 14.

As it had been previously proposed [100-102], the present results are consistent with the previously proposed ground state structure, which is indeed the OC-HI configuration (see Figure 13). However, these results indicate as well that the global minimum does not have the OC-HI structure but the OC-IH structure. This is a characteristic that is very similar to what occurs in Ar:HBr [23,107], Kr:HBr [25], and He:CH_3F [31]. The global minimum structure OC-IH is predicted to be 33(4) cm^{-1} more stable than the corresponding local minimum associated with the OC-HI structure. Thus, the ground state and global minimum structures are predicted to be different, giving a further indication that this system is a potential candidate for demonstrating ground state isotopic isomerization. This unusual isomerization gives cause for extreme caution when applying generalized methods, such as the application of Kraitchman's equations [108] to determine r_s, and the determination of r_m [109], using limited data from spectroscopic investigation of weakly bound dimers and clusters.

The fundamental conclusion that can be made from the determined morphed potential is the prediction that the OC:DI dimer ground state has an OC-ID structure, and that it is predicted to be 5.30(8) cm^{-1} more stable than the corresponding hydrogen bond OC-DI structure (see Figure 14). The significantly higher barrier (382(4) cm^{-1}) of isomerization results in more localized wave functions than those that occur in Ar:HBr, and consequently, significantly lowers transition cross-sections; particularly for direct transitions between respective deuterated isomers. Thus, the experimental observation of the isomerization of OC-DI to OC-ID will be extremely challenging, unless infrared double resonance techniques are applied.

It is emphasized that the ground state isotopic isomerization found in OC:HI is probably not unique. The current study involves ground state isomerization from a hydrogen-bonded structure to a deuterated van der Waals structure. However, there are some indications that such isomerization may be occurring in the van der Waals ground state structure of CO_2:BrH [110], as well as in Ar:H_2S [111]. Further studies will be needed to confirm such effects.

The intermolecular morphed potential of OC:HI, that has been generated, is consistent with four linear isomeric structures. The global minimum is characterized to be the linear OC-IH isomer with R = 4.180(11) Å. In addition, the present results are consistent with the ground state having the OC-HI configuration. The ground state molecular isotopic isomerization is predicted from the morphed potential. From this potential, it is found that the OC-ID structure is 5.30(8) cm^{-1} more stable than the corresponding hydrogen bound OC-DI structure. It is emphasized that confirmation of

this anomalous isotopic effect must await further spectroscopic investigations.

The differences in stability of the OC-IH and CO-IH can be attributed to the interactions of the carbon and oxygen lone pairs, with the anti-bonding orbital on HI [112]. Since the orbital energy of the lone pair electrons of carbon are higher that the corresponding energy levels in oxygen, it makes it a better electron density donor to the anti-bonding orbital on HI. On the other hand, the stability of OC-IH over OC-HI, and CO-IH over CO-HI, is due to the fact that the polarization interactions of the HI is smaller, with larger dispersion effects; thus favoring van der Waals interaction over the hydrogen bond interaction.

4.5 HI:CO_2

In the previous sections it was concluded that the global minimum, in the potential surfaces of the OC:HCl and OC:HBr complexes, were the OC-HCl and OC-HBr linear configurations. However, for the OC:HI complex, it was found that the global minimum in the potential surface have an OC-IH linear configuration. These results imply a competition between the hydrogen bond and the van der Waals interactions in the OC:HX (X= Cl, Br, I) complexes. In this section, the HI:CO_2 system is studied to investigate the competition of intermolecular forces that occur in the HX:CO_2 complexes, compare to those observed in the OC:HX complexes.

Although the HI:CO_2 complex has been extensively studied in photodissociation experiments [113-117], studies on the structure of the complex have been limited. The

complex has been used to control the orientation of the collision in bimolecular reactions like H + CO_2. Recently Jabs et al. [30] reported the microwave spectra of HI:CO_2 using pulsed-nozzle Fourier transform microwave spectroscopy. The equilibrium and ground state of the complex was found to be planar, with a quasi-T-shaped geometry with the hydrogen atom tilted toward the CO_2 moiety.

In the *ab initio* calculation, the bond length of the HI was fixed at the experimental r_e: 1.60916 Å [79]. The C-O bond lengths in CO_2 were taken to be 1.162453 Å [118], which is the averaged distance in the ground rovibrational state of the isolated molecule. The interaction energy of the HI:CO_2 complex was calculated at the CCSD(T) level of theory. The aug-cc-pVTZ basis set was used for all the atoms, except for the iodine, for which the basis set was the pseudopotential aug-cc-pVTZ-pp. The potential energy surface was calculated on a grid built taking 9 different *R* points (3.50 Å, 4.00 Å, 4.25 Å, 4.50 Å, 4.75 Å, 5.00 Å, 5.50 Å, 6.50 Å, and 8.00 Å), 5 points for both θ_1 and θ_2 (25.02°, 57.42°, 90.00°, 122.58°, and 154.98°), and 10 points for ϕ (18.0°, 54.0°, 90.0°, 126.0°, 162.0°, 198.0°, 234.0°, 270.0°, 306.0°, and 342.0°). This set of points was supplemented with a selection of 20 specific angular points (θ_1,θ_2,ϕ) for each value of *R*, giving a final grid composed of 2,430 points, defined in Figure 1(b). These 20 specific angular points are (0.0°, 0.0°, 0.0°), (0.0°, 180.0°, 0.0°), (60.0°, 0.0°, 0.0°), (60.0°, 120.0°, 0.0°), (60.0°, 160.0°, 0.0°), (72.0°, 125.0°, 0.0°), (80.0°, 100.0°, 0.0°), (90.0°, 80.0°, 0.0°), (90.0°, 80.0°, 180.0°), (90.0°, 90.0°, 0.0°), (90.0°, 90.0°, 180.0°), (90.0°, 110.0°, 0.0°), (90.0°, 110.0°, 180.0°), (100.0°, 100.0°, 180.0°), (108.0°,

125.0°, 180.0°), (120.0°, 0.0°, 180.0°), (120.0°, 120.0°, 180.0°), (120.0°, 160.0°, 180.0°), (180.0°, 0.0°, 180.0°), and (180.0°, 180.0°, 180.0°). In the fitting of the *ab initio* potential, the weighing factor, in Eq. (21), F_w = 75 cm^{-1} was used. This was done in order to obtain an absolute average difference less than 6.0 cm^{-1}, between the *ab initio* and fitted potential, for the points within 350 cm^{-1} from the minimum of the potential [45,49]. The value of the V_{min} in Eq. (22) was chosen to be 700 cm^{-1}. The value of the parameters used in the rovibrational calculations were: R_{start} = 3.50 Å, R_{end} = 8.00 Å, N_R = 38, N_{θ_1} = 48, N_{θ_2} = 24, N_ϕ = 54, N_F = 34, j_{max_1} = 26, j_{max_2} = 22, and $\tau_L = 10^{-12}$ atomic units. In addition, the value of the rotational constants for the diatomic fragments were taken to be: 0.390219027 cm^{-1} [119] for $^{12}C^{16}O_2$, 0.368185104 cm^{-1} [119] for $^{12}C^{16}O^{18}O$, 0.346817311 cm^{-1} [119] for $^{12}C^{18}O_2$, 6.4263650 cm^{-1} [80] for HI, and 3.25348718 cm^{-1} [80] for DI.

In a similar manner to the OC:HI system, *ab initio* potentials with large basis set are computationally too expensive to be calculated for the HI:CO_2 complex. Thus, the PCM method is preferred over the CMM method. For HI:CO_2, the PCM method described in Eqs. (9) to (12) was used, with R_f selected to be 3.90 Å. The experimental microwave data [30] used to morph the interaction potential of the HI:CO_2 complex is shown in Table 18.

Table 18
Experimental data of HI:CO_2 used in the fits and fitted values, and their uncertainties.

Isotopomer	Observable[a]	Units	$V_{ab\ initio}$	V_{morphed}	Exp[b]	σ_k
HI-$^{12}C^{16}O_2$	A	cm^{-1}	0.459	0.416	0.421	0.003
	$(B+C)/2$	10^{-2} cm^{-1}	3.191	3.462	3.462	0.002
	Δ_{JK}	10^{-8} cm^{-1}	2325.8	520.0	560.5	10.0
	$\langle P_2(\cos\theta_2)\rangle$		-0.317	-0.351	-0.350	0.001
HI-$^{12}C^{18}O_2$	A	cm^{-1}	0.414	0.374	0.379	0.003
	$(B+C)/2$	10^{-2} cm^{-1}	2.989	3.243	3.243	0.002
	Δ_{JK}	10^{-8} cm^{-1}	2483.8	520.4	475.7	10.0
	$\langle P_2(\cos\theta_2)\rangle$		-0.316	-0.351	-0.350	0.001
HI-$^{12}C^{18}O^{16}O$	A	cm^{-1}	0.362	0.358	0.355	0.003
	$(B+C)/2$	10^{-2} cm^{-1}	3.093	3.354	3.351	0.002
	$\langle P_2(\cos\theta_2)\rangle$		-0.309	-0.345	-0.346	0.001
HI-$^{12}C^{16}O^{18}O$	A	cm^{-1}	0.363	0.360	0.356	0.003
	$(B+C)/2$	10^{-2} cm^{-1}	3.084	3.340	3.342	0.002
	$\langle P_2(\cos\theta_2)\rangle$		-0.324	-0.357	-0.355	0.001
	G		101.5	2.0		

[a]Observables for the ground vibrational state of the complex.
[b]From [30].

Table 19
Optimized values for the parameters of the morphing functions of HI:CO_2.

α	i	$\lambda_{\alpha,i} = (l_x$	n	θ'_1	θ'_2	$\phi')$	$C^{(0)}_{\alpha,i}$	$C_{\alpha,i}$	σ
1	1	0					1.0	1.0433	0.0084
2	1	0					1.0	(1.0)	Constrained
3	1	0					0.0	0.0380	0.0002
1	2	2	2	90	90	0	0.0	0.2181	0.0039

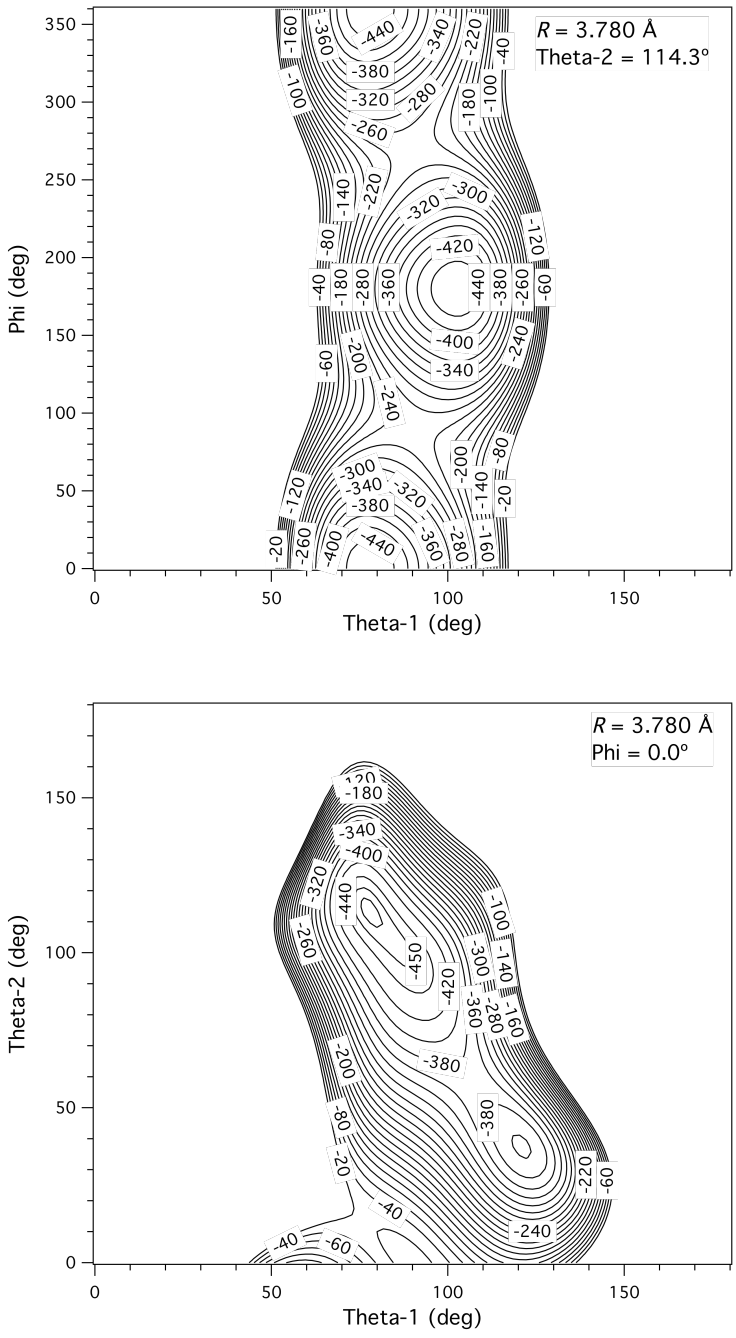

Figure 15. Morphed interaction potential of HI:$^{12}C^{16}O_2$. The coordinates used are the Jacobi coordinates defined in Figure 1(b). All contours are given in cm^{-1}.

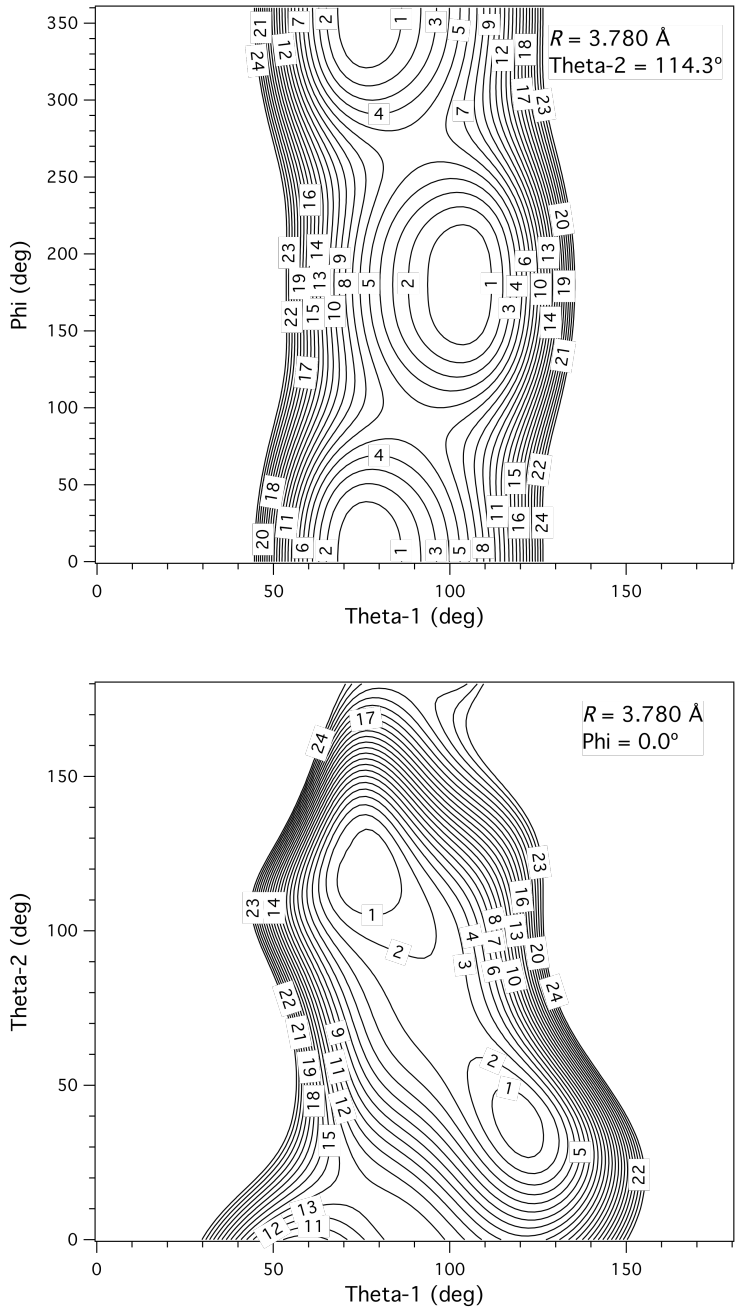

Figure 16. Corresponding statistical uncertainties for the morphed potential of HI:$^{12}C^{16}O_2$. The statistical uncertainties are relative to the minimum of the potential which occurs at R = 3.780(1) Å, θ_1 = 77.9(1)º, θ_2 = 114.3(1)º, and ϕ = 0.0(1)º, with V = -457(14) cm^{-1}. The coordinates used are the Jacobi coordinates defined in Figure 1(b). All contours are given in cm^{-1}.

The *ab initio* potential was morphed using three morphing functions, two with no angular dependence (i.e. $l_x = 0$), and one localized angular function with $l_x = 2$ (Table 19). During the fitting procedure, the morphing parameter $C_{2,1}$ was not included as it could not be determined with statistical significance, and it did not change the quality of the final fit. The final RMS after the morphing was $G = 2.0$, which indicates an improved agreement with the experimental data, when compared to the original *ab initio* data of $G = 101.5$.

Two equivalent global minima (see Figures 15 and 16), with a well depth of 457(14) cm^{-1}, were determined to correspond to the geometries R = 3.780(1) Å, θ_1 = 77.9(1)°, θ_2 = 114.3(1)°, ϕ = 0.0(1)°, and R = 3.780(1) Å, θ_1 = 102.1(1)°, θ_2 = 114.3(1)°, ϕ = 180.0(1)°; separated by a barrier of 181(17) cm^{-1}. The top of the barrier was located at the geometry R = 3.818(1) Å, θ_1 = 90.0(1)°, θ_2 = 98.1(1)°, ϕ = 90.0(1)°, which corresponds to a T-shaped geometry with the hydrogen being located out-of-plane. The morphed potential also has a secondary minimum, with a well depth of 405(14) cm^{-1}, at the geometry R = 3.875(1) Å, θ_1 = 124.4(1)°, θ_2 = 35.4(1)°, ϕ = 0.0(1)°. The determined global minimum for the HI-CO_2 complex, 457(14) cm^{-1}, compares the values of 837 cm^{-1}, 576 cm^{-1}, and 397 cm^{-1}, for CO_2-HF, CO_2-HCl, and HBr-CO_2 respectively [120]. In addition, an MP2 calculation [121] predicts a value of 392 cm^{-1} for HBr-CO_2. The morphed potential predicts the dissociation energy, D_0, of HI-CO_2 to be 341(14) cm^{-1}. As a comparison, the D_0 for CO_2-HF was experimentally determined to be 672(4) cm^{-1} [122], while it is estimated to be 430 cm^{-1} for CO_2-HCl [123].

It should be noted that in Table 18, the values of A in HI-$^{12}C^{16}O_2$ and HI-$^{12}C^{18}O_2$ are significantly larger that those in the mono-^{18}O substituted complexes. This difference is not commensurate with an isotopic effect, but can be interpreted as a consequence of the hindered rotation of the HI monomer in the HI-CO_2 complex. The hindered rotation of the HI monomer can occur via two significant pathways: in-plane and out-of-plane. Based on the morphed potential, the most probable pathway for the hindered rotation occurs out-of-plane, around the a-axis of the molecule, and as described by the angle ϕ (see Figure 15). Along this pathway, the estimated height of the barrier of 181(17) cm^{-1} can be compared to the value of 184 cm^{-1} for HBr-CO_2 [121]. This gives the frequency of tunneling through the barrier the following values: 0.037 cm^{-1} for HI-$^{12}C^{16}O_2$, 0.035 cm^{-1} for HI-$^{12}C^{18}O_2$ and 0.001 cm^{-1} for DI-$^{12}C^{16}O_2$. As a consequence of the Bose-Einstein statistics, for the spin-zero oxygen nuclei, only symmetric states were allowed, in the ground vibrational state, for even K_a, and only antisymmetric states for odd K_a. Consequently, rotation-tunneling transitions were observed for the complexes HI-$^{12}C^{16}O_2$ and HI-$^{12}C^{18}O_2$. Thus, the observed discrepancy in the rotational constant A can be attributed to the allowed transitions in the symmetric complexes, from the K_a=0 symmetric state to the K_a=1 antisymmetric state. Therefore, the rotational constant A for the symmetric complexes will have a larger magnitude by the value of the tunneling splitting. In the case of the mono-^{18}O substituted complexes, the morphed potential confirms the picture of pure rotational spectra observed in the experimental data. Since the oxygen atoms are not equivalent, the tunneling does not occur. The experimental data determined the ground state geometry of the HI-CO_2

complex to be planar, with the heavy atoms having a quasi-T-shape configuration and a geometry of θ_1 = 82.30(1)° and θ_2 = 108.45(1)° [30]. This quasi-T-shaped geometry differs significantly from the one observed in HBr-CO_2 [110], and the linear geometries found for CO_2-HCl [124] and CO_2-HF [125]. In contrast to the systems CO_2-HX (X = F, Cl, Br) there is no experimental data available for DI-CO_2. However, based on the morphed potential, it is possible to predict the values of the spectroscopic constants, for the ground vibrational state, of DI-$^{12}C^{16}O_2$ to be: A = 0.361(6) cm^{-1}, $(B+C)/2$ = 0.03460(4) cm^{-1}, and $\langle P_2(\cos\theta_2)\rangle$ = -0.367(2).

The determined morphed potential of HI:CO_2 is characterized by two equivalent global minima with a well depth of 457(14) cm^{-1}. It has a planar quasi-T-shaped structure, with the hydrogen atom tilted toward the CO_2 moiety, and separated by a barrier of 181(17) cm^{-1}. Also, the morphed potential has a secondary minimum with a well depth of 405(14) cm^{-1}, and a planar quasi-T-shaped structure with the hydrogen atom tilted away from the CO_2 moiety. An interesting feature revealed by the morphed potential of HI:CO_2 is that the complex has a linear OCO-HI geometry when the separation of the monomers is large (i.e., R = 6.0 Å). In addition, when the distance between the monomers is shorter than the equilibrium distance (i.e., R = 3.0 Å), the complex has a T-shaped geometry with θ_1 = 92.0º, θ_2 = 96.1º and ϕ = 0.0º. The model obtained in this study has direct relevance to further understanding the photoinitiated reactions in H_nX:CO_2 complexes (X = Cl, Br, I, n =1 and X = S, n = 2). The determined structure is now available for interpreting regiospecific effects, in photoinitiated reaction dynamics, of the HI:CO_2 complex and its clusters.

4.6 OC:HF

In the previous sections, the potential morphing methodology was applied to systems in four-dimensional vibrational approximation. In this section, the potential morphing methodology is extended to six-dimensions, in order to morph the vibrationally-complete six-dimensional potential of OC:HF system. The results presented in this section are a key step in the future development of potential morphing theories in systems of higher dimensions, as OC:HF is a prototypical system for the simplest heteromolecular hydrogen bonds.

The OC:HF complex was first observed experimentally using pulsed supersonic jet Fourier transform microwave spectroscopy [93,95]. These studies demonstrated that the equilibrium geometry is linear with the atoms in the order OC-HF. In addition, electric and magnetic properties of OC-HF have also been studied [126,127]. The values of the ν_1, ν_2, and ν_4^1 vibrational frequencies were initially determined to be 3789.3(3) cm^{-1}, 2162.4(3) cm^{-1}, and 389.5(5) cm^{-1}, using infrared spectra in solid argon matrices [94]. Analysis of the intramolecular bands ν_1 and ν_2, located at 3844.0294(50) cm^{-1} and 2167.69904(11) cm^{-1} were reported using a single frequency mode hop color center laser [128] and diode-laser spectroscopy [129]. A reinvestigation of the sub-Doppler resolution infrared spectrum, of the ν_1 intramolecular band [130], provided a precise evaluation, of the lifetime of the excited state, of 0.9(1) ns. A further investigation provided hot bands, associated with the ν_1 intramolecular band [131], and the ν_5^1

vibrational frequency was estimated to be 80(12) cm^{-1}. Subsequent studies of the ν_1 intramolecular band have been undertaken [132,133]. This includes the analysis of the ^{18}O and ^{13}C isotopic species in the complex, which shows an anomalous shift of the ν_1 band origin, attributed to anharmonic coupling of the zero-point CO bending motion [132]. In addition, the values of ν_1 and ν_2 for OC-DF were recorded using a supersonic jet Fourier transform infrared spectrometer [134]. Afterwards, the analysis of state-to-state dissociation dynamics [135] determined the dissociation energy $D_0 = 732 \pm 2$ cm^{-1}. Lastly, valuable spectroscopic constants of the OC-HF complex at the $\upsilon_{HF} = 3$ level have been observed [136].

The OC:HF complex has also been the subject of extensive theoretical work [84,112,137-149]. The theory included in such work varies, from *ab initio* calculations [84,112,137-144,147] to density functional theory (DFT) [143-145,149], to molecular mechanics for clusters (MMC) [146], and to natural bond orbital (NBO) [112,147] analysis. A model based on atom-atom potentials and multipole moments [148] has also been applied to the OC:HF complex and other weakly bound systems. In general, the computed properties include: dimer equilibrium geometry, vibrational frequencies, and binding energies. All theoretical work agrees that the global minimum of the PES is the linear OC-HF, which is in agreement with the experiments. However, the theory predicted a secondary minimum in the surface, which is the linear CO-HF. The observations of the CO-HF isomer until now have been limited to high-pressure gas phase and matrix isolation experimental studies [150-153]. Besides all the extensive

work on the OC:HF system, a six-dimensional potential energy surface is needed in order to provide insights into the dissociation dynamics of the complex [135]. Lastly, as it has been pointed out by Curtiss et al. [112,147], the differences in stability of the OC-HF and CO-HF is attributed to the interactions of the carbon and oxygen lone pairs with the anti-bonding orbital on HF, rather than to the low order electrostatic contributions.

The six *ab initio* potentials calculated for the OC:HF complex are: (i) CCSD(T)/aug-cc-pVTZ, (ii) MP2/aug-cc-pVQZ, (iii) MP2/aug-cc-pVTZ, (iv) HF/aug-cc-pVQZ, (v) HF/aug-cc-pVQZ-DK, and (vi) CCSD(T)/aug-cc-pVTZ without the CP correction. All of these six *ab initio* potentials were calculated in a six-dimensional grid of 149,940 $\left(R,r_1,r_2,\theta_1,\theta_2,\phi\right)$ points, defined in Figure 1(c). The R distance was varied by using a 17 point grid (2.90 Å, 2.95 Å, 3.00 Å, 3.10 Å, 3.30 Å, 3.50 Å, 3.65 Å, 3.80 Å, 4.00 Å, 4.25 Å, 4.50 Å, 4.75 Å, 5.00 Å, 5.50 Å, 6.00 Å, 6.50 Å, and 7.00 Å); the CO bond length, r_1, was varied by using a 5 point grid (0.978902 Å, 1.053438 Å, 1.128323 Å, 1.219632 Å, and 1.362541 Å); the HF bond length, r_2, was varied by using a 7 point grid (0.701767 Å, 0.733069 Å, 0.784496 Å, 0.916808 Å, 1.113087 Å, 1.254045 Å, and 1.380656 Å); the angles θ_1 (the CO angle) and θ_2 (the HF angle) was varied by using a 5 point grid (10.0°, 50.0°, 90.0°, 130.0°, and 170.0°); and the dihedral angle ϕ was varied by using a 10 point grid (10.0°, 50.0°, 90.0°, 130.0°, 170.0°, 190.0°, 230.0°, 270.0°, 310.0°, and 350.0°). The six-dimensional grid was supplemented with additional points at all values of R, r_1, and r_2, and with θ_1 = 0.0º and 180.0º, θ_2 = 180.0º, and ϕ = 0.0º.

In the interpolating moving least-squares procedure an accurate representation of the interaction potentials was obtained using 55 angular functions, defined in Eq. (19), in which $L_1 = L_2 = 0$ to 4, $L = 0$ to (L_1+L_2), and L_1+L_2+L is an even number. The parameters χ, n, and ε in Eq. (26) were chosen to be 0.423 radians^{-2}, 2, and 10^{-12} radians^2 (5.730×10^{-11} degrees^2) respectively. The parameter V_M in Eq. (28) was chosen to be 300 cm^{-1}. For the OC:HF system in Eq. (28), the $q_1^{2,3}$ radial reproducing kernel was used. The $q_1^{2,3}$ function is defined in Eq. (65) and it accounts for the asymptotic form $1/R^3$, of the dipole-dipole interaction potential, in OC:HF.

$$q_1^{2,3}\left(R,R'\right)=\frac{1}{5R_>^4}\left\{1-\frac{2}{3}\frac{R_<}{R_>}\right\} \tag{65}$$

Eq. (65) behaves asymptotically as $1/R^4$, and if a continuous set of radial reproducing kernel is used, it will yield the correct functional form of the potential ($1/R^3$). The $R_>$ and $R_<$ in Eq. (65) are respectively the larger and smaller of R and R'.

In Eq. (37), the value of N for the CO RKR potential [154] was $N = 18$, for the HF RKR potential [155] it was $N = 26$, and it was $N = 20$ for the DF RKR potential [155]. The convergence of the adiabatic potential, and rovibrational energy calculations, depends on the selection of the following parameters: R_{start} = 2.90 Å, R_{end} = 7.00 Å, $r_{CO,start}$ = 0.90 Å, $r_{CO,end}$ = 1.50 Å, $r_{HF,start}$ = 0.55 Å, $r_{HF,end}$ = 1.80 Å, $N_R = 54$, $N_{r_{CO}} = N_{r_{HF}} =$ 701, $N_{\theta_{CO}} = N_{\theta_{HF}} = 24$, and $N_\phi = 38$. The number of radial spectral basis functions is $N_F =$ 50. All of the summations, over spectral states, are truncated so that $j_{max_{CO}} = 20$ and $j_{max_{HF}} = 16$, as well as including all possible values of m_{CO} and m_{HF}. The tolerance (τ_L)

used to determine the convergence, of the eigenvalues, in the Lanczos procedure [58] was 10^{-12} atomic units. In the VSCF calculations, N_{NC} = 8 and τ_{VSCF} = 10^{-11} atomic units. In addition, the value of the rotational constants for the diatomic fragments, in Eq. (58), were calculated with the fixed angular coordinates $\left(\theta_{CO}^{f},\theta_{HF}^{f},\phi^{f}\right)$ chosen to be (20.0°, 160.0°, 0.0°).

The CMM method in Eq. (61) was used to morph the interaction potential of OC:HF. In Eq. (61), the value of R_f was chosen to be 3.65 Å. The parameter C_5 was constrained to zero because the six-dimensional HF/aug-cc-pV5Z potential, for OC:HF, was not available. The experimental data used to morph the PES of OC:HF is shown in Table 20. The values of *G*, for the $V_{CMM}^{(0)}$ and morphed potential ($V_{CMM}^{(4)}$), given in Table 20 are *G* = 57.4 and *G* = 0.9, respectively, indicating the improvement in the overall agreement with experimental data obtained through the morphing procedure. In Table 21, the final morphing parameters that yielded the best fit of the experimental data are given. As apparent in Table 21, the values of the C_4 and C_6 parameters were constrained to one, because their value could not be determined with statistical significance, and they did not change the quality of the final fit. Contrary to the four-dimensional cases, the radial correction was found to be important in order to fit the experimental data. If the C_7 parameter is constrained to zero, the value of *G* for the morphed potential ($V_{CMM}^{(3)}$), in Table 20, is *G* = 3.1. As a comparison, the non-relativistic CCSD(T)/aug-cc-pVTZ *ab initio* potential gave a value of *G* = 181.5.

Table 20
Experimental data of OC:HF used in the fits and fitted values, and their uncertainties.

Observable[a]	Isotopomer	$V_{CMM}^{(0)}$	$V_{CMM}^{(3)}$	$V_{CMM}^{(4)}$	Exp	σ_k
B (GS)/10^{-2} cm^{-1}	$^{16}O^{12}C$-HF	10.158	10.203	10.221	10.220[b]	0.003
D_J (GS)/10^{-8} cm^{-1}	$^{16}O^{12}C$-HF	33.0	32.6	32.8	32.6[b]	3.0
B (GS)/10^{-2} cm^{-1}	$^{16}O^{12}C$-DF	10.103	10.145	10.164	10.167[b]	0.003
D_J (GS)/10^{-8} cm^{-1}	$^{16}O^{12}C$-DF	31.2	30.9	31.1	31.4[b]	3.0
$\Delta\nu_1$/cm^{-1}	$^{16}O^{12}C$-HF	-115.80	-117.38	-117.39	-117.39[c]	0.01
B (ν_1)/10^{-2} cm^{-1}	$^{16}O^{12}C$-HF	10.362	10.407	10.426	10.425[c]	0.005
D_J (ν_1)/10^{-8} cm^{-1}	$^{16}O^{12}C$-HF	30.3	30.1	30.3	30.2[c]	5.0
B (ν_1)/10^{-2} cm^{-1}	$^{16}O^{12}C$-DF	10.246	10.288	10.307	10.311[d]	0.005
D_J (ν_1)/10^{-8} cm^{-1}	$^{16}O^{12}C$-DF	29.5	29.3	29.5	31.1[d]	5.0
$\Delta\nu_2$/cm^{-1}	$^{16}O^{12}C$-HF	24.35	24.43	24.46	24.43[e]	0.01
B (ν_2)/10^{-2} cm^{-1}	$^{16}O^{12}C$-HF	10.095	10.140	10.158	10.155[e]	0.005
D_J (ν_2)/10^{-8} cm^{-1}	$^{16}O^{12}C$-HF	33.3	32.9	33.1	34.5[e]	5.0
$\Delta\nu_2$/cm^{-1}	$^{16}O^{12}C$-DF	25.49	25.54	25.58	25.59[d]	0.01
B (ν_2)/10^{-2} cm^{-1}	$^{16}O^{12}C$-DF	10.040	10.083	10.101	10.104[d]	0.005
D_J (ν_2)/10^{-8} cm^{-1}	$^{16}O^{12}C$-DF	31.4	31.1	31.3	33.6[d]	5.0
ν_5^1/cm^{-1}	$^{16}O^{12}C$-HF	80.96	82.02	81.98	81.97[f]	0.01
B (ν_5^1)/10^{-2} cm^{-1}	$^{16}O^{12}C$-HF	10.240	10.285	10.304	10.303[f]	0.005
D_J (ν_5^1)/10^{-8} cm^{-1}	$^{16}O^{12}C$-HF	36.7	36.2	36.4	37.0[f]	5.0
Δ ($\nu_1+\nu_5^1-\nu_5^1$)/cm^{-1}	$^{16}O^{12}C$-HF	-110.30	-111.99	-111.98	-111.98[g]	0.01
B ($\nu_1+\nu_5^1$)/10^{-2} cm^{-1}	$^{16}O^{12}C$-HF	10.446	10.491	10.510	10.506[g]	0.005
D_J ($\nu_1+\nu_5^1$)/10^{-8} cm^{-1}	$^{16}O^{12}C$-HF	33.5	33.2	33.4	33.0[g]	5.0
Δ ($\nu_2+\nu_5^1$)/cm^{-1}	$^{16}O^{12}C$-HF	103.97	105.11	105.10	105.12[f]	0.01
B ($\nu_2+\nu_5^1$)/10^{-2} cm^{-1}	$^{16}O^{12}C$-HF	10.177	10.223	10.242	10.239[f]	0.005
D_J ($\nu_2+\nu_5^1$)/10^{-8} cm^{-1}	$^{16}O^{12}C$-HF	37.1	36.5	36.8	36.3[f]	5.0
G		57.4	3.1	0.9		

[a]GS = ground state.
[b]From [93]. [c]From [132]. [d]From [134]. [e]From [129].
[f]Unpublished data provided by Dr. J. W. Bevan.
[g]From [131].

Table 21
Optimized values for the morphing parameters of OC:HF.

α	$C_\alpha^{(0)}$	$C_\alpha^{(3)}$	σ for $C_\alpha^{(3)}$	$C_\alpha^{(4)}$	σ for $C_\alpha^{(4)}$
1	1.0	0.9869	0.0004	0.9894	0.0004
2	0.0	-0.2617	0.0036	-0.2362	0.0040
3	1.0	0.9745	0.0008	0.9786	0.0008
4	(1.0)	(1.0)	Constrained	(1.0)	Constrained
5	(0.0)	(0.0)	Constrained	(0.0)	Constrained
6	(1.0)	(1.0)	Constrained	(1.0)	Constrained
7	0.0	(0.0)	Constrained	0.0012	0.0001

Table 22
Relativistic effects in the computed observables of OC:HF.

Observable[a]	Isotopomer	$V^{(0)}_{\mathrm{CMM}}$ Relativistic	$V^{(0)}_{\mathrm{CMM}}$ Non-Relativistic	$V^{(4)}_{\mathrm{CMM}}$ Relativistic	$V^{(4)}_{\mathrm{CMM}}$ Non-Relativistic
B (GS)/10^{-2} cm^{-1}	^{16}O^{12}C-HF	10.158	10.162	10.221	10.221
D_J (GS)/10^{-8} cm^{-1}	^{16}O^{12}C-HF	33.0	32.9	32.8	32.9
B (GS)/10^{-2} cm^{-1}	^{16}O^{12}C-DF	10.103	10.106	10.164	10.164
D_J (GS)/10^{-8} cm^{-1}	^{16}O^{12}C-DF	31.2	31.1	31.1	31.1
$\Delta\nu_1$/cm^{-1}	^{16}O^{12}C-HF	-115.80	-116.84	-117.39	-117.40
B (ν_1)/10^{-2} cm^{-1}	^{16}O^{12}C-HF	10.362	10.368	10.426	10.426
D_J (ν_1)/10^{-8} cm^{-1}	^{16}O^{12}C-HF	30.3	30.2	30.3	30.3
B (ν_1)/10^{-2} cm^{-1}	^{16}O^{12}C-DF	10.246	10.251	10.307	10.308
D_J (ν_1)/10^{-8} cm^{-1}	^{16}O^{12}C-DF	29.5	29.4	29.5	29.5
$\Delta\nu_2$/cm^{-1}	^{16}O^{12}C-HF	24.35	24.43	24.46	24.46
B (ν_2)/10^{-2} cm^{-1}	^{16}O^{12}C-HF	10.095	10.099	10.158	10.158
D_J (ν_2)/10^{-8} cm^{-1}	^{16}O^{12}C-HF	33.3	33.2	33.1	33.1
$\Delta\nu_2$/cm^{-1}	^{16}O^{12}C-DF	25.49	25.56	25.58	25.57
B (ν_2)/10^{-2} cm^{-1}	^{16}O^{12}C-DF	10.040	10.044	10.101	10.101
D_J (ν_2)/10^{-8} cm^{-1}	^{16}O^{12}C-DF	31.4	31.3	31.3	31.3
ν_5^1/cm^{-1}	^{16}O^{12}C-HF	80.96	81.17	81.98	81.98
B (ν_5^1)/10^{-2} cm^{-1}	^{16}O^{12}C-HF	10.240	10.244	10.304	10.304
D_J (ν_5^1)/10^{-8} cm^{-1}	^{16}O^{12}C-HF	36.7	36.5	36.4	36.5
Δ ($\nu_1+\nu_5^1-\nu_5^1$)/cm^{-1}	^{16}O^{12}C-HF	-110.30	-111.30	-111.98	-111.98
B ($\nu_1+\nu_5^1$)/10^{-2} cm^{-1}	^{16}O^{12}C-HF	10.446	10.451	10.510	10.510
D_J ($\nu_1+\nu_5^1$)/10^{-8} cm^{-1}	^{16}O^{12}C-HF	33.5	33.3	33.4	33.4
Δ ($\nu_2+\nu_5^1$)/cm^{-1}	^{16}O^{12}C-HF	103.97	104.26	105.10	105.10
B ($\nu_2+\nu_5^1$)/10^{-2} cm^{-1}	^{16}O^{12}C-HF	10.177	10.181	10.242	10.242
D_J ($\nu_2+\nu_5^1$)/10^{-8} cm^{-1}	^{16}O^{12}C-HF	37.1	36.9	36.8	36.8
G		57.4	31.1	0.9	0.9

[a]GS = ground state.

Table 23
Morphing parameters of the relativistic and non-relativistic potentials.

α	$C_\alpha^{(0)}$ Relativistic	$C_\alpha^{(0)}$ Non-relativistic	$C_\alpha^{(4)}$ Relativistic	$C_\alpha^{(4)}$ Non-relativistic	σ for $C_\alpha^{(4)}$ Relativistic	σ for $C_\alpha^{(4)}$ Non-relativistic
1	1.0	1.0	0.9894	0.9844	0.0004	0.0004
2	0.0	0.0	-0.2362	-0.2473	0.0040	0.0040
3	1.0	1.0	0.9786	0.9850	0.0008	0.0008
4	(1.0)	(0.0)	(1.0)	(0.0)	Constrained	Constrained
5	(0.0)	(0.0)	(0.0)	(0.0)	Constrained	Constrained
6	(1.0)	(1.0)	(1.0)	(1.0)	Constrained	Constrained
7	0.0	0.0	0.0012	0.0010	0.0001	0.0001

Table 24
Accuracy of the relativistic $V_{\mathrm{CMM}}^{(4)}$ potential of OC:HF.

Observable (cm^{-1})	Isotopomer	$V_{\mathrm{CMM}}^{(4)}$ Relativistic	Exp	Exp - $V_{\mathrm{CMM}}^{(4)}$
D_0	$^{16}O^{12}C$-HF	743*	732(2)[a]	-11
ν_1	$^{16}O^{12}C$-HF	3844.03007	3844.02937(22)[b]	-0.00070
ν_1	$^{16}O^{12}C$-DF	2821.20156*	2819.90114(14)[c]	-1.30042
ν_2	$^{16}O^{12}C$-HF	2167.72983	2167.69904(11)[d]	-0.03079
ν_2	$^{16}O^{12}C$-DF	2168.84648	2168.86239(16)[c]	0.01591
ν_5^1	$^{16}O^{12}C$-HF	81.98015	81.96825(12)[e]	-0.01190
$\nu_2 + \nu_5^1$	$^{16}O^{12}C$-HF	2248.37280	2248.38623(10)[e]	0.01343
$\nu_1 + \nu_5^1 - \nu_5^1$	$^{16}O^{12}C$-HF	3849.4391	3849.4400(3)[f]	0.0009
$3\nu_1$	$^{16}O^{12}C$-HF	10893.97*	10894.46(1)[g]	0.49

*Data not included in the morphing procedure.
[a]From [135]. [b]From [132]. [c]From [134]. [d]From [129].
[e]Unpublished data provided by Dr. J. W. Bevan.
[f]From [131]. [g]From [136].

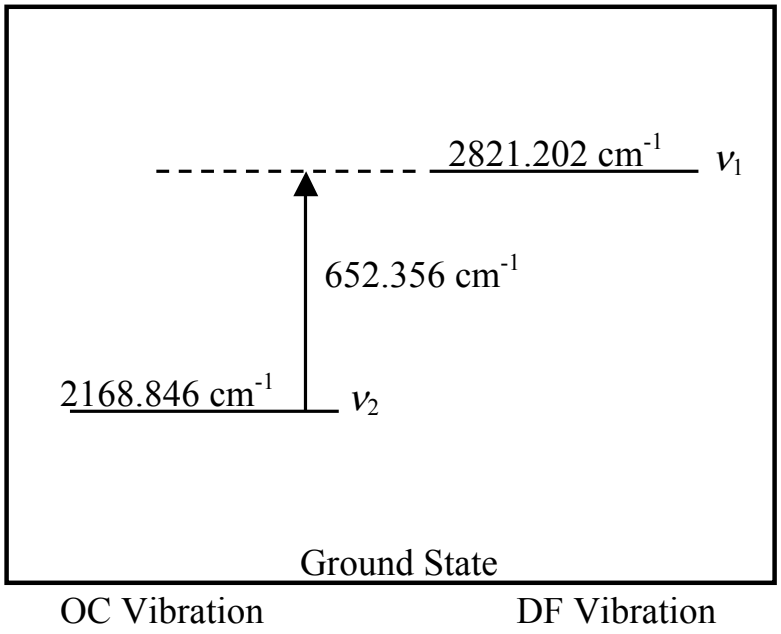

Figure 17. Energy level diagram for OC-DF. The CO and DF frequencies in the complex were calculated using the relativistic $V_{CMM}^{(4)}$ potential. The D_0 of OC-DF is predicted to be 827(5) cm^{-1}.

In Table 22 a comparison between the relativistic (i.e. $C_4 = 1$) and non-relativistic (i.e. $C_4 = 0$) unmorphed potentials show significant relativistic effects on the interaction potential, for the computed observables. It is noted that using the RKR potential, it already includes most significant relativistic effects. In addition, a comparison of the morphing parameters is also given in Table 23. It is found that the optimized morphing parameters are very similar for the relativistic and non-relativistic potentials. The values of G for the relativistic and non-relativistic unmorphed potentials, given by Table 22, are $G = 57.4$ and $G = 31.1$, respectively. Thus, indicating that the non-relativistic unmorphed potential is in better agreement with the experimental observables. However, after the morphing optimization, both surfaces have the same predictions within the errors. This indicates that the morphing procedure has the advantage of correcting for errors in the computed relativistic effects, which may not be appropriate at the Hartree-Fock level.

To test the accuracy of the relativistic $V_{\mathrm{CMM}}^{(4)}$ potential, the calculated and experimental vibrational frequencies for OC:HF are compared in Table 24. As apparent in Table 24, some of the vibrational frequencies were not included in the fitting. The predicted value for D_0, of 743(5) cm^{-1}, agrees with the experimental determined value of 732(2) cm^{-1}, within two standard deviations. The relatively large deviation observed in the prediction of ν_1 in OC-DF, is very likely to be caused by Fermi, and/or Coriolis, coupling. As shown in Figure 17, the more likely choice for the perturbing states are the states that belong to the CO part of the potential, that are close in energy to the ν_1

frequency. Since these perturbing states are in different adiabatic potentials, than the one used to calculate the fundamental ν_1 of OC-DF, the current methodology cannot correct for these perturbations. Yet, the current methodology was able predict the unperturbed vibrational frequencies. In contrast, the experimental frequencies may be perturbed, thus they were unable to be accurately predicted. Using the relativistic $V_{\mathrm{CMM}}^{(4)}$ potential, two Σ states with energies of 2818.262 cm^{-1} and 2825.802 cm^{-1}, and two Π states with energies of 2817.320 cm^{-1} and 2825.085 cm^{-1}, were found in the $\upsilon_{\mathrm{CO}} = 1$ potential surface of OC-DF. These states are within 5 cm^{-1} of the calculated value of ν_1, of 2821.202 cm^{-1}, in OC-DF. However, it is currently difficult to carry out a deperturbation of these interactions by using the currently available spectroscopic data.

The prediction for $3\nu_1$, of 10893.97(50) cm^{-1} in OC-HF, agrees within the computational errors, with the experimental determined value of 10894.46(1) cm^{-1}. In addition the ν_4^1, of OC-HF in the $\upsilon_{\mathrm{HF}} = 3$ potential surface, is predicted to be 501.33(5) cm^{-1}, which can be compared to the 538.20(1) cm^{-1} observed value [136]. The discrepancy in this band is attributed to the fact that the measured data does not actually belong to the assigned state. Another Π state, in the $\upsilon_{\mathrm{HF}} = 3$ potential surface, is predicted to have a frequency of 534.49(5) cm^{-1}, and a rotational constant of 0.10880(4) cm^{-1} which, is closer by 3.71 cm^{-1} to the measured value. This Π state is assigned to the $3\nu_1 + 3\nu_3 + 3\nu_5^1$ combination band. Moreover, a calculated value, for ν_4^1 in the $\upsilon_{\mathrm{HF}} = 3$ potential surface that is in reference [136] of 493.1 cm^{-1}, agrees very well with our

prediction of 501.33(5) cm^{-1}. It is noteworthy that the rest of the vibrational frequencies presented in Table 24 are very close to the experimentally measured values. The deviations in the calculated observables are primarily considered to be results of numerical errors, in the interpolation methods, that have been used in the current calculations. The best way to minimize the interpolation errors is by having a denser grid of *ab initio* points. However, this will be limited to do when large basis sets are needed in the calculation. On the other hand, highly accurate interpolation methods may be developed, but this constitutes a challenging mathematical problem.

In Figure 18, two-dimensional slices of the adiabatic $V^{(0,0)}$ interaction potential, of the relativistic $V^{(4)}_{\mathrm{CMM}}$ potential, of $^{16}O^{12}C$:HF are shown. The corresponding estimated errors relative to the potential at infinite separation are given in Figure 19. The potential has a global minimum, with a well depth of 1311(10) cm^{-1}, corresponding to the equilibrium linear structure $^{16}O^{12}C$-HF with R = 3.598(1) Å. The linear isomer $^{12}C^{16}O$-HF has a corresponding local well depth of 637(10) cm^{-1} with an R = 3.444(1) Å. This results in a ΔE of 674(10) cm^{-1}, between the minima, in the potential energy of two isomers. In Table 25, a comparison of the predicted values for D_e, with previous calculations, is given. It is found that the morphed potential results are intermediate within a range of calculated values. Lastly, in Table 26 predictions for the ν_3 and ν_4^1 fundamental frequencies are given. The predicted value of 368.45(7) cm^{-1} for the ν_4^1 frequency can be used to refine the angular force constant correlation with dissociation, previously discussed by Yu and Klemperer [156].

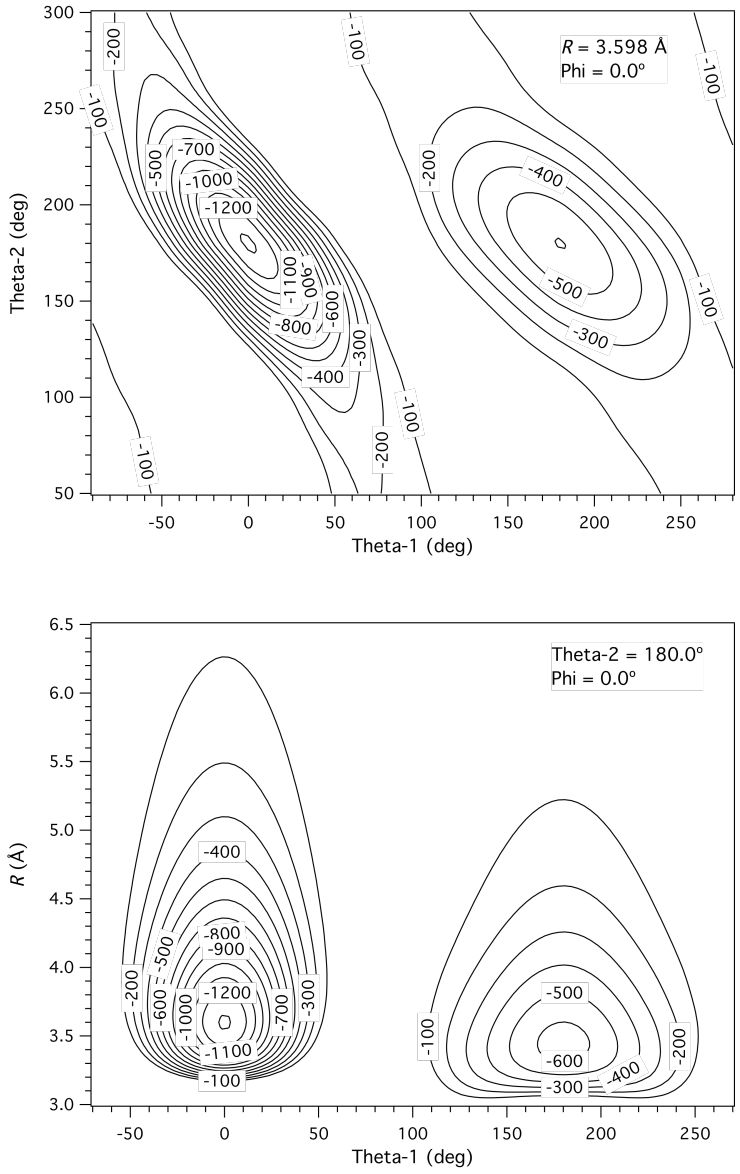

Figure 18. Two-dimensional slices of the adiabatic $V^{(0,0)}$ interaction morphed potential (relativistic $V^{(4)}_{\mathrm{CMM}}$), of $^{16}O^{12}C$:HF. The coordinates used are the Jacobi coordinates defined in Figure 1(c). All contours are in cm^{-1}.

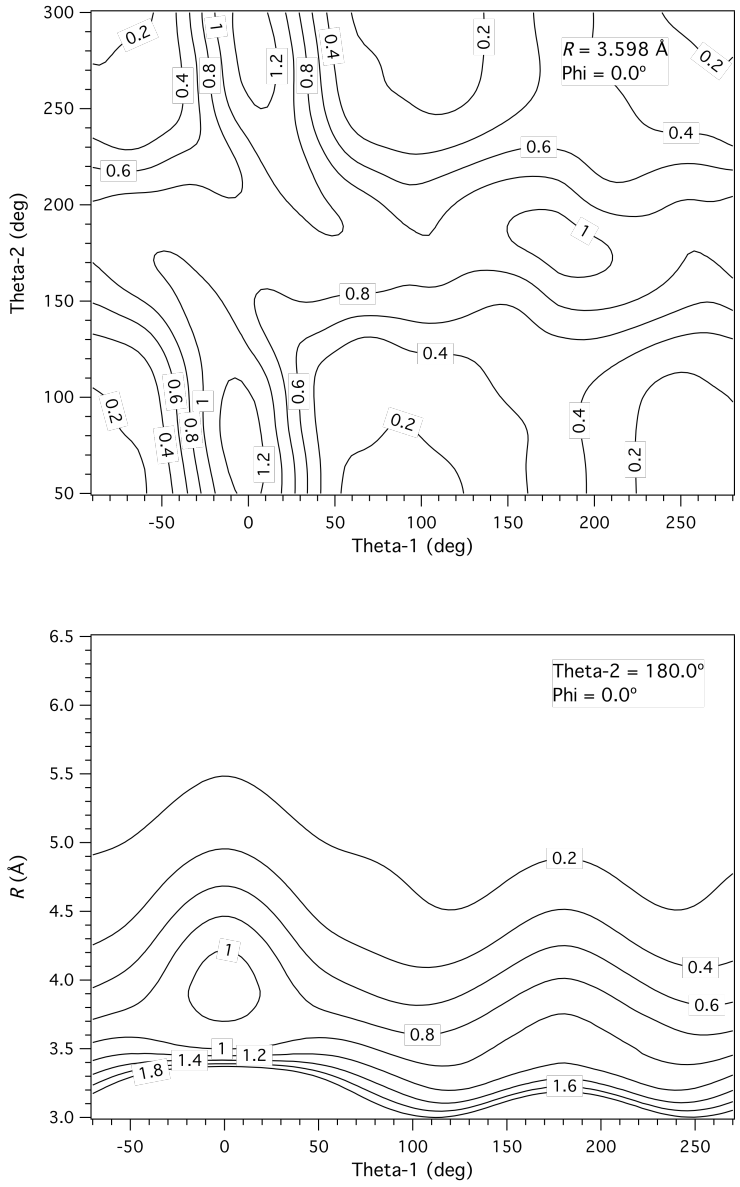

Figure 19. The corresponding estimated errors on the $^{16}O^{12}C$:HF morphed potential, relative to the potential at infinite separation. The coordinates used are the Jacobi coordinates defined in Figure 1(c). All contours are in cm^{-1}.

Table 25
Comparison of previous potentials of OC:HF.

Reference	Method	D_e OC-HF (cm^{-1})	D_e CO-HF (cm^{-1})
This Work[a]	Morphed	1311(10)	637(10)
[84]	*Ab initio*, HF	733	659
[139]	*Ab initio*, ACCD	1066	603
[112]	*Ab initio*, MP2	1340	549
[146]	MMC	732	458
[149]	*Ab initio*, CCSD(T)	1222	584
[149]	DFT, HCTH38	1265	489

[a]The potential used for this predictions is the adiabatic $V^{(0,0)}$ potential from the relativistic $V^{(4)}_{CMM}$ potential of $^{16}O^{12}C$:HF.

Table 26
Predictions of ν_3 and ν_4^1 frequencies of $^{16}O^{12}C$-HF, using the relativistic $V^{(4)}_{CMM}$ potential.

$B(\nu_3)$ ($\times 10^{-2}$ cm^{-1})	$B(\nu_4^1)$ ($\times 10^{-2}$ cm^{-1})	$D_J(\nu_3)$ ($\times 10^{-8}$ cm^{-1})	$D_J(\nu_4^1)$ ($\times 10^{-8}$ cm^{-1})	ν_3 (cm^{-1})	ν_4^1 (cm^{-1})
9.958(3)	9.888(3)	39.84(4)	45.11(9)	108.04(2)	368.45(7)

The application of the CMM method to symmetric dimers, such as HX (X = F, Cl, Br, I) dimers, must await future work, where the inclusion of non-adiabatic coupling in the rovibrational Hamiltonian will be indispensable. The current application to OC:HF dimer may improved by considering the proper calculation of $B_{\upsilon_x}(\Omega)$. Consequently, this will also increase the difficulties for the evaluation of the derivatives of the rovibrational eigenvalues with respect to the morphing parameters.

A complete six-dimensional morphed PES has been generated for the OC:HF hydrogen-bonded dimer. It is found that the CP method over corrected the BSSE by 24(2)%, as seen by the negative value of the $C_2^{(4)}$ parameter in Table 21, and the definition of the morphing parameters in Eq. (61). The calculated vibrational frequencies from the morphed potential are in very good agreement with the experimental values. The small errors in the calculated observables primarily come from numerical errors in the interpolation methods. Nevertheless, the current morphed potential is quantitatively good and it can be claimed that it has nearly spectroscopic accuracy.

5. CONCLUSIONS

In this dissertation, reliable morphed interaction potential energy surfaces have been calculated for the prototypical systems of non-covalent interaction: Ne:HCl, OC:HF, OC:HCl, OC:HBr, OC:HI, and HI:CO_2. Also, the compound model morphing method has been presented and shown to be as accurate and reliable as the potential coordinate morphing method. The compound model morphing method was extended, from four-dimensions to six-dimensions, and applied to the OC:HF system to morph the vibrationally-complete six-dimensional potential of this complex. It has been found that the morphing parameters in the CMM method are similar for the OC:HCl and OC:HBr systems. However, for the OC:HF system, the morphing parameters in the CMM method are different from those for OC:HCl and OC:HBr. In the OC:HCl and OC:HBr complexes, the value of the C_3 parameter was found to be close to 0.5, whereas for OC:HF it was close to one. These results imply that the CCSD(T) calculation is better suited for OC:HF, rather than to OC:HCl or OC:HBr. In addition, a comparison of the morphing parameters in the CMM method for OC:HF, OC:HCl, and OC:HBr gave a fundamental insight about the nature of the BSSE. It was found that the CP method successfully corrected the BSSE in OC:HCl, but under corrected, by 16(7)%, in OC:HBr and over corrected, by 24(2)%, in OC:HF. These results support the conclusion by Tuma et al. [149] where it is stated that BSSE becomes less important with strong interactions. This implies a connection between the BSSE and the contributions for the interaction potential in the OC:HX (X = F, Cl, Br) complexes.

The interaction potential of non-covalent systems is governed by different contributions to the interaction energy, i.e. electrostatic, induction, electron delocalization, exchange repulsion, and dispersion [157]. In the families Rg-HX, OC-HX, and CO_2-HX (Rg = Ne, Ar, Kr; X = F, Cl, Br, I) [21,30,89,96,146] there exists a competition between the hydrogen bond and van der Waals interactions. As the number of electrons (from F to I) increases in the atom X, the dipole moment of H-X decreases, and the dispersion effects increase; thus favoring van der Waals interactions. For fluorine the hydrogen bond interactions dominates, while for iodine the van der Waals interactions dominates. On the other hand, for chlorine and bromine the two different types of interactions make comparable contributions to the interaction potential. In addition, for the OC:HX complexes, the differences in stability of the OC-HX and CO-HX can be attributed to the interactions of the carbon and oxygen lone pairs, with the anti-bonding orbital on HX [112]. Since the lone pair orbitals of carbon are at higher energy than those of oxygen, it makes it a better electron density donor to the anti-bonding orbital on HX. Consequently, the hydrogen bond and van der Waals interactions work in opposing directions to create a natural balance of intermolecular interactions in real systems.

The results from this study are relevant to understand differences in the thermodynamics of hydration of H_2O and D_2O [158-160]. Previous studies have shown a difference in the stability and flexibility of protein in H_2O and D_2O solvents [161-165]. This difference in stability and flexibility has been attributed to the different abilities of H_2O and D_2O to solvate polar and non-polar groups in the protein [158]. Consequently,

the ground state isotopic isomerization, observed in the OC-HI complex, may suggest a structural change of biological macromolecules in deuterated solvents [166-169].

Hydrogen bonding is a very old concept in chemistry, but still a phenomenon not well understood [157]. Non-covalent interactions, in particular the hydrogen bond and van der Waals interaction, are one of the most important concepts, not only in chemistry, but in all branches of molecular science as well. Above all, there are problems that remain open, and further research needs to be done to gain new insight into the nature of intermolecular interactions. Some possible directions to extend the current research are as follow:

i) An important improvement in the potential morphing methodology would be the development of an analytical derivative treatment of the intramolecular modes.

ii) The reduction of interpolation errors, by calculating a very dense grid of *ab initio* points, will be feasible in the near future as better and faster computers become available. In addition, highly accurate interpolation methods may be developed, but this will constitute a challenging mathematical problem.

iii) In the case of degenerate vibrations, such as in the six-dimension calculation of HX (X = F, Cl, Br, I) dimers, a vibrational multiconfigurational self-consistent field calculation [170] would be needed. Also, the inclusion of non-adiabatic coupling, and the proper calculation of $B_{\upsilon_x}\left(\Omega\right)$, in the rovibrational Hamiltonian will be indispensable.

iv) A challenging step in the potential morphing theory would be an increase in the dimensionality of the system to a nine-dimension treatment of triatom-diatom

systems, such as HCN:HF. Also, the development of a methodology to morph the interaction potential of dimers that have one or two non-linear monomer constitutes a formidable computational challenge.

REFERENCES

[1] H. Margenau, Reviews of Modern Physics 11 (1939) 1-35.

[2] L. Pauling, The nature of the chemical bond and the structure of molecules and crystals: an introduction to modern structural chemistry, Cornell University Press, Ithaca, 1960.

[3] B. Widom, Science 157 (1967) 375-382.

[4] P. Hobza, R. Zahradník, Topics in Current Chemistry 93 (1980) 53-90.

[5] G.A. Jeffrey, W. Saenger, Hydrogen bonding in biological structures, Springer-Verlag, Berlin, 1991.

[6] J. Cerny, P. Hobza, Physical Chemistry Chemical Physics 9 (2007) 5291-5303.

[7] L. Pauling, M. Delbruck, Science 92 (1940) 77-79.

[8] F. Jensen, Introduction to computational chemistry, Wiley, Chichester, 1999.

[9] J.N. Murrell, Molecular potential energy functions, Wiley, Chichester, 1984.

[10] R.J. Le Roy, J. Scott Carley, Advances in Chemical Physics 42 (1980) 353-420.

[11] A.J. Stone, The theory of intermolecular forces, Oxford University Press, Oxford, 1996.

[12] T.S. Ho, H. Rabitz, Journal of Physical Chemistry 97 (1993) 13447-13456.

[13] J.M. Hutson, Annual Review of Physical Chemistry 41 (1990) 123-154.

[14] A.D. Buckingham, P.W. Fowler, J.M. Hutson, Chemical Reviews 88 (1988) 963-988.

[15] G. Chalasinski, M.M. Szczesniak, Chemical Reviews 94 (1994) 1723-1765.

[16] M. Meuwly, J.M. Hutson, Journal of Chemical Physics 110 (1999) 8338-8347.

[17] A. McIntosh, Z. Wang, J. Castillo-Chara, R.R. Lucchese, J.W. Bevan, R.D. Suenram, A.C. Legon, Journal of Chemical Physics 111 (1999) 5764-5770.

[18] J.M.M. Howson, J.M. Hutson, Journal of Chemical Physics 115 (2001) 5059-5065.

[19] A. McIntosh, P. Lin, R.R. Lucchese, J.W. Bevan, D.J. Brugh, R.D. Suenram, Chemical Physics Letters 331 (2000) 95-100.

[20] P. Lin, W. Jabs, R.R. Lucchese, J.W. Bevan, D.J. Brugh, R.D. Suenram, Chemical Physics Letters 356 (2002) 101-108.

[21] R.R. Lucchese, J.W. Bevan, F.J. Lovas, Chemical Physics Letters 398 (2004) 544-552.

[22] B.A. McElmurry, R.R. Lucchese, J.W. Bevan, S.P. Belov, Physical Chemistry Chemical Physics 6 (2004) 5318-5323.

[23] J. Castillo-Chara, R.R. Lucchese, J.W. Bevan, Journal of Chemical Physics 115 (2001) 899-911.

[24] S.P. Belov, B.A. McElmurry, R.R. Lucchese, J.W. Bevan, I. Leonov, Chemical Physics Letters 370 (2003) 528-534.

[25] Z. Wang, R.R. Lucchese, J.W. Bevan, Journal of Physical Chemistry A 108 (2004) 2884-2892.

[26] Z. Wang, A.L. McIntosh, B.A. McElmurry, J.R. Walton, R.R. Lucchese, J.W. Bevan, Journal of Physical Chemistry A 109 (2005) 8168-8179.

[27] L.A. Rivera-Rivera, B.A. McElmurry, S.P. Belov, R.R. Lucchese, J.W. Bevan, Chemical Physics Letters 444 (2007) 9-16.

[28] B.A. McElmurry, R.R. Lucchese, J.W. Bevan, S.P. Belov, I.I. Leonov, Chemical Physics Letters 407 (2005) 40-47.

[29] L.A. Rivera-Rivera, R.R. Lucchese, J.W. Bevan, Chemical Physics Letters 429 (2006) 68-76.

[30] W. Jabs, F.F. Willaert, B.A. McElmurry, L.A. Rivera-Rivera, R. Montuoro, R.R. Lucchese, J.W. Bevan, R.D. Suenram, Journal of Physical Chemistry A 111 (2007) 11976-11985.

[31] K.J. Higgins, W. Klemperer, Journal of Chemical Physics 122 (2005) 244309-12.

[32] L.A. Rivera-Rivera, R.R. Lucchese, J.W. Bevan, Chemical Physics Letters 460 (2008) 352-358.

[33] S.V. Shirin, O.L. Polyansky, N.F. Zobov, R.I. Ovsyannikov, A.G. Csaszar, J. Tennyson, Journal of Molecular Spectroscopy 236 (2006) 216-223.

[34] S. Green, Journal of Chemical Physics 62 (1975) 2271-2277.

[35] H.-J. Werner, P.J. Knowles, R. Lindh, F.R. Manby, M. Schütz, P. Celani, T. Korona, G. Rauhut, R.D. Amos, A. Bernhardsson, A. Berning, D.L. Cooper, M.J.O. Deegan, A.J. Dobbyn, F. Eckert, C. Hampel, G. Hetzer, A.W. Lloyd, S.J. McNicholas, W. Meyer, M.E. Mura, A. Nicklass, P. Palmieri, R. Pitzer, U. Schumann, H. Stoll, A.J. Stone, R. Tarroni, T. Thorsteinsson, MOLPRO, version 2006.1, a package of ab initio programs, Cardiff, UK, 2006.

[36] H.-J. Werner, P.J. Knowles, R. Lindh, F.R. Manby, M. Schütz, P. Celani, T. Korona, A. Mitrushenkov, G. Rauhut, T.B. Adler, R.D. Amos, A. Bernhardsson, A. Berning, D.L. Cooper, M.J.O. Deegan, A.J. Dobbyn, F. Eckert, E. Goll, C.

Hampel, G. Hetzer, T. Hrenar, G. Knizia, C. Köppl, Y. Liu, A.W. Lloyd, R.A. Mata, A.J. May, S.J. McNicholas, W. Meyer, M.E. Mura, A. Nicklass, P. Palmieri, K. Pflüger, R. Pitzer, M. Reiher, U. Schumann, H. Stoll, A.J. Stone, R. Tarroni, T. Thorsteinsson, M. Wang, A. Wolf, MOLPRO, version 2009.1, a package of ab initio programs, Cardiff, UK, 2009.

[37] T.H. Dunning, Journal of Chemical Physics 90 (1989) 1007-1023.

[38] D.E. Woon, T.H. Dunning, Journal of Chemical Physics 98 (1993) 1358-1371.

[39] T.H. Dunning, K.A. Peterson, A.K. Wilson, Journal of Chemical Physics 114 (2001) 9244-9253.

[40] S.F. Boys, F. Bernardi, Molecular Physics 19 (1970) 553-566.

[41] W.A. de Jong, R.J. Harrison, D.A. Dixon, Journal of Chemical Physics 114 (2001) 48-53.

[42] M. Douglas, N.M. Kroll, Annals of Physics 82 (1974) 89-155.

[43] B.A. Hess, Physical Review A 33 (1986) 3742-3748.

[44] T.S. Ho, H. Rabitz, Journal of Chemical Physics 104 (1996) 2584-2597.

[45] J. Castillo-Chara, J.W. Bevan, R.R. Lucchese, Computer Physics Communications 145 (2002) 48-63.

[46] C.G. Gray, K.E. Gubbins, Theory of molecular fluids, Oxford University Press, Oxford, 1984.

[47] A. van der Avoird, P.E.S. Wormer, R. Moszynski, Chemical Reviews 94 (1994) 1931-1974.

[48] M.H. Alexander, A.E. Depristo, Journal of Chemical Physics 65 (1976) 5009-5016.

[49] J. Castillo-Chara, A.L. McIntosh, Z. Wang, R.R. Lucchese, J.W. Bevan, Journal of Chemical Physics 120 (2004) 10426-10441.

[50] A. van der Avoird, P. Wormer, F. Mulder, R. Berns, Topics in Current Chemistry 93 (1980) 1-51.

[51] P. Lancaster, K. Šalkauskas, Curve and surface fitting: an introduction, Academic Press, London, 1986.

[52] D.C. Clary, D.J. Nesbitt, Journal of Chemical Physics 90 (1989) 7000-7013.

[53] A. Quinones, G. Bandarage, J.W. Bevan, R.R. Lucchese, Journal of Chemical Physics 97 (1992) 2209-2223.

[54] A. McIntosh, A.M. Gallegos, R.R. Lucchese, J.W. Bevan, Journal of Chemical Physics 107 (1997) 8327-8337.

[55] J. Han, A.L. McIntosh, Z. Wang, R.R. Lucchese, J.W. Bevan, Chemical Physics Letters 265 (1997) 209-216.

[56] C. Leforestier, L.B. Braly, K. Liu, M.J. Elrod, R.J. Saykally, Journal of Chemical Physics 106 (1997) 8527-8544.

[57] G. Brocks, A. van der Avoird, B.T. Sutcliffe, J. Tennyson, Molecular Physics 50 (1983) 1025-1043.

[58] J.K. Cullum, R.A. Willoughby, Lanczos algorithms for large symmetric eigenvalue computations, Birkhäuser, Boston, 1985.

[59] N.L. Singh, D.C. Jain, Proceedings of the Physical Society of London 79 (1962) 274-278.

[60] R. Sankari, M. Ehara, H. Nakatsuji, Y. Senba, K. Hosokawa, H. Yoshida, A. De Fanis, Y. Tamenori, S. Aksela, K. Ueda, Chemical Physics Letters 380 (2003) 647-653.

[61] J.W. Cooley, Mathematics of Computation 15 (1961) 363-374.

[62] W.H. Press, B.P. Flannery, S.A. Teukolsky, W.T. Vetterling, Numerical recipes: the art of scientific computing, Cambridge University Press, Cambridge, 1986.

[63] J.M. Bowman, Accounts of Chemical Research 19 (1986) 202-208.

[64] J.M. Hutson, Chemical Physics Letters 151 (1988) 565-569.

[65] J.M. Hutson, Journal of Chemical Physics 96 (1992) 6752-6767.

[66] S.E. Novick, P.B. Davies, T.R. Dyke, W. Klemperer, Journal of the American Chemical Society 95 (1973) 8547-8550.

[67] A.E. Barton, D.J.B. Howlett, B.J. Howard, Molecular Physics 41 (1980) 619-628.

[68] J.M. Prout, BA Thesis, Part II, Oxford University, Oxford, 1981.

[69] J.M. Hutson, B.J. Howard, Molecular Physics 45 (1982) 769-790.

[70] C.M. Lovejoy, D.J. Nesbitt, Chemical Physics Letters 147 (1988) 490-496.

[71] J.M. Hutson, Journal of Chemical Physics 91 (1989) 4448-4454.

[72] M.D. Schuder, D.D. Nelson, D.J. Nesbitt, Journal of Chemical Physics 94 (1991) 5796-5811.

[73] V. Subramanian, D. Sivanesan, T. Ramasami, Chemical Physics Letters 295 (1998) 312-316.

[74] T.J. Dudley, R.R. Pandey, P.E. Staffin, M.R. Hoffmann, G.C. Schatz, Journal of Chemical Physics 114 (2001) 6166-6179.

[75] L. Jiang, Z. Hua, X. Dai-Qian, Y. Guo-Sen, Chemical Journal of Chinese Universities 24 (2003) 686-689.

[76] J.L. Cagide Fajin, J.L. Cacheiro, B. Fernandez, Journal of Chemical Physics 121 (2004) 4599-4604.

[77] H.M. Hulburt, J.O. Hirschfelder, Journal of Chemical Physics 9 (1941) 61-69.

[78] D.H. Rank, B.S. Rao, T.A. Wiggins, Journal of Molecular Spectroscopy 17 (1965) 122-130.

[79] K.P. Huber, G. Herzberg, Molecular spectra and molecular structure IV: constants of diatomic molecules, van Nostrand Reinhold, New York, 1979.

[80] F.C. De Lucia, P. Helminger, W. Gordy, Physical Review A 3 (1971) 1849-1857.

[81] R.S. Altman, M.D. Marshall, W. Klemperer, A. Krupnov, Journal of Chemical Physics 79 (1983) 52-56.

[82] J.D. Augspurger, C.E. Dykstra, Chemical Physics Letters 189 (1992) 303-310.

[83] R. Garnica, A.L. McIntosh, Z. Wang, R.R. Lucchese, J.W. Bevan, A.R. McKellar, Chemical Physics Letters 272 (1997) 484-488.

[84] A. Hinchliffe, Advances in Molecular Relaxation and Interaction Processes 21 (1981) 151-157.

[85] R.W. Larsen, F. Hegelund, B. Nelander, Journal of Physical Chemistry A 108 (2004) 1524-1530.

[86] S.A.C. McDowell, A.D. Buckingham, Journal of the American Chemical Society 127 (2005) 15515-15520.

[87] A.R.W. Mckellar, Z. Lu, Journal of Molecular Spectroscopy 161 (1993) 542-551.

[88] R.F. Meads, C.L. Hartz, R.R. Lucchese, J.W. Bevan, Chemical Physics Letters 206 (1993) 488-492.

[89] P. Politzer, C.W. Kammeyer, J. Bauer, W.L. Hedges, Journal of Physical Chemistry 85 (1981) 4057-4060.

[90] K.S. Rutkowski, S. Melikova, D.N. Shchepkin, P. Lipkowski, A. Koll, Chemical Physics Letters 325 (2000) 425-432.

[91] P.D. Soper, A.C. Legon, W.H. Flygare, Journal of Chemical Physics 74 (1981) 2138-2142.

[92] Z. Wang, M. Eliades, J.W. Bevan, Chemical Physics Letters 161 (1989) 6-11.

[93] A.C. Legon, P.D. Soper, W.H. Flygare, Journal of Chemical Physics 74 (1981) 4944-4950.

[94] L. Andrews, R.T. Arlinghaus, G.L. Johnson, Journal of Chemical Physics 78 (1983) 6347-6352.

[95] A.C. Legon, P.D. Soper, M.R. Keenan, T.K. Minton, T.J. Balle, W.H. Flygare, Journal of Chemical Physics 73 (1980) 583-584.

[96] M.R. Keenan, T.K. Minton, A.C. Legon, T.J. Balle, W.H. Flygare, Proceedings of the National Academy of Sciences of the United States of America 77 (1980) 5583-5587.

[97] Z. Wang, J.W. Bevan, Chemical Physics Letters 167 (1990) 49-56.

[98] Z. Wang, M. Eliades, K. Carron, J.W. Bevan, Review of Scientific Instruments 62 (1991) 21-26.

[99] Z. Wang, A.L. McIntosh, R.R. Lucchese, J.W. Bevan, Journal of Molecular Structure 695 (2004) 171-180.

[100] Z. Wang, R.R. Lucchese, J.W. Bevan, A.P. Suckley, C.A. Rego, A.C. Legon, Journal of Chemical Physics 98 (1993) 1761-1767.

[101] A.L. McIntosh, Z. Wang, R.R. Lucchese, J.W. Bevan, Infrared Physics & Technology 45 (2004) 301-314.

[102] A.L. McIntosh, Z. Wang, R.R. Lucchese, J.W. Bevan, A.C. Legon, Chemical Physics Letters 305 (1999) 57-62.

[103] K.A. Peterson, C. Puzzarini, Theoretical Chemistry Accounts 114 (2005) 283-296.

[104] P. Helminge, F.C. De Lucia, W. Gordy, Physical Review Letters 25 (1970) 1397-1399.

[105] F.J. Lovas, P.H. Krupenie, Journal of Physical and Chemical Reference Data 3 (1974) 245-257.

[106] L.A. Rivera-Rivera, Z. Wang, B.A. McElmurry, F.F. Willaert, R.R. Lucchese, J.W. Bevan, R.D. Suenram, F.J. Lovas, Journal of Chemical Physics 133 (2010) 184305-13.

[107] F.F. Willaert, B.A. McElmurry, R.R. Lucchese, J.W. Bevan, Chemical Physics Letters 460 (2008) 525-530.

[108] J. Kraitchman, American Journal of Physics 21 (1953) 17-24.

[109] Z. Kisiel, Journal of Molecular Spectroscopy 218 (2003) 58-67.

[110] J.K. Rice, F.J. Lovas, G.T. Fraser, R.D. Suenram, Journal of Chemical Physics 103 (1995) 3877-3884.

[111] H.S. Gutowsky, T. Emilsson, E. Arunan, Journal of Chemical Physics 106 (1997) 5309-5315.

[112] L.A. Curtiss, D.J. Pochatko, A.E. Reed, F. Weinhold, Journal of Chemical Physics 82 (1985) 2679-2687.

[113] Y. Chen, G. Hoffmann, D. Oh, C. Wittig, Chemical Physics Letters 159 (1989) 426-434.

[114] M. Fushitani, T. Shida, T. Momose, M. Rasanen, Journal of Physical Chemistry A 104 (2000) 3635-3641.

[115] S.I. Ionov, G.A. Brucker, C. Jaques, L. Valachovic, C. Wittig, Journal of Chemical Physics 97 (1992) 9486-9489.

[116] N.F. Scherer, L.R. Khundkar, R.B. Bernstein, A.H. Zewail, Journal of Chemical Physics 87 (1987) 1451-1453.

[117] N.F. Scherer, C. Sipes, R.B. Bernstein, A.H. Zewail, Journal of Chemical Physics 92 (1990) 5239-5259.

[118] A.J. Misquitta, R. Bukowski, K. Szalewicz, Journal of Chemical Physics 112 (2000) 5308-5319.

[119] G. Graner, C. Rossetti, D. Bailly, Molecular Physics 58 (1986) 627-636.

[120] J.S. Muenter, Journal of Chemical Physics 103 (1995) 1263-1273.

[121] Y.P. Zeng, S.W. Sharpe, S.K. Shin, C. Wittig, R.A. Beaudet, Journal of Chemical Physics 97 (1992) 5392-5402.

[122] L. Oudejans, R.E. Miller, Journal of Chemical Physics 109 (1998) 3474-3484.

[123] L. Oudejans, D. Olson, R.E. Miller, Journal of Chemical Physics 105 (1996) 8515-8522.

[124] R.S. Altman, M.D. Marshall, W. Klemperer, Journal of Chemical Physics 77 (1982) 4344-4349.

[125] F.A. Baiocchi, T.A. Dixon, C.H. Joyner, W. Klemperer, Journal of Chemical Physics 74 (1981) 6544-6549.

[126] E.J. Campbell, W.G. Read, J.A. Shea, Chemical Physics Letters 94 (1983) 69-72.

[127] W.G. Read, E.J. Campbell, Journal of Chemical Physics 78 (1983) 6515-6530.

[128] E.K. Kyro, P. Shoja-Chaghervand, K. Mcmillan, M. Eliades, D. Danzeiser, J.W. Bevan, Journal of Chemical Physics 79 (1983) 78-80.

[129] Z. Wang, J.W. Bevan, Journal of Chemical Physics 91 (1989) 3335-3339.

[130] K.W. Jucks, R.E. Miller, Journal of Chemical Physics 86 (1987) 6637-6645.

[131] K. Mcmillan, D. Bender, M. Eliades, D. Danzeiser, B.A. Wofford, J.W. Bevan, Chemical Physics Letters 152 (1988) 87-93.

[132] G.T. Fraser, A.S. Pine, Journal of Chemical Physics 88 (1988) 4147-4152.

[133] C. Hartz, B.A. Wofford, R.F. Meads, R.R. Lucchese, J.W. Bevan, Review of Scientific Instruments 66 (1995) 4375-4384.

[134] J. Han, A.L. McIntosh, C.L. Hartz, J.W. Bevan, Chemical Physics Letters 264 (1997) 411-416.

[135] L. Oudejans, R.E. Miller, Journal of Chemical Physics 113 (2000) 4581-4587.

[136] Z.H. Yu, C.C. Chuang, P. Medley, T.A. Stone, W. Klemperer, Journal of Chemical Physics 120 (2004) 6922-6929.

[137] I.L. Alberts, N.C. Handy, E.D. Simandiras, Theoretica Chimica Acta 74 (1988) 415-428.

[138] M.A. Benzel, C.E. Dykstra, Journal of Chemical Physics 77 (1982) 1602-1603.

[139] M.A. Benzel, C.E. Dykstra, Chemical Physics 80 (1983) 273-278.

[140] M.A. Benzel, C.E. Dykstra, Journal of Chemical Physics 78 (1983) 4052-4062.

[141] M.A. Benzel, C.E. Dykstra, Journal of Chemical Physics 80 (1984) 3510-3511.

[142] P. Botschwina, Journal of the Chemical Society-Faraday Transactions II 84 (1988) 1263-1276.

[143] C. Chen, S.J. Chen, Y.S. Hong, Journal of the Chinese Chemical Society 52 (2005) 853-861.

[144] S.J. Chen, C. Chen, Y.S. Hong, Journal of the Chinese Chemical Society 53 (2006) 783-792.

[145] B. Civalleri, E. Garrone, P. Ugliengo, Journal of Molecular Structure: THEOCHEM 419 (1997) 227-238.

[146] C.A. Parish, J.D. Augspurger, C.E. Dykstra, Journal of Physical Chemistry 96 (1992) 2069-2079.

[147] A.E. Reed, F. Weinhold, L.A. Curtiss, D.J. Pochatko, Journal of Chemical Physics 84 (1986) 5687-5705.

[148] M.A. Spackman, Journal of Chemical Physics 85 (1986) 6587-6601.

[149] C. Tuma, A.D. Boese, N.C. Handy, Physical Chemistry Chemical Physics 1 (1999) 3939-3947.

[150] G. Schatte, H. Willner, D. Hoge, E. Knoezinger, O. Schrems, Journal of Physical Chemistry 93 (1989) 6025-6028.

[151] L. Andrews, R.D. Hunt, Journal of Physical Chemistry 92 (1988) 81-85.

[152] K.G. Tokhadze, Z. Mielke, Journal of Chemical Physics 99 (1993) 5071-5077.

[153] V.P. Bulychev, Z. Mielke, K.G. Tokhadze, S.S. Utkina, Optics and Spectroscopy 86 (1999) 352-360.

[154] A.W. Mantz, J.K.G. Watson, K.N. Rao, D.L. Albritto, A.L. Schmelte, R.N. Zare, Journal of Molecular Spectroscopy 39 (1971) 180-184.

[155] J.A. Coxon, P.G. Hajigeorgiou, Journal of Molecular Spectroscopy 142 (1990) 254-278.

[156] Z.H. Yu, W. Klemperer, Proceedings of the National Academy of Sciences of the United States of America 102 (2005) 12667-12669.

[157] A.D. Buckingham, J.E. Del Bene, S.A.C. McDowell, Chemical Physics Letters 463 (2008) 1-10.

[158] G. Hummer, S. Garde, A.E. Garcia, L.R. Pratt, Chemical Physics 258 (2000) 349-370.

[159] O. Likhodi, T.V. Chalikian, Journal of the American Chemical Society 122 (2000) 7860-7868.

[160] M.M. Lopez, G.I. Makhatadze, Biophysical Chemistry 74 (1998) 117-125.

[161] P. Cioni, G.B. Strambini, Biophysical Journal 82 (2002) 3246-3253.

[162] G.I. Makhatadze, G.M. Clore, A.M. Gronenborn, Nature Structural Biology 2 (1995) 852-855.

[163] S.Y. Sheu, E.W. Schlag, H.L. Selzle, D.Y. Yang, Journal of Physical Chemistry A 112 (2008) 797-802.

[164] Z.S. Shi, B.A. Krantz, N. Kallenbach, T.R. Sosnick, Biochemistry 41 (2002) 2120-2129.

[165] Y.M. Efimova, S. Haemers, B. Wierczinski, W. Norde, A.A. van Well, Biopolymers 85 (2007) 264-273.

[166] B.W. Chellgren, T.P. Creamer, Journal of the American Chemical Society 126 (2004) 14734-14735.

[167] A.N. Drozdov, A. Grossfield, R.V. Pappu, Journal of the American Chemical Society 126 (2004) 2574-2581.

[168] A. Kentsis, M. Mezei, T. Gindin, R. Osman, Proteins-Structure Function and Bioinformatics 55 (2004) 493-501.

[169] M. Mezei, P.J. Fleming, R. Srinivasan, G.D. Rose, Proteins-Structure Function and Bioinformatics 55 (2004) 502-507.

[170] F. Culot, F. Lievin, Theoretica Chimica Acta 89 (1994) 227-250.

VITA

Name: Luis A. Rivera-Rivera

Address: Department of Chemistry, Texas A&M University, College Station, TX 77843-3255, USA

Email Address: rivera@chem.tamu.edu

Education:

2011	Texas A&M University Ph.D. in Chemistry
2004	University of Puerto Rico at Mayagüez M.S. in Chemistry
2002	University of Puerto Rico at Mayagüez B.S. in Chemistry with High Honors

Experience:

2007-2008	Teaching Assistant, Department of Chemistry, Texas A&M University
2005-2011	Research Assistant, Department of Chemistry, Texas A&M University
2004	Research Associate, Department of Chemistry, University of Puerto Rico at Mayagüez
2002-2003	Teaching Assistant, Department of Chemistry, University of Puerto Rico at Mayagüez
1999-2003	Research Assistant, Department of Chemistry, University of Puerto Rico at Mayagüez

Selected Publications:

L.A. Rivera-Rivera, Z. Wang, B.A. McElmurry, F.F. Willaert, R.R. Lucchese, J.W. Bevan, R.D. Suenram, F.J. Lovas, "A ground state morphed intermolecular potential for the hydrogen bonded and van der Waals isomers in OC:HI and a prediction of an anomalous deuterium isotope effect", J. Chem. Phys. 133 (2010) 184305.

L.A. Rivera-Rivera, R.R. Lucchese, J.W. Bevan, "A parameterized compound-model chemistry for morphing the intermolecular potential of OC-HCl", Chem. Phys. Lett. 460 (2008) 352.